

People's Democratic Republic of Algeria
Ministry of Higher Education and Scientific Research
UNIVERSITY OF KASDI MERBAH OUARGLA
Faculty of Mathematics and Material Sciences
Department of physics



THESIS

For obtaining the LMD Doctorate Degree in physics

Specialty: Physics of Material

Presented by:

BESRA Safa

Entitled

***Synthesis and characterization of thin films
based on functional metal oxides***

Publicly defended on: 11/02/ 2024

Jury Members:

CHOHRA Thouria	Pr.	Ouargla Univ	President
BENSOUICI Aicha	Pr.	Constantine-1 Univ	Examiner
BELKHELFA Hakim	M.R.A	CRAPC Ouargla	Examiner
GHERIANI Rachid	Pr.	Ouargla Univ	Examiner
BELAKROUM Karima	Pr.	Ouargla Univ	Supervisor
IAICHE Sabrina	M.C.A	Khenchela Univ	Co-Supervisor
HENNI Abdallah	Pr.	Ouargla Univ	Invited

Academic year: 2023-2024

ACKNOWLEDGEMENTS

At the end of this work, we would first like to thank God for guiding us and offering us the courage, power, and patience to carry out this work as best as possible. I am totally sure that this work would have never come true, without His guidance.

This thesis allowed me to meet several people who helped me accomplish this work in the best conditions and for whom; I express my most sincere thanks.

*I want to express my deepest thanks to my supervisor, Pr. **Belakroum Karima**, for her patience, her valuable advice, and her presence during the preparation of this thesis.*

*My deep gratitude and sincere thanks to the Co-director of my thesis, PhD (MCB) **Sabrina LAICHE** for her availability for allowing me to benefit from her scientific skills, and for having directed this work in a spirit of trust and confidence.*

*I extend my special and sincere thanks to Professor **HENNI Abdellah** for following my work closely with serenity, his scientific rigor, and his precious advice which guided me well in the development of this study. I also thank him for the trust & understanding he has always shown towards me. If this work is completed, it is thanks to his help and support.*

May he be assured of my deep esteem and may he find here the expression of my deep gratitude.

*My deepest sincere gratitude to my Sir Professor **Ghariani Rachid** in University Kasdi Merbah Ouargla for giving me a chance to work in their laboratory, I will never forget and I will be eternally grateful to you.*

*This makes it a great honor for me to have the chance to carry out this dissertation within the **LRPPS Laboratory** (Lab. of Radiation & Plasmas & Surface Phy).*

ACKNOWLEDGEMENTS

I am honored that Pr. CHOHRA Thouria, a Professor at the University of Ouargla, chairs the jury for this thesis. I thank her very much. I would also like to thank all examined members, Pr. GHERJANI Rachid. In addition, Mrs. BENSOUICI Aicha Professors at the University de Constantine 1, and Mr. BELKHALFA Hakim Research Masters A at CRAPC in Ouargla agreed to judge this work,

I will not forget to thank all the members of the CRAPC Ouargla teams.

I extend my heartfelt gratitude to Pr. Nadir Dizge and his team at the Laboratory in the Environmental Engineering department at Mersin University in Turkey for the invaluable learning experience during my short-term internship. Thank you for a welcoming environment for learning and growth. Absolutely the training within your group gave me a chance to acquire experience in different systems.

My thanks also go to all the teachers, researchers, and students with whom I had the pleasure of working throughout the period of this thesis.

In our education from primary school to university.

We also extend our sincere thanks, especially to our PARENTS who helped us a lot.

Their valuable moral support and spared no effort throughout our training.

A big thank you to everyone we couldn't mention.

DEDICATION

I dedicate the fruit of my current humble work

To those who were in my heart watching us

To those who sacrificed so much for our success:

*My dear mother, **FATIMA ZOUHRA**.*

To the one who always taught me how to think before I act, to whom

Throughout my school and college life,

To those who spare no effort for a charitable cause:

*Dear **Father ABDESSALLEM**.*

*To my dear sisters: Amel, Zineb, Rekia, Thawab, Baraa, And Niamet-
Alah*

*To all the **BESRA** family and the **HAMLAOUI** family.*

*To my dear friends who accompanied me throughout this university
journey*

To all my teachers from primary to higher education.

And to everyone who is dear to me.

To beloved Algeria

Besra Safa

Table of contents

Acknowledgment	i
Dedication	iii
Table of contents	iv
List of figures	viii
List of tables	xii
<i>Introduction</i>	1-3
<i>1st Chapter. Background & Literature Review</i>	
I.1 Theoretical context of thin films and Nanomaterials	4
I.2 Materials	6
I.3 Semiconductors (SCs)	7
I.3.1 Pure Semiconductors (intrinsic)	7
I.3.2 Doped Semiconductors (extrinsic)	7
I.3.3 Coupled Semiconductors	9
I.3.4 Semiconductors and energy bands	10
I.4 Semiconductors based Metal- Oxide/Sulfide	11
I.4.1 Metal Oxide Semiconductor	11
I.4.2 Metal Sulfide Semiconductor	12
I.5 Zinc Oxide	13
I.5.1 Main ZnO characteristics	14
I.5.1.1 Structural and crystallographic properties	14
I.5.1.2 ZnO Electronic band structure	16
I.5.1.3 Intrinsic defects in ZnO	18
I.5.1.4 Electrical characteristics	18
I.5.1.5 Optical characteristics	19
I.6 Nickel Oxide (NiO)	20
I.6.1 Structural and electronic band structure properties.	20
I.6.2 Electrical and Optical properties	21
I.7 Zinc Sulfide (ZnS)	22
I.7.1 Structural and electronic band structure properties	22
I.7.2 Electrical and Optical properties	23

Table of contents

I.8 Semiconductors Applications	24
I.8.1 Gas sensors	24
I.8.2 Solar cells	24
I.9 Photocatalytic Activity Application	25
I.9.1 Photocatalysis principle	25
I.9.2 Mechanism of Semiconductor Catalysis	26
I.9.3 Photocatalysts types	27
I.9.4 Factors affecting photocatalysis degradation process (η %)	28
I.9.4.1 Effects of pollutant concentration	28
I.9.4.2 Effects of catalyst-specific surface area	28
I.9.4.3 Temperature influence	28
I.9.4.4 Wavelength effect and light intensity	29
I.9.4.5 pH Effect	29
I.9.5 Advantages of photocatalysis	30
I.9.6 Enhancing and improving Semiconductor-photocatalysis	30
I.10 Application of photocatalysis to the treatment of water polluted by Organic dyes	30
I.10.1 Organic dyes	31
I.10.2 Classification of dyes	31
I.10.3 Contaminated dyes Examples	33
I.11 Literature review of ZnO thin films photocatalyst	34
I.12 Advances in ZnO photocatalysis strategies	35
<i>2ndChapter. Film Growth Processes & Characterization Tools</i>	
II.1 Thin Films Formation	37
II.2 Mechanism of thin film formation	37
II.2.1 Nucleation stage	37
II.2.2 Growth stage	37
II.2.3 Growth Modes	38
II.3 Thin Film Deposition Techniques	39
II.3.1 Spray Pyrolysis Technique (SPT)	40
II.3.1.1 Principle of the spray pyrolysis technique	41
II.3.1.2 Spray pyrolysis process	41

Table of contents

II.3.1.3 Spray pyrolysis parameters	44
II.3.1.4 The advantages of the SPT	44
II.3.2 Sol-Gel Technique	44
II.3.2.1 Sol-Gel principle	45
II.3.2.2 Sol-Gel process	46
II.3.2.3 Spin-Coating	48
II.3.2.4 The process of the Spin-coating technique	49
II.4 Characterization tools	49
II.4.1 X-Ray Diffraction	50
II.4.1.1 Structural parameters	51
II.4.2 Fourier-transform infrared spectroscopy	53
II.4.3 Surface morphology	55
II.4.3.1 scanning electron microscopy (SEM)	55
II.4.3.2 Energy Dispersive Spectroscopy	56
II.4.3.3 Atomic Force Microscope	57
II.4.4 Optical Characterization	59
II.4.4.1 UV-Vis Spectrophotometer	59
II.4.4.2 Optical constants	60
II.4.4.2.1 Absorption coefficient	60
II.4.4.2.2 Determination of the bandgap width	61
II.4.4.2.3 Urbach Energy	62
II.4.5 Thickness measurement	62
<i>3rdChapte. Synthesis of Pure, Doped and Co-doped ZnO Metal Oxide Thin Films</i>	
III.1 Introduction	64
III.2 Elaboration of thin films	64
III.2.1 Preparation of the substrates	64
III.2.2 Preparation of thin films by spray pyrolysis	64
III.3 Results and Discussion	66
III.3.1 Optical analysis	66
III.3.2 X-Ray Diffraction study	69
III.3.2.1 Structural parameters	69

Table of contents

III.3.3 ATR-FTIR analysis	73
III.3.4 Surface morphology	74
III.4 Tested of thin films in the photocatalytic activity	78
III.4.1 Experimental protocol (Photodegradation test)	78
III.4.2 Photocatalytic degradation	78
III.5 Conclusions	81
<i>4thChapter. Doped & Coupled ZnO for Enhancing Photocatalytic Activity</i>	
IV.1 Introduction	82
IV.2 Elaboration of thin films (Thin Films Preparation Protocols)	82
IV.2.1 Single-layer Preparation by Sol-gel	82
IV.2.2 Multilayer Preparation by Spray Pyrolysis	83
IV.3 Results and Discussion	84
IV.3.1 Structural analysis by XRD	84
IV.3.1.1 Structural parameters	85
IV.3.2 ATR-FTIR study	87
IV.3.3 SEM micrographs	88
IV.3.4 AFM Analysis	90
IV.3.5 Optical analysis	92
IV.4 Application of thin films in the photocatalytic activity	94
IV.4.1 Experimental protocol (Photodegradation measurement)	94
IV.4.2 Mechanism of photodegradation behavior	95
IV.4.3 Photocatalytic degradation under visible light	98
IV.4.4 pH Effect	102
IV.4.5 Photocatalytic degradation under natural irradiation	103
IV.5 Conclusion	108
<i>Conclusions and Outlook</i>	109
<i>References</i>	111

List of figures

Figure I.1	Schematic illustration of nanomaterials classification according to dimensionality.	5
Figure I.2	CB and VB relative positions for a) Conductor, b) Insulator, and c) Semiconductor.	6
Figure I.3	Fermi level position within the E_g for a) Pure, b) n-type, and c) p-type SC.	8
Figure I.4	Schematic E_g diagram of heterojunctions SC.	10
Figure I.5	Band gap types in SC materials.	11
Figure I.6	Band positions of some typical MO/MS.	13
Figure I.7	Crystal structure of zinc oxide.	14
Figure I.8	ZnO wurtzite Crystal structure.	16
Figure I.9	Band structures of wurtzite ZnO.	17
Figure I.10	Calculated intrinsic defect levels in ZnO thin films.	18
Figure I.11	a) NiO crystal structure, b) Calculated electronic band structures of NiO.	21
Figure I.12	a) ZnS crystal structure, b) Calculated electronic band structures of ZnS.	23
Figure I.13	a) Operating principle p-n heterojunction of a photovoltaic cell, b) general schematic of the photovoltaic thin layer structure	25
Figure I.14	Schematic illustration of the photocatalytic degradation mechanism of pollutants on the ZnO surface.	27
Figure I.15	Structure of the Congo red dye.	33
Figure I.16	Structure of the Crystal violet dye.	33
Figure I.17	Structure of the Methylene blue dye.	34
Figure II.1	Schematic representation of thin film growth modes on the substrate.	39
Figure II.2	Diagram of thin-film deposition techniques.	40
Figure II.3	Schematic diagram of spray pyrolysis equipment.	42

List of figures

Figure II.4	Description of films deposited by Spray pyrolysis method.	43
Figure II.5	The two sol-gel techniques for depositing the sol onto a substrate.	45
Figure II.6	The schematic diagram of sol-gel method.	48
Figure II.7	Schematic of spin coating process.	49
Figure II.8	a) Schematic diagram of X-ray diffractometer. b) X-ray beam interacting with a sample.	50
Figure II.9	X-ray-Diffractometer in the CRAPC Laghouat.	51
Figure II.10	a) Schematic diagram of FTIR Spectrophotometer. b) Cary 660 FTIR spectrometer equipment.	54
Figure II.11	a) Schematic diagram of SEM. b) The ZEISS EVO 15 SEM equipment.	56
Figure II.12	a) Schematic diagram of AFM. b) APE Research A100 AFM equipment.	58
Figure II.13	a) Schematic diagram of UV-Vis spectrophotometer. b) Cary 100 UV-Vis equipment.	60
Figure II.14	Estimated of E_g of the thin film using the Tauc method.	61
Figure II.15	Urbach tails description.	62
Figure II.16	SEM cross-section image (show the direct thickness estimated).	63
Figure III.1	Spray pyrolysis equipment used in LRPPS laboratory (Inset shows the obtained pure ZnO film).	65
Figure III.2	a) Optical transmittance spectra, b) Optical Absorbance spectra of as deposited thin films (ZnO, Al:ZnO, Al:Ni: ZnO).	67
Figure III.3	(a-e) Tauc plot of sprayed layers, f) Variation of E_g and E_u of sprayed layers.	68
Figure III.4	a) The XRD diffraction patterns of as-deposited films, b) the corresponding JCPDS cards pattern.	70
Figure III.5	Structural parameters: crystallite size (D_{cs} , ϵ_{ms}) and δ of the sprayed films.	72
Figure III.6	Variation of the texture coefficient values for pure and doped ZnO thin films.	72
Figure III.7	ATR-FTIR spectra of sprayed films.	73

List of figures

Figure III.8	SEM surface with the histograms of grain size of as-sprayed films a) Z, b) Z1.	75
Figure III.9	SEM surface with the histograms of grain size of co-doped sprayed films a) Z2, b) Z3, and c) Z4.	76
Figure III.10	EDS spectra of undoped and doped of as-sprayed films.	77
Figure III.11	(a-e) MB UV-visible spectra under UV illumination using as-sprayed Z catalysts, f) MB Photodegradation efficiency of as-sprayed films.	80
Figure IV.1	a) descriptive diagram of the stages of deposition of the thin layers by spin coating, b) a tubular furnace was used for annealing in the CRAPC Ouargla.	83
Figure IV.2	descriptive diagram of the steps of deposition of the thin layers by spray pyrolysis.	84
Figure IV.3	a) The X-Ray Diffraction of mono and multilayer samples, b) Structural parameters	86
Figure IV.4	ATR-FTIR spectra of monolayer, bilayer and multilayer Samples.	87
Figure IV.5	SEM micrographs with the cross-sectional and EDX images of a) monolayer, b) bilayer and c) multilayer Samples.	89
Figure IV.6	The AFM images of a) monolayer, b) bilayer and c) multilayer Samples.	91
Figure IV.7	a) Transmittance spectra of the mono and multilayer samples (Inset display the band-edge absorption zone), b) Tauc plot of the mono and multilayer samples, c) Variation of E_g and E_u of signal and multi-layer thin films.	93
Figure IV.8	Schematic of the photocatalytic reactor with a visible-light lamp.	94
Figure IV.9	Proposed schematic photodegradation mechanism of multilayer photocatalyst under visible irradiation.	96
Figure IV.10	Suggested MB decomposition pathway.	98
Figure IV.11	UV-visible spectra of MB solution under visible lamp.	99
Figure IV.12	Photodegradation efficiency curves of MB with vis-irradiation using mono and multilayer photocatalysts.	100
Figure IV.13	Photodegradation Kinetics oh MB by Z and ZSN as catalysts.	101

List of figures

Figure IV.14	Recyclability of ZSN photocatalyst with MB under visible illumination.	102
Figure IV.15	The photodegradation efficiencies of various pH levels.	103
Figure IV.16	CR, CV, and MB UV-Visible absorbances spectra.	104
Figure IV.17	a-c) UV-vis curves of a) MB, b) CV, and c) CR under sunlight using ZSN photocatalyst sample, d) Degradation rate of dyes under sunlight using ZSN photocatalyst sample.	106

List of tables

Table I.1	Classification of dyes, depending on their chromophores.	32
Table I.2	The degradation efficiency of enhanced ZnO films has been reported by literature	35
Table I.3	Coupled ZnO photocatalysts has been reported by literature.	36
Table III.1	Optical parameters of as-deposited Z, Z1, Z2, Z3 and Z4 films.	69
Table III.2	Structural parameters of as-deposited Z, Z1, Z2, Z3 and Z4 films.	71
Table IV.1	Structural parameters of mono- and multilayers samples.	85
Table IV.2	$\eta\%$, time, k, and R^2 values of mono and multilayer of photocatalytic degradation performance.	105
Table IV.3	Reported degradation efficiency of coupled ZnO photocatalysts against methylene blue (MB) in literature.	107

General Introduction

Nowadays, numerous investigators have proven the exclusive properties of nano-thin layers that belong to the semiconductor material family, due to their unique properties, which have been demonstrated in both theoretical and applied studies. They are being used in many potential applications [1,2], such as gas sensors [2], antimicrobial [3], antibacterial [4], and photocatalytic activities [5]. In this regard, many semiconductor metal oxide-based materials have been investigated; particularly Zinc and Nickel Oxides have garnered interest owing to their varied characteristics. Zinc oxide is a semiconductor with an n-type and hopeful binary of the II-VI group with a broad gap ($E_g = 3.37$ eV). Zinc Oxide is suitable for photonic applications in the ultraviolet region [6]. It has two structures, a wurtzite hexagonal phase and a cubic phase [1]. NiO is a p-type semiconductor of the VIII-VI group with a NaCl structure [7], an antiferromagnetic semiconductor [8], transparent with a wide gap energy ($E_g: 3.6 \sim 4.0$ eV) [7]. Besides, nano-layer semiconductors based on metal sulfides, such as ZnS, PbS, CuS, and CdS, etc [9,10] have received significant attention due to their impressive properties [9]. ZnS is an n-type semiconductor of the II-VI group with ($E_g: 3.54 \sim 3.72$ eV) for the cubic phase and ($3.74 \sim 3.91$ eV) for the hexagonal one [11].

Currently, the world's industrial boom is driving the fast rise of environmental pollution caused by hazardous waste on a global scale. Furthermore, the continuous release of contaminants into waterways, such as organic dyes, is the most popular kind of pollution due to their ability to dissolve and stability in natural water systems, as well as their effects on aquatic and human life [12–14]. The pursuit of contemporary safe, affordable, and environmentally friendly methods to address these issues has been accelerated by the growing energy needs and environmental concerns. Because photocatalysis shows significant degradation efficiency without requiring complicated technology, it is a viable, affordable, and advantageous method for dealing with polluted wastewater. The large-scale performance of semiconductors is enhanced by their use as photocatalysts. Nevertheless, their excitement by irradiation rapidly produces electron-hole pairs, which can take part in chemical interactions and considerably challenging aspects of the photocatalytic process. The faster recombination of photo-generated pair electron-hole rate always weakens the photodegradation efficiency. Considerable research has been forward to improve semiconductors' photocatalytic performance to reduce the rate of photo-generated e-h pair recombination by several methods such as the introduction of defects, by annealing, doping, or coupling as heterogeneous (p-n) semiconductor structure, etc. Until now, pure or modified metal oxide/sulfide has been

General Introduction

synthesized with various types and morphologies of nanostructures such as powder nanoparticles [15,16], nanorods [17], core/shell type [18] and thin films. Among them, metal oxides/sulfides of the deposited thin films on different substrates are a very simple type that has a low cost-effective way of reaching techniques synthesis. Moreover, semiconductor thin films particularly the modified such as doped semiconductors e.g. Li, Al, Co, Fe, Ag [2,17,19–21], etc. Even, composite heterogeneous or multilayer structures [22–24], have improved their photocatalytic activity performance under various light source types, especially the use of Ultraviolet light irradiation. Whereas in view of the energy and environmental audits, the use of hazardous Ultraviolet irradiation is discouraged. Accordingly, many visible light active photo-catalysts with satisfying energy band requirements have been developed [25], and these photocatalysts have improved their capability under visible irradiation. Moreover, natural sunlight irradiation is seen as an excellent choice since it is a renewable source of energy, eco-friendly, and plentiful [13].

Several techniques have been used to deposit layers, including electrodeposition [26], pulsed laser ablation [27], sputtering [28], sol-gel [9], and spray pyrolysis [29,30]. Among the popular techniques, sol-gel and spray pyrolysis are easy and inexpensive methods for depositing metal sulfide/oxide layers on various substrates, such as Si, ITO, FTO, or glass substrates. In addition, thin layers provide several benefits over powder nanoparticles in the photocatalytic process, including ease of use, controllability, and avoidance of expensive powder cleaning and recycling after each degradation. In fact, selecting photocatalyst semiconductor thin layers is not only based on their intrinsic characteristics but also on the elaboration conditions that influence their obtained characteristics. Thus, to enhance and improve the photocatalytic activity of zinc oxide (ZnO), it is studied by doping it with aluminum (Al). This choice is based on the fact that Al^{3+} has a shorter ionic radius (0.053 nm) compared to Zn^{2+} (0.074 nm) [31], as previously discussed in the literature [17,32], making aluminum a promising dopant material source for ZnO. For more enhancement, the ZnO doped by Al layer can be coupled with another phase such as Al-ZnO/ZnS multilayers [33].

The aim of this study is to synthesize and characterize thin films based on functional metal oxides as photocatalysts. In addition to the introduction, conclusion, and references, this thesis is organized into 4 chapters:

First chapter is devoted to a theoretical and literature review study to get an idea for understanding the aim of the experimental results in the next chapters. Where the first part of

General Introduction

this chapter is concerned with thin films belonging to the semiconductor family and a brief description of the main properties of ZnO, NiO as metal oxide Semiconductors and ZnS as metal sulfide Semiconductors (background about materials worked on). The development of Semiconductor applications, particularly their function in photocatalytic activity applications, will also be presented. The chapter ends with a literature review of ZnO and Advances in ZnO layers as photocatalysts.

Second chapter initially presents a brief description of the thin film growth mechanism. Additionally, a detailed description of the thin film deposition methods and physicochemical characterization tools (X-Ray Diffraction and FTIR, morphological: AFM and SEM and UV-vis spectrophotometry) that were used in this work will also be presented.

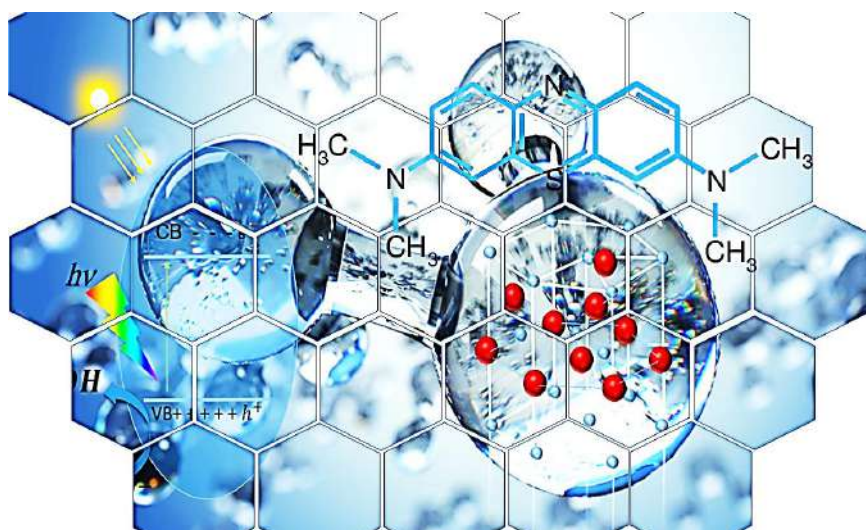
Third chapter aimed to synthesize pure ZnO, Al-doped, and Al, Ni Co-doped ZnO thin layers by spray pyrolysis method. The obtained samples were investigated using structural, morphological, and optical characterization tools. The pure and doped ZnO thin films also were tested in the photocatalytic degradation activity for methylene Blue dye under UV irradiation.

Fourth chapter intended to use inexpensive spin-coating and spray pyrolysis methods to create ZnO:Al/ZnS/NiO heterojunction multilayers as photocatalysts for the degradation of organic dyes. Tools for structural, morphological and optical analysis were used to analyze the sample characteristics.

Finally, this thesis ends with a conclusion and outlook that summarizes the essentials and the main results obtained during this study and ends with perspectives.

Chapter I.

Background & Literature Review



This chapter is devoted to a theoretical and literature review study to get an idea for understanding the aim of the experimental results in the next chapters. Where the first part of this chapter is concerned with thin films belonging to the semiconductor family and a brief description of the main characteristics of ZnO, NiO as metal oxide Semiconductors and ZnS as metal sulfide Semiconductors (background about materials worked on). The development of Semiconductor applications, particularly their function in photocatalytic activity applications, will also be presented. The chapter ends with a literature review of pure and Advances in ZnO films as photocatalysts.

Nowadays, the unique characteristics of semiconductor group nano-thin layers have been deeply investigated by several scientists, as indicated by both practical and theoretical investigations. For the past 50 years, thin layers have been used as coatings on other materials and have been employed in a variety of prospective applications. A "thin film" is defined as a layer of a material deposited on a substrate (generated by the accumulation of single atoms on a substrate via the sequential condensation of atoms, molecules, or ions), typically less than several micrometers (nanometers) thick.

I.1 Theoretical context of thin films and Nanomaterials

Thin films are grown and formed through the deposition of material on a support called a substrate; one of the dimensions (thickness) of this deposit has been significantly reduced so that it is expressed in nanometers[34]. The formation of thin films made of different materials begins with a random nucleation phase followed by the growth process. The basic film properties, like film chemical compounds, structural crystal phase, thickness, etc. are controlled by the deposition conditions. Moreover, thin films have unique properties that are not observed in bulk materials. These properties result from the film growth step on the substrates and their size effects including layer thickness, crystal orientation, and multilayer structure. Indeed, bulk materials are typically made from powders that have been compacted and heated to bond together. The powder used in this process typically has particle sizes of around 1 micrometer. Additionally, thin films can be formed from extremely small particles, which consist of individual atoms or clusters of atoms. Lastly, uniform compound materials can be created through the collision of atoms on a substrate surface, where adatoms are deposited [35].

Nanomaterials and nanotechnology have prospective applications in almost all scientific fields. The thin films are also suitable for the production of nanoscale materials.

- **Nanomaterials**

Nanomaterials are referred to as substances or components of nanomaterials found in alloys, compounds, or composites that have nanometer-size dimensions [35]. The nanomaterials are classified according to their dimensions into four types (*Figure I.1*) [36]:

0D nanomaterials: Here, all dimensions (x, y, z) are at the nanoscale. It included Nanospheres, quantum dots etc.

1D nanomaterials: Here, 2 dimensions (x, y) are in the nanoscale. This results in nanomaterials with a needle form. It includes nano- rods, fibers, tubes, and wires.

2D nanomaterials: Here, 1 dimension (x) is on the nanoscale. 2D nanomaterials exhibit plate-like shapes. It includes thin films, nanolayers, graphene, and nanocoatings of nanometer thickness.

3D nanomaterials: these nanomaterials are not confined to the nanoscale in any dimension. They consist of multiple arrangements of nanoscale crystals with different orientations. It includes dispersions of nanoparticles, bundles of nanowires and nanotubes, and multi-nanolayers (poly-crystals).

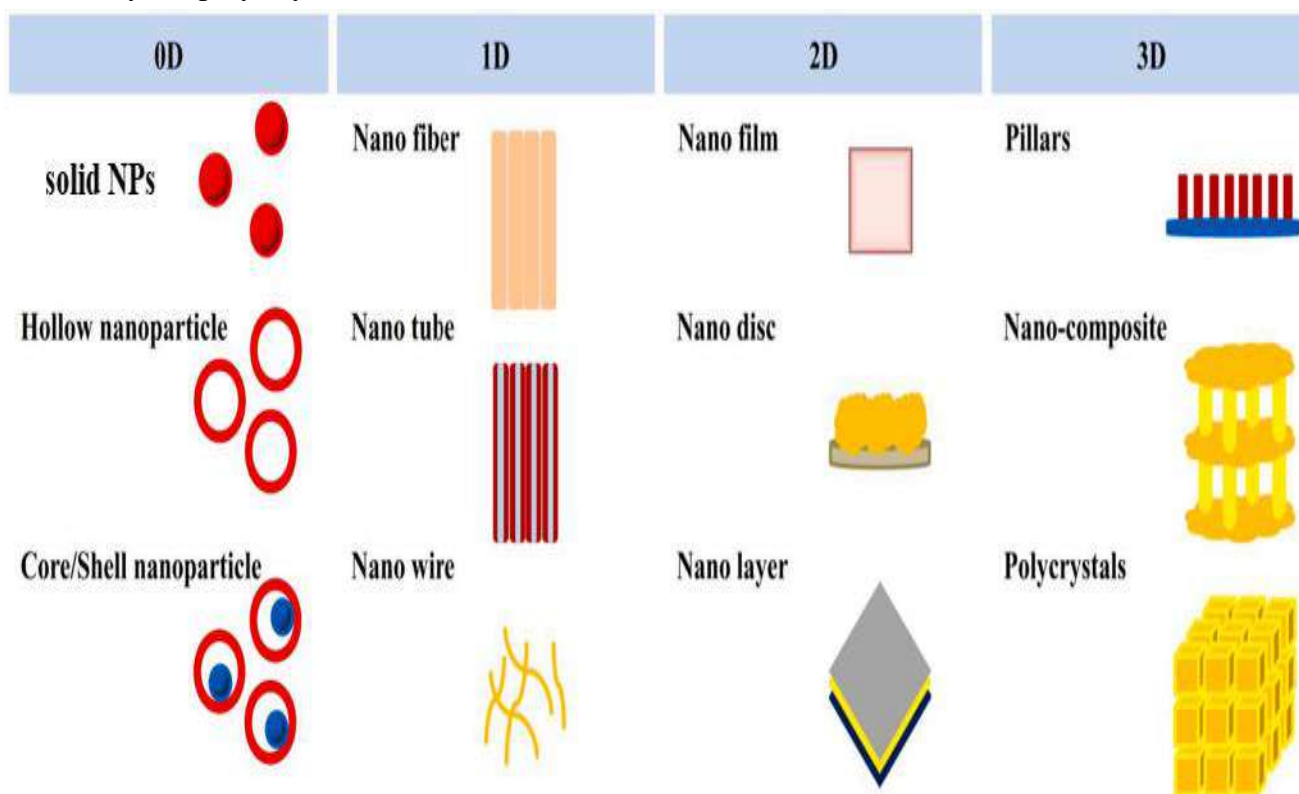


Figure I.1: Schematic illustration of nanomaterials classification according to dimensionality

[37].

I.2 Materials

Generally, in a material, the last energy band occupied by electrons is called the valence band (VB). The next energy band is the conduction band (CB). Based on the theory of energy bands, a material is said to be conductive (metal) when the conduction band and valence band overlap, or when the CB is partially filled by quasi-free electrons that can move easily under the effect of weak external excitations (electrical, optical, thermal, etc.), and thus participate in conduction phenomena. A semiconductor possesses a forbidden energy band known as the bandgap energy (E_g), which divides the valence band (VB), completely filled with electrons, from the conduction band (CB), entirely empty at absolute zero temperature. Typically, this bandgap is less than 3 eV, enabling charge carriers to transition into the conduction band through thermal excitation or upon acquiring energy equal to or greater than the bandgap ($\geq E_g$). When the gap of the material is sufficiently wide (> 5 eV), the passage of electrons in the CB becomes difficult, even under the effect of thermal agitation; in this case, the material is said to be isolated. Most transparent materials are insulators, and highly conductive materials reflect much of the electromagnetic spectrum owing to their high concentration of free carriers. Therefore, transparency, which requires a large gap and low carrier density, and conduction, which requires a small gap and high carrier concentration, cannot coexist in a single material. However, a small number of materials possess these two properties combined when they are elaborated, particularly in the form of thin layers such as Transparent and Conductive Oxides (TCOs) [36].

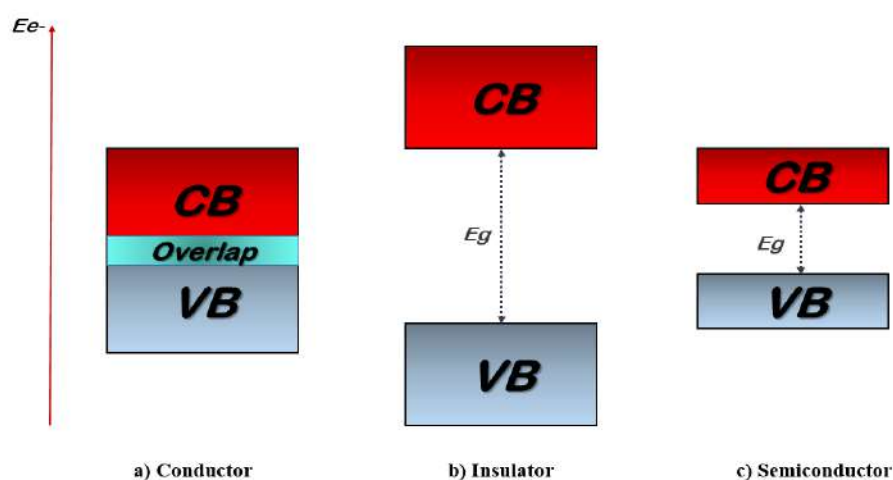


Figure I.2: CB and VB relative positions for **a) Conductor**, **b) Insulator**, and **c) Semiconductor**.

I.3 Semiconductors (SCs)

I.3.1 Pure Semiconductors (intrinsic)

The Gap Energy is a forbidden band in which electrons can only cross owing to external excitation, such as the absorption of a photon. The banned band corresponds to an energy barrier, the order of magnitude of which is the electron volts. At ambient temperature (above 0°K), the mechanism of creating an electron-hole pair occurs. These electrons become a library in the CB and can therefore move easily, leaving holes in the VB, which are also free to move [38]. The electrons present in the conduction band allow the conduction of the current. Current conduction can be viewed quite similarly in terms of electron holes moving through the valence band. The electron density (concentration per unit volume) is denoted as **n**, and that of the holes is **p**. There are no doping atoms in an intrinsic or pure semiconductor. Therefore, all electrons present in the conduction band originate from the valence band, there are as many electrons as holes ($n = p = n_i$), where " n_i " is the intrinsic concentration. The Fermi level E_f is situated in the middle of the band gap with a probability of electron occupation equal to 50% at 0K. Where E_f is defined as the level located between the VB and CB because all electrons are at their lowest energy level at 0 K. In an absolute zero, the Fermi Level is the highest energy point at which an electron can reach. The Fermi level changes as solids are heated, and electrons are provided or removed from them. One of the two types of carriers uses doping to modify the balance between electrons and holes to promote electrical conduction [39,40]. Extrinsic doping with a controlled concentration up to a very high level is necessary to obtain moderate or high conductivity.

I.3.2 Doped Semiconductors (extrinsic)

Depending on the nature of the introduced atoms, the doping procedure increases the density of charge carriers inside the SC material. Therefore, the injection of impurities in semiconductors can greatly increase their conductivity, thus producing extrinsic materials. If the electron density increases, it is n-type doping. If it increases the hole density, it is a p-type doping [38].

- There are two types of doping:

n-type doping: the purpose of n-type doping is to produce excess carrier electrons in semiconductors. If the impurity atom has more valence electrons than those of the

semiconductor matrix, for example, we consider a Si (silicon) crystal lattice, which is doped by atoms such as those of group V (VA) in the periodic table (for example, phosphorus), incorporated into the crystal lattice, which has four covalent bonds and one free electron. As a result, atoms with an extra electron to donate are called "donor" atoms (it will "donate" that extra electron to the conductivity band). In this case, the electrons are the majority carriers and the holes are the minority carriers. Thus, the materials formed are known as n-type semiconductors because they contain an excess of negatively charged electrons [36,39].

p-type doping: the purpose of p-type doping is to create excess holes. If the impurity atom has fewer valence electrons in comparison to the base semiconductor material. In this case, a silicon atom in the crystal lattice substitutes a trivalent atom, usually a boron atom. As a result, one electron is missing in one of the four covalent bonds of the adjacent silicon atoms, and the atom can accept an electron to complete this fourth bond (it will "accept" an electron from the valence band and hence it is called "acceptor"), generating a hole. The holes are the majority carriers and the electrons are the minority carriers in this state. Thus, these materials are known as p-type semiconductors [39].

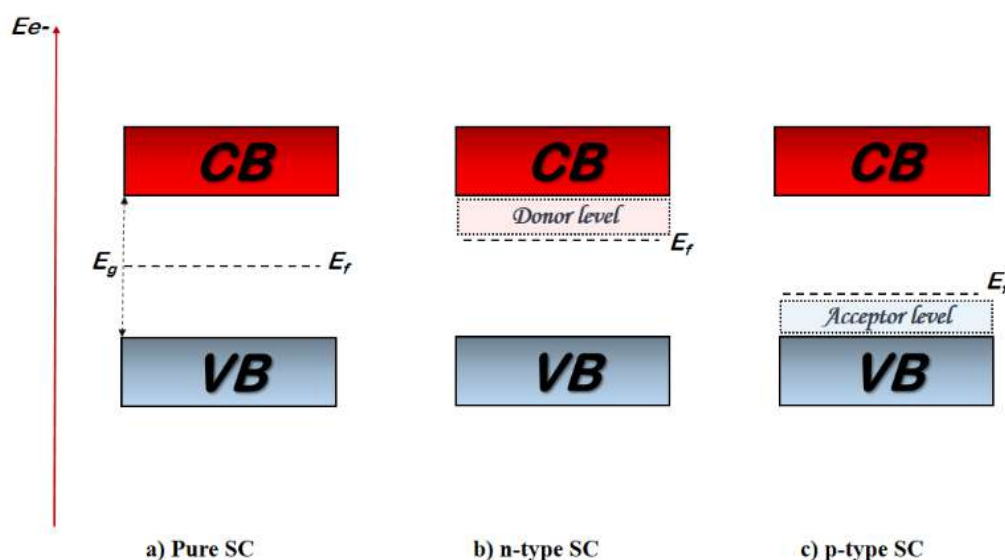


Figure I.3: Fermi level position within the E_g for a) Pure, b) n-type, and c) p-type SC.

SCs injected with a donor impurity will have a greater amount of conduction electrons (those offered by the impurity in addition to those generated by electron transitions that

migrate into the CB); thus, they are known to be n-type materials. A SC doped with an acceptor impurity is a p-type material [41]. In the doped SC, the Fermi level approaches the majority carrier band (**Figure I.3**) [38]. As a result, n-type doping produces an excess of negatively charged electrons, and the E_f level is closer to the CB. P-type doping produces an electron deficiency; therefore, an excess of holes is considered to be positively charged, and the E_f level is closer to the VB.

I.3.3 Coupled Semiconductors

The coupling of 2 semiconductor materials with different bandgap energies creates a heterostructured semiconductor. A p-n junction commonly consists of a single semiconductor material with two different doped regions: n-type and p-type. Depending on the type of doping used for the semiconductor, distinguish two heterostructure semiconductors: we have a "homojunction" (n-n/p-p), where the two semiconductors have the same type of doping. If they are composed of different doping types (n-p) of semiconductors, then it is called a "heterojunction". When a semiconductor contacts another phase exhibiting a different Fermi level, the electrons redistributed to equalize the chemical potential between the semiconductors. The Fermi levels of p-type semiconductors are lower than those of n-type. Thus, when they placed in contact with each other, electrons flow from the n-type semiconductor to the p-type semiconductor, and holes flow in the opposite direction. This causes the p-side of the junction to become charged negatively and the n-side to become positively charged, thereby creating an electric field near the junction. Semiconductor heterostructures can be classified into three different types according to their band alignment: straddling gap (**type I**), staggered gap (**type II**), and broken gap (**type III**), as shown in **Figure I.4**. The type-I structure (straddled band lineup) is the bandgap of one material that entirely overlaps with that of the other. In the type II structure, a staggered lineup is present, electrons are localized in one material, and holes are localized in other materials. Considering a type-II heterostructure, the E_c of one material is lower than that of the other. The energy gradient at the interface tends to spatially separate electrons and holes on different sides of the heterojunction, where electrons may be confined to one side and holes to another [42,43].

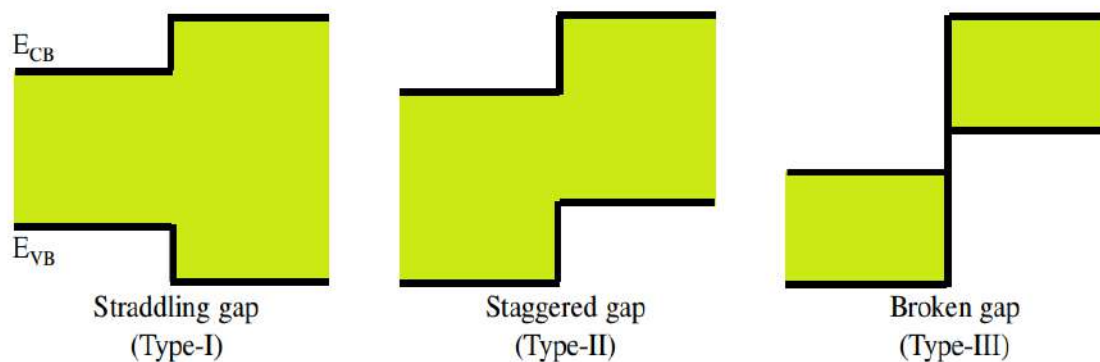


Figure I.4: Schematic Eg diagram of heterojunctions SC [42].

I.3.4 Semiconductors and energy bands

Semiconductors can also be classified into two different bandgap types according to their bandgap transition: **direct** and **indirect** (**Figure I.5**). These kinds of band structures may be defined based on wavevector k (crystal momentum). k vector describes the behavior of the electrons in the crystal lattice.

In direct bandgap SCs, like; Zinc Oxide or Zinc Sulfide, the highest energy level in the Valence-B, and the lowest level in the Conduction-B have the same vector value k . **Figure I.5** shows the energy (E) plotted as a function of the vector (k). Here, the momentum of the electrons at the minimum energy level of the CB and maximum energy level of the VB are the same. Accordingly, an energized electron can release its hold without losing energy. On the other hand, indirect bandgap SC such as Si or Ge, there is a change in the momentum of an electron between the lowest energy level of the CB and the high-energy state of the VB. An electron must thus travel through an intermediate state between the two bands (conduction and valence) in order to be able to release a photon directly. Therefore, the indirect-gap SC materials are relatively weak light emitters [44].

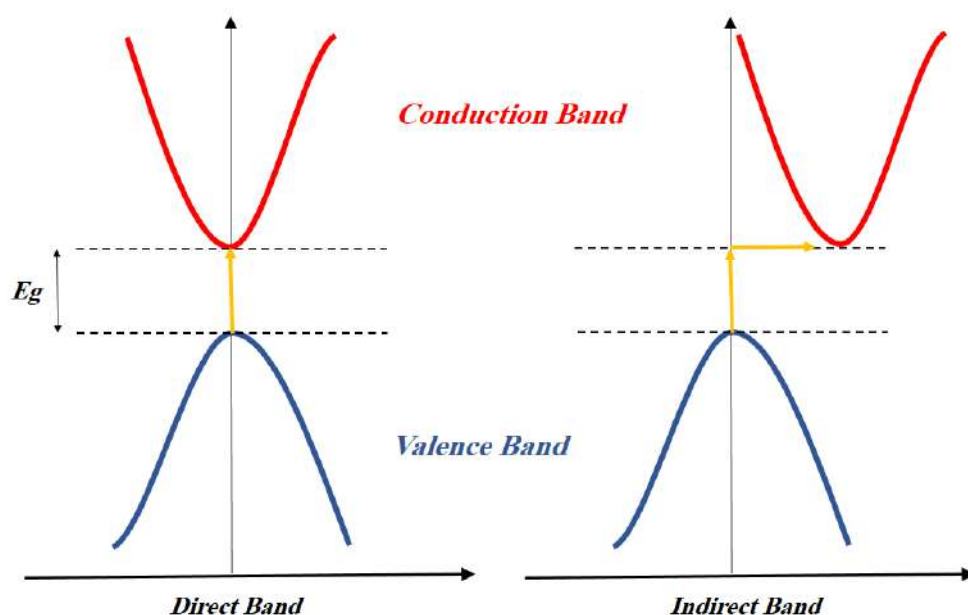


Figure I.5: Band gap types in SC materials.

I.4 Semiconductors based Metal- Oxide/Sulfide

I.4.1 Metal Oxide Semiconductor

Metal oxide (MO) semiconductors represent a unique category of materials because of their electronic charge carrier properties compared to conventional covalent semiconductors, like silicon (Si). MO semiconductors are valence compounds with high ionic-bonding ratios. The conduction band minimum and valence band maximum mainly consist of Metal M-nS and Oxygen O-2P orbitals, respectively. The interaction between the metal and oxide orbitals results in a significant disparity in the charge carrier transport [45]. The unique electronic structure of metal oxides determines their metallic and semiconductor characteristics. Metallic elements can be used to form a wide variety of oxides via several synthetic methods. Consequently, nanomaterial MO exhibits unique optical, magnetic, electrical, catalytic, optoelectronic, and photochemical characteristics [46]. Therefore, Nanotechnology opens up many opportunities because of the enhancement in the characteristics of nano-sized particles with their unique size and shape [46].

Nevertheless, Metal oxides are TCO with wide gaps. (M_xO_y) can symbolize them, where M is the chemical symbol of the considered metal, O is the oxygen symbol, and "x" and "y" are natural numbers. Generally, most transparent materials are insulators (as mentioned previously), and highly conductive materials reflect much of the electromagnetic spectrum

owing to their high concentration of free carriers. Therefore, transparency, which requires a large gap and low carrier density, and conduction, which requires a small gap and high carrier concentration, cannot coexist in a single material. However, there is a family of oxides that. In addition to being transparent, can become conductive if they have an excess of electrons in their lattices. This excess of electrons can be created either by structural defects, which introduce an imbalance in the stoichiometry of the oxide, or by appropriate doping. These oxides are known as Transparent Conductive Oxides (TCO). They have the dual properties of being good electrical conductors and being transparent in the visible range. Moreover, their large gap (3 to 4 eV) makes them conductive at room temperature and transparent in the visible region [36].

Typical TCOs belonging to SCs are two main groups, predominately **n-type** conductivity such as ZnO, TiO₂, SnO₂, In₂O₃, Al₂O₃, Fe₂O₃, etc. As well as several families are promising **p-type** SCs, including CuO, PdO, AgO₂, La₂O₃, Te₂O₃, BaTiO₃, and NiO [36]. NiO is the first known p-type TCO since 1993 [45].

I.4.2 Metal Sulfide Semiconductor

The majority of semiconductors based on metal sulfides (MS) have attracted a lot of interest because of their remarkable characteristics; however, have a negative CB, indicating a potent reduction ability akin to that of metal oxides. Additionally, because of the greater VB position that the S 3P orbital contributes compared to the O 2P orbital, most metal sulfides have poorer oxidation capabilities than metal oxides. As a result, metal sulfides often exhibit high reduction capabilities, relatively soft oxidation capabilities, and small band gaps [47]. Moreover, the holes carriers of metal oxides often have a greater effective mass than those of metal sulfides, indicating an increased holes mobility of metal sulfides for better charge transfer. This is because the O 2P state is more localized than the S 3P state. Additionally, many metal oxides have wide band gaps and can only use UV light, which accounts for only 5% of solar radiation. Metal sulfides often have a wider solar light-responsive spectrum than metal oxides, because many of them can absorb visible light (*Figure I.6*) [47].

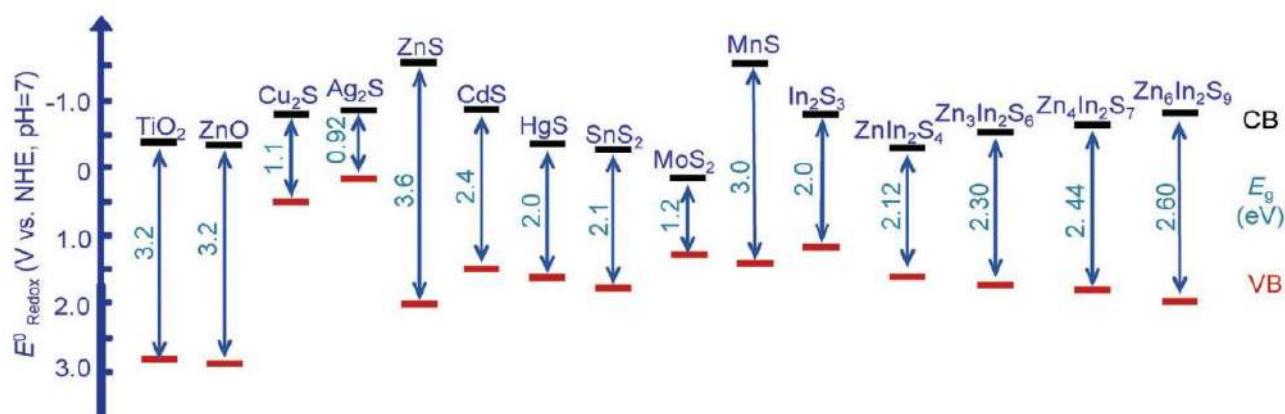


Figure I.6: Band positions of some typical MO/MS [47].

Nanostructured metal-oxide or metal-sulfide are considered to be one of the most intriguing functional materials and, hence, an active research topic. As a result, their distinguishing characteristics enable their wide use in applications such as photocatalysis for organic degradation [46], which will be improved in this work. Generally, a significant number of studies on SC MO-based materials, n-type-ZnO and p-type-NiO in particular, have garnered interest owing to their different properties. Additionally, ZnS based on MS SC has attracted significant attention due to its impressive characteristics. Therefore, **ZnO** (*in particular*), **NiO**, and **ZnS** semiconductors will be reviewed in the following part of this chapter.

I.5 Zinc Oxide

Zinc Oxide (ZnO) is an inorganic compound with the formula ZnO. ZnO has been researched as a multifunctional semiconductor for more than 80 years, starting in the 1930s. The first research, in which bulk ZnO was the primary focus, peaked at the end of the 1970s and the beginning of the 1980s. It then started to wane in part because of the challenge of doping ZnO into both the n- and p-types. However, since the middle of the 1990s ZnO has been rediscovered, and a large number of studies have been published with an eye toward its applications in optoelectronics, including light-emitting diodes, lasing, photodetectors, etc [45]. In addition to existing naturally as "zincite," ZnO may also be chemically produced in solid structure as "ZnO bulk," with varying hues depending on the impurities it contains. Moreover, ZnO appears in the solid state as an odorless off-white to pale yellow powder [48]. It is insoluble in water but soluble in acids and alcohols. The abundance and affordability of Zn metal, which makes it easier to produce and use ZnO-related materials and devices on a large scale, should be highlighted as one of the key benefits of ZnO.

I.5.1 Main ZnO characteristics

I.5.1.1 Structural and crystallographic properties

Zinc oxide is an n-type semiconductor belonging to the binary II-VI compound. The three main forms of ZnO (**Figure I.7**) are hexagonal wurtzite (P63mc space group), cubic zinc blende, and infrequently encountered cubic rocksalt (NaCl), depending on the synthesis that modifies the mixed nature of the bonds within the crystal. The last two forms of ZnO are unstable and form under high pressure (10-15 GPa), and they revert to wurtzite upon decompression.

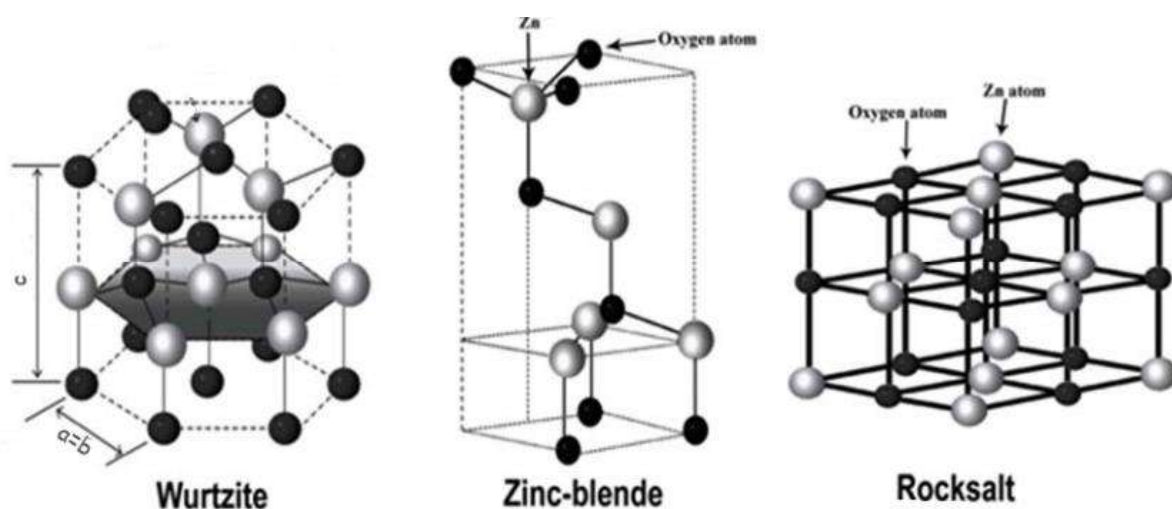


Figure I.7: Crystal structure of zinc oxide [36].

The hexagonal compact (*hc*) wurtzite structure is a more stable form of ZnO, which has a hexagonal unit cell and lattice parameters of $a=b= 3.296$ and $c=5.2065$ Å [40].

The oxygen (O) anions and zinc (Zn) cations form a tetrahedral unit and the entire structure lacks central symmetry, so it is composed of two elements with different ion radii [36].

ZnO can be directly defined as a chain of alternating planes created by tetrahedrally coordinated O^{2-} and Zn^{2+} ions, where each O (or Zn) atom is surrounded by four Zn (or O) atoms alternately stacked along the *c*-axis. The polar surface of ZnO is another important property. It has a polar (0001) surface terminated with either Zn or O. The Zn-type polarity is represented by the + *c* (0001) direction. Type O polarity is associated with direction -*c* (000-1) [40].

Chapter I. Background and Literature Review

The particular positions of the four atoms in the wurtzite structure in each cell are:

$$\mathbf{Zn}: (0, 0, 0), (1/3, 2/3, 1/2) \quad ; \quad \mathbf{O}: (0, 0, u), (1/3, 2/3, u+1/2).$$

The hexagonal lattice of the wurtzite ZnO is characterized by three lattice constants a , c , and u :

- a being the side of a rhombus constituting the base
- c the side parallel to the oz axis
- u is the interior coordinate along the axis.

These constants determine the relative positions of the O^{2-} anion and Zn^{+2} cation sublattices.

The u coordinate is defined by the following relationship Eq. **I.1**:

$$u = \frac{1}{4} + \frac{c^2}{3a^2} \quad (\mathbf{I.1})$$

According to this relationship, parameter u is dimensionless. The following Eq. **I.2** gives the distance separating the reticular planes of indices (hkl) :

$$\frac{1}{d_{hkl}} = \frac{4}{3} \left(\frac{h^2 + hk + k^2}{a^2} \right) + \frac{l^2}{c^2} \quad (\mathbf{I.2})$$

The following Eq. **I.3** determines the stability of this structure:

$$0.225 \leq \frac{R_a}{R_c} \leq 0.414 \quad (\mathbf{I.3})$$

Where R_a and R_c are the radii of the anion and cation, respectively. This condition stems from the following considerations:

For a compact hexagonal structure (hc), we have:

$$R_a + R_c = \frac{3}{8}c \quad \text{with} \quad \frac{c}{a} = 2\sqrt{\frac{2}{3}} \quad \text{and} \quad 2R_a < a \quad (\mathbf{I.4})$$

As the hc structure is derived from the face-centered cubic structure (fcc) of blende, we have:

$$\frac{R_a}{R_c} \leq 0.414 \quad (\mathbf{I.5})$$

The stacking in the wurtzite structure phase of ZnO is composed of two interpenetrating *hc* sublattices (**Figure I.8**), with alternate atomic planes stacking in the sequence ABAB along the [0001] direction [36].

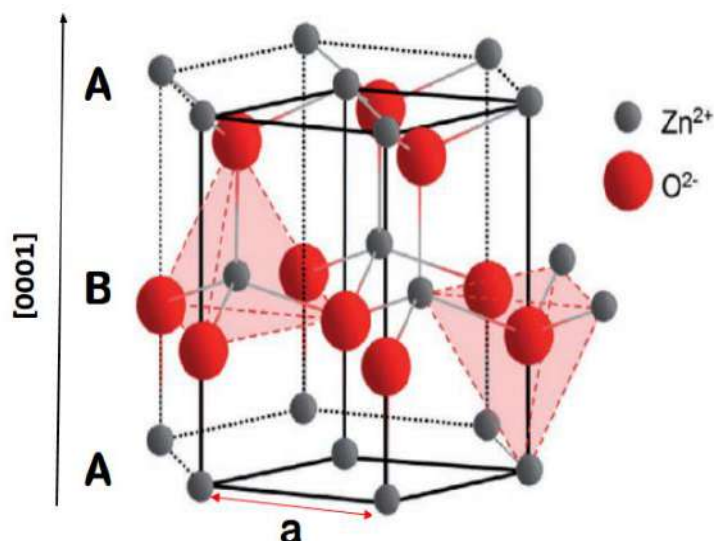


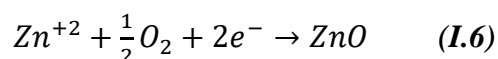
Figure I.8: ZnO wurtzite Crystal structure [49].

I.5.1.2 ZnO Electronic band structure

The electronic properties of ZnO have been the subject of several studies, including those of its band structure. The electronic structures of oxygen and zinc are as follows:



The 2P states of oxygen form the valence band and the 4S states of zinc form the conduction band of the ZnO semiconductor. Therefore, to form an ionic bond, the zinc atom must give up two electrons from the 4S orbital to an oxygen atom, which subsequently has a plain 2P orbital with six electrons. The formation reaction of ZnO is as follows Eq. **I.6**:



The theoretical studies represented in **Figure I.9** illustrate the appearance of the band structure, revealing that ZnO is in the reciprocal space at the Brillouin zone. In this structure, there are six Γ bands resulting from the 2P states of oxygen, and the lowest of the conduction bands have a strong contribution from the 4S states of zinc [50].

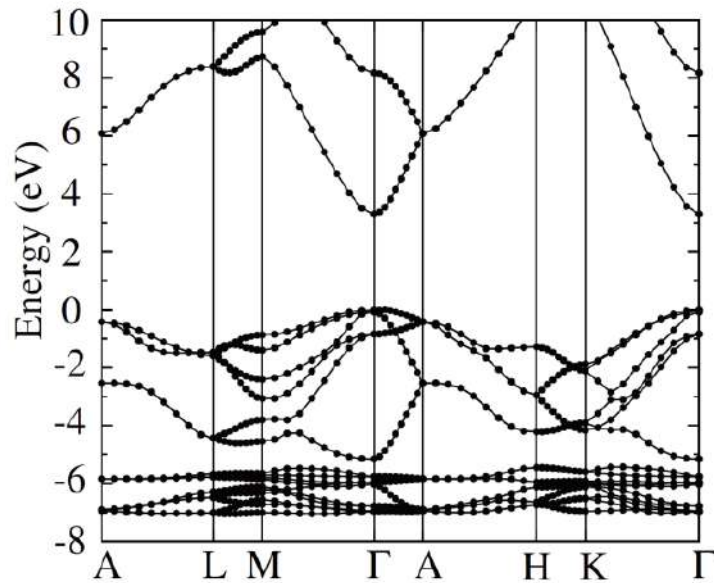


Figure I.9: Band structures of wurtzite ZnO [51].

This figure indicates that ZnO is a direct-gap semiconductor because the minimum of the conduction band and the maximum of the valence band are located on the same axis Γ (in the center of the Brillouin zone: point Γ where $k = 0$)).

As for its conduction properties, stoichiometric ZnO is insulating but becomes n-type degenerate because of the presence of systematic defects, such as oxygen vacancies and zinc atoms in the interstitial position (native defects). At room temperature, bulk ZnO has a gap of 3.37 eV, allows vertical transitions between the valence band and the conduction band (the gap corresponds to the energy required to move an electron from the BV to BC), and has radiative transitions. This value varied with temperature. When foreign atoms are introduced (doping), the nature and rate of doping vary according to the width of the forbidden band [36,50].

On the other hand, the passage of electrons from the valence band to the conduction band creates an electron-hole pair linked by a Colombian interaction within the crystalline structure (called an exciton). The binding energy of the exciton is 60 meV, which is the largest in the II-VI family [39]. At room temperature, the binding energy is greater than the energy of thermal agitation (23 meV), which means that the exciton created will not be thermally annihilated [52].

I.5.1.3 Intrinsic defects in ZnO

Typically, ZnO is an n-type conducting material. If we consider a pure stoichiometric ZnO crystal without imperfections or point/line defects and no grain boundaries at ambient temperature, ZnO would not be a semiconductor but a nonconductor [53]. The ZnO conductivity type is determined by the excess Zn atoms, which yield an electron (which can be caused by the synthesis conditions and methods). The Zn diffusion ratio in ZnO was found to be greater than the O ratio. In ZnO, there are large interstitial sites where Zn^{+2} can diffuse. Thus, the intrinsic defects in ZnO include unoccupied lattice sites, Zinc and Oxygen vacancies (V_{Zn} , V_o), interstitials (Zn_i , O_i), and antisite ZnO (O_{Zn} , Zn_o), which exhibit a range of ionization energies. Two well-known ionic defects exist: Zn_i (interstitials) and V_o vacancies. These imperfections are called "structural defects". Their energies were always located in the forbidden band. Therefore, these native structural defects in a ZnO-crystal strongly affect their electrical and optical properties that consequently have a bearing on minority carrier lifetime [53]. **Figure I.10** shows the energy levels of the intrinsic defects in the ZnO film estimated by B. Lin et al [54].

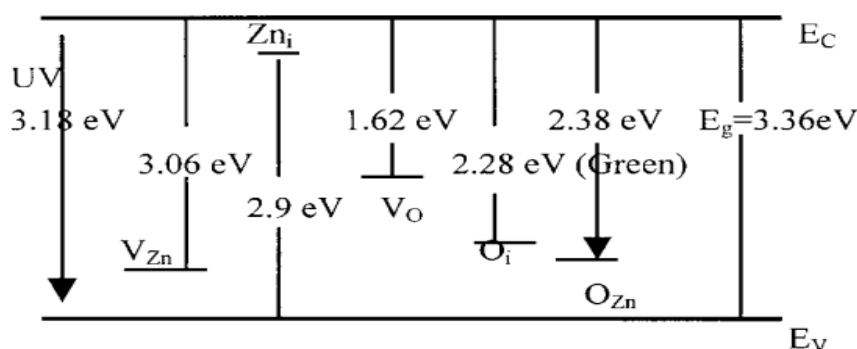


Figure I.10: Calculated intrinsic defect levels in ZnO films [54].

I.5.1.4 Electrical characteristics

The electrical properties of pure ZnO strongly depend on the synthesis technique and variation in the band gap energy (3 -3.4 eV). This can depend on the elaboration modes (a number of studies have shown that annealing after the growth of ZnO crystals can increase the intrinsic defects and thus change the electrical properties considerably) and doping rate (introduction of impurities into different ZnO lattice sites). Indeed, thermal energy can be sufficient to excite electrons from the VB to the CB, which makes ZnO an intrinsic semiconductor. The electronic transport properties of an ideal ZnO single crystal can be

described by its conductivity (σ). This conductivity is ensured by the holes created in the VB and the electrons located in the CB. As we mentioned before, ZnO has a natural n-type electrical conductivity which is due to the presence of intrinsic defects (zinc in interstitial position (Zn_i), and oxygen vacancy (V_o)). The electronic properties of semiconductors are largely related to doping by the addition or substitution of a very small quantity of atoms that constitute the network with other atoms with well-chosen properties [52].

Typically, an n-type semiconductor is formed when the concentration of electrons is higher than that of holes (these materials are obtained by n-type doping). If the doping atom belongs to the next column, it has an additional electron compared with the initial atom. Intentional n-doping is generally performed with column III elements in the substitution of zinc, in particular Al, Ga, and In, and column VII (Cl) elements in the substitution of oxygen. A p-type semiconductor occurs when the number of holes is higher compared to free electrons in a semiconductor (these materials are obtained after p-type doping). To achieve p-type conductivity, which is extremely difficult to realize compared to n-type conductivity, in particular, because of the compensation that can cause instability. This doping can be done with an element from the first column such as Li, Na, K, Cu, or Ag in substitution for Zn, or with an element from column V such as N, P, As, or Sb in substitution for O [52].

I.5.1.5 Optical characteristics

The interaction of electromagnetic radiation with solid materials (radiation-matter interaction) results in reflection, absorption, and transmittance phenomena. Parameters T (transmittance), R (reflectance), and A (absorbance) characterize these phenomena. ZnO is used today as a transparent oxide. It allows until 90% visible light when it is highly crystalline. It has an absorption threshold of approximately 360 nm, a wavelength in the ultraviolet region, which explains the value of the bandgap of this material [52]. An electromagnetic wave interacting with the semiconductor is capable associated with transferring electrons from the valence band to the conduction band if this energy is at least equal to that of the forbidden bandwidth [55].

In addition, ZnO also exhibits luminescence properties. Under the effect of an intense electromagnetic field, with an energy greater than the energy of the forbidden band (in our case, greater than 3.37 eV), ZnO emits photons, which is called photoluminescence. In practice, different emissions (bands of luminescence) can be observed, depending on the production and processing methods. In ZnO thin films, visible luminescence is due to defects related to

emissions from deep levels (virtual levels between the conduction band and valence band), such as zinc interstitials and oxygen vacancies [55]. Moreover, in thin layers, the refractive index (n) and absorption coefficient (α) vary according to the conditions under which the layers are formed. The refractive index varies between 1.7 and 2.2 [55].

According to the ZnO thin films, the transmission and reflection spectra exhibited three distinct regions [36].

- In the UV region, the transmission decreases rapidly and vanishes owing to the total light absorption towards the conduction band.
- In the visible range, the transmission is high, whereas the absorption is very low.
- In the IR region, the free carrier absorption region is characterized by high reflection and low-to-zero transmission.

I.6 Nickel Oxide (NiO)

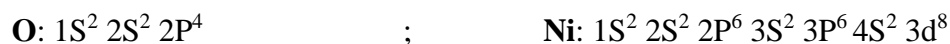
Nickel oxide has high chemical and stabilities are very resistant to oxidation. It is a transition antiferromagnetic material. Its Neel temperature is 523 K, which is the temperature that characterizes antiferromagnetic materials. Below this temperature, the sublattice atoms magnetize spontaneously like a ferromagnetic lattice and its Curie temperature is around 2000K [56].

In brief, the terms Curie temperature (TC) and Neel temperature (TN) describe the magnetic properties of certain substances. TC is the point at which some materials lose their ability to be permanently magnetic, whereas TN is the temperature above which certain antiferromagnetic materials become paramagnetic.

I.6.1 Structural and electronic band structure characteristics

NiO crystal is displayed in **Figure I.11(a)**. It is crystallizes in a known rocksalt structure (NaCl-type) face-centered cubic structure with a lattice parameter of $a = 4.177 \text{ \AA}$. This cubic structure is composed of two similar sublattices, A and B, such that any atom of sublattice A has only neighbors belonging to sublattice B, and vice versa. The anion sublattice (O^{2-}) and cation sublattice (Ni^{+2}) are *fcc* structures, the (100) plane is a mixed plane composed of 50% Ni and 50% O, and the (111) planes are alternating. The (111) face is a polar one, therefore not stable, while face (100) is a non-polar face, and therefore stable [56]. NiO is a p-type with a direct-gap

semiconductor. The electronic structures of the oxygen and nickel constituting the NiO are as follows:



The 2P states of oxygen form the VB and the 3d states of nickel constitute the CB of the NiO semiconductor. The width of its fundamental band-broad optical gap energy E_g from 3.6 to 4.0 eV [7]. Nickel oxide (NiO) is a transition metal [56]. The band structure of NiO is shown in *Figure I.3(b)*, revealing the reciprocal space in the Brillouin zone.

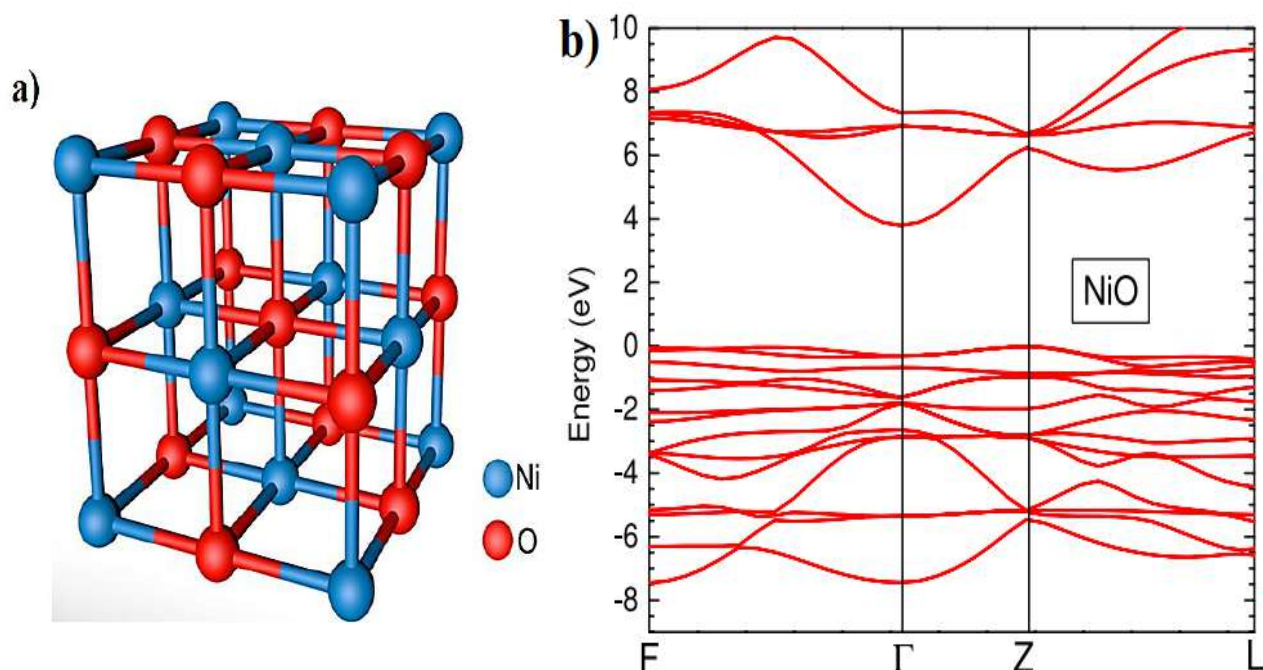


Figure I.11: a) NiO crystal structure [57], b) Calculated electronic band structures of NiO [58].

I.6.2 Electrical and Optical properties

Nickel oxide is an extrinsic p-type SC material, and the origin of p-type electrical conductivity in NiO is discussed from the point of view of nickel or oxygen vacancies. The majority of defects in the oxide are cationic vacancies, such as oxides (p-type semiconductors). NiO thin films usually exhibit p-type conduction owing to holes generated by Ni vacancies, which act as stable acceptors similar to metal vacancies in other metal oxide SCs (have low p-type conductivity according to the preparation method) [59]. Nevertheless, the V_{Ni} acceptor

level is deep, which restricts the achievable hole concentration and conductivity. Extrinsic doping techniques like exchanging Li^+ ions for Ni^{2+} ions or increasing the amount of Ni^{3+} ions were often utilized to increase p-type conductivity. Thus, the only possible conduction of NiO involves defects (native or extrinsic) in the structure [56].

The NiO material is one of the TCOs that has a p-type and direct optical band gap. The Transmittance, absorption, and bandgap of NiO thin films change depending on the preparation conditions, allowing a transmittance between 40% and 80% of visible light with a refractive index of 2.33, which makes it suitable for visibly transparent application [60,56].

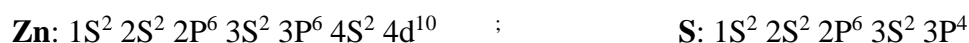
I.7 Zinc Sulfide (ZnS)

ZnS garnered a lot of attention because of its remarkable characteristics. Particularly, ZnS as a thin film has been found useful in various devices, taking wide applications. It has a wide E_g and is mostly used in optoelectronic devices, light-emitting diodes [61], and catalysts. The following is an overview of the main ZnS properties:

I.7.1 Structural and electronic band structure properties

Zinc Sulfide like ZnO is also an n-type semiconductor belonging to the binary II-VI compound that is naturally found in mineral sphalerites. Typically exists in two allotropes: the more stable zinc-blende cubic structure (F43m space group) and the wurtzite hexagonal structure (P63mc space group). The zinc-blende structure results in tetrahedrally coordinated zinc and sulfur atoms stacked in the ABCABC pattern, while the wurtzite has a structure with atoms stacked in the ABABAB pattern. The lattice parameters of wurtzite are $a = b = 3.82 \text{ \AA}$, $c = 6.26 \text{ \AA}$, and those of the zinc-blende cubic structure are $a = 5.41 \text{ \AA}$. **Figure I.12(a)** shows two ZnS structures [62].

ZnS is a direct-gap semiconductor such as ZnO (the minimum of the CB and the maximum of the VB are located at the point Γ of the Brillouin zone). ZnS electronic structures of the sulfur and zinc constituting the ZnS semiconductor are as follows:



Generally, the electronic band structure of a semiconductor is composed of a VB and CB separated by a band gap (E_g). For ZnS, the VB is essentially formed by the 3P orbitals of sulfur. Thus, the CB is composed of an overlap of the 4S and 4P orbitals of zinc. This difference in the structure induces differences in the optical and electronic properties. Indeed, the band spacings are not the same for the two structures (wurtzite, zinc blende), so the bandgap widths differ. The zinc blende (ZnS cubic stable phase) gap is of the order of 3.65 eV at room temperature, allowing vertical transitions between the valence band and the conduction band, as well as radiative transitions [63], **Figure I.12(b)** [64].

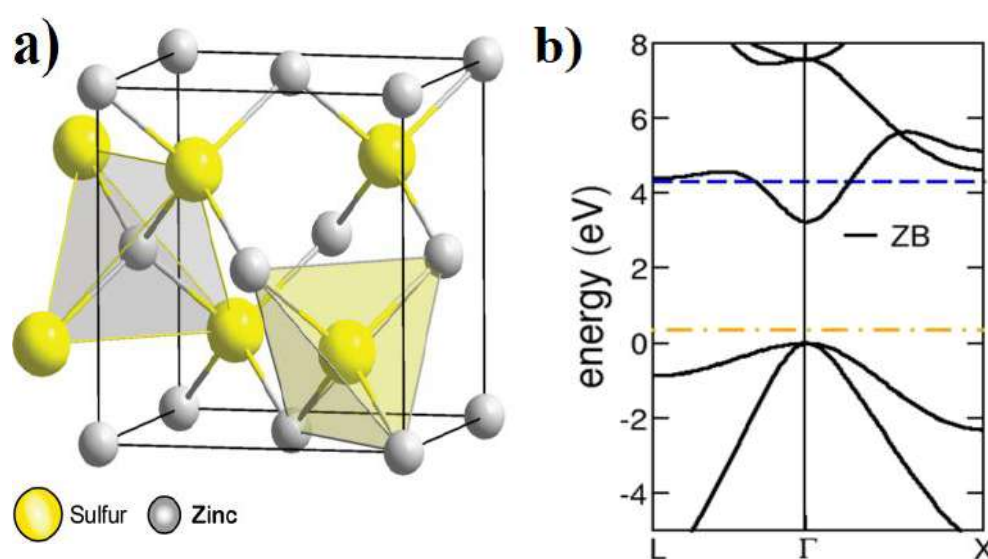


Figure I.12: a) ZnS crystal structure [65], b) Calculated electronic band structures of ZnS [64].

I.7.2 Electrical and Optical properties

ZnS is an n-type semiconductor device. Many researchers attribute this to interstitial zinc atoms and, therefore, the non-stoichiometry of the composition. ZnS crystals can be doped with Mn, Al, In, etc. Gives n-type behavior. The high conductivity of the pure sulfur layers is due to the high concentration of carriers (electrons) [44].

Zinc sulfide has a wide gap energy with good transmittance and a significant refractive index of 2.35 at $\lambda=632$ nm. Its transmittance is excellent in the visible and near-IR regions, and low in the lower wavelengths (Ultraviolet range). The high ZnS transmittance of about 90% in the visible wavelengths leads to the conclusion that the ZnS films are actually efficient transmitting and anti-reflective materials. Thus, the absorbance is low in the visible and near-

infrared regions but high in the UV region, with an enhanced absorption observed close to 360 nm [62].

I.8 Semiconductors Applications

I.8.1 Gas sensors application

As sensors play a fundamental role in monitoring environmental pollution, metal-oxide-semiconductor-based gas detectors detect changes in conductance caused by the adsorption of gases and subsequent surface reactions. As technology advances, environmental concerns are growing, and there is a need to detect various types of pollutants and toxic gases, such as carbon monoxide (CO), CH_4 , H_2S , ozone (O_3), ammonia (NH_3), etc. A gas sensor transforms quantitative or qualitative information into an electrical signal representing a chemical interaction or process between the analyzed gas and component. Semiconductor sensors consist of a layer that is sensitive to the gases to be detected. Therefore, the principle of gas detection on a semiconductor material is based on the oxidation and reduction reactions between oxygen and gas molecules, leading to variations in the electrical resistance of the material. The materials most used as detectors are oxide semiconductors [56].

The porous layers of ZnO were established as gas-sensing devices for the first time. Doping these metal oxides with noble metals such as platinum (Pt) and palladium (Pd) was discovered to be successful in enhancing their sensory abilities. Other metal oxide SC materials, like as WO_3 , are employed as gas sensors to keep an eye on environmental contaminants [66].

I.8.2 Solar cells

Generally, thin-film solar cells consist of two semiconductors: n-type (negatively charged with electrons) and p-type (positively charged with holes) semiconductors. Solar cells using p–n junctions were prepared by depositing multiple SC layers in succession. These thin-film solar cells typically include a substrate, transparent conductive oxide (TCO: generally n-type SC with high transparency in the visible range and good electrical conductivity), a window layer with high transmittance, an absorber layer with high optical absorption, and a top contact layer made of either Al or Au. A scheme of a typical p-n solar cell is shown in **Figure I.13**, where a p-n junction forms a depletion zone that creates an electric field. This electric field drives negative charges to one side and positive charges to the other side of the system, which limits the recombination of electron-hole pairs and enhances the performance of the solar cell [40].

In brief, sun cells are semiconductor-based technologies capable of converting sun energy into electrical energy. This change is caused by the photovoltaic effect of the material utilized, which allows the energy of the photons received to be captured and used to discharge charge carriers from the valence band to the conduction band [56].

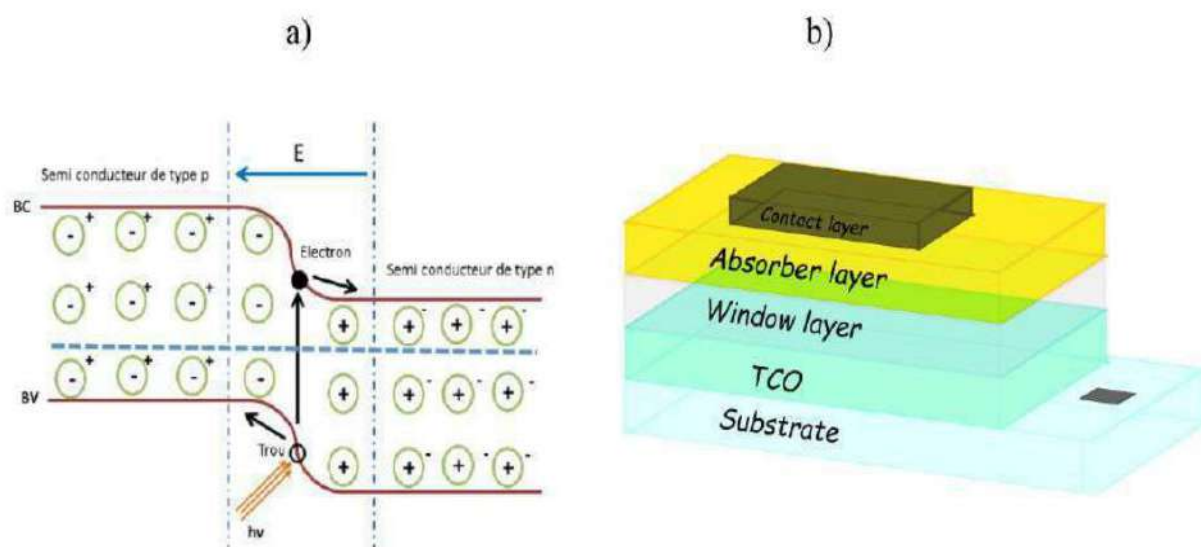


Figure I.13: a) Operating principle p-n heterojunction of a photovoltaic cell, b) general schematic of the photovoltaic thin layer structure [40].

I.9 Photocatalytic Activity Application

This method is use light and SCs. It is non-toxicity or secondary pollution causes. In 1972, Fujishima and Honda first reported the production of hydrogen by water splitting using an n-type TiO_2 semiconductor photocatalyst [67]. The photocatalytic activity of the photocatalyst dominates the performance of the photocatalytic process. The ideal photocatalyst should have a lower recombination rate, safety, improved charge separation, higher visible light efficiency, and good stability. In addition, it is possible to use semiconductor photocatalysts for sterilization, air purification, wastewater treatment, etc [44].

I.9.1 Photocatalysis principle

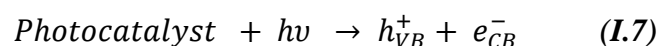
Photocatalysis is the process of using a semiconductor photocatalyst to convert organic matter into carbon dioxide and water by capturing sunlight or any incident light. This process can eliminate environmental pollutants through light-induced redox reactions known as

photocatalysis. When the surface of the photocatalyst is exposed to photon energy equal to or greater than the band gap energy, it agitates electrons from the VB to the CB, resulting in the formation of electron-hole pairs in both bands. The formation of positive holes in the valence band leads to the oxidation of pollutant or water molecules, producing hydroxyl radicals. Those excited electrons reduce the adsorbed oxygen on the photocatalyst. In the conduction band, excited electrons have a strong reduction ability to react with dissolved molecular oxygen in water or adsorbed oxygen on the surface of the photocatalytic material.

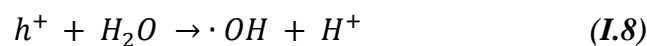
I.9.2 Mechanism of Semiconductor Catalysis

In the photocatalytic process, incident light interacts with the photocatalyst, causing (on a femtosecond time scale) the generation of electron-hole pairs (e^-/h^+) if the energy is equal to or greater than the bandgap (E_g) of the semiconductor material. The bandgap is an energy barrier between the valence band (VB, the highest energy band occupied by electrons) and the conduction band (CB, the lowest energy band occupied by electrons). The photocatalytic mechanism involves the generation of hydroxyl radicals ($\bullet\text{OH}$) and superoxide anions ($\bullet\text{O}_2^-$). Among these, $\bullet\text{OH}$ has a high oxidation potential and acts as a major oxidizing species. Both $\bullet\text{OH}$ and $\bullet\text{O}_2^-$ act as oxidants that degrade organic compounds. After mineralization, the organic pollutants yielded less harmful CO_2 and H_2O as reaction products [44], (**Figure I.14**).

In the case of organic contaminants, $\bullet\text{OH}$ free radicals react with organic pollutants and convert them into non-hazardous forms. The exciting and reducing agents are the photon energy required to excite the electrons, which results in h^+_{VB} and e^-_{CB} .

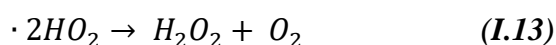
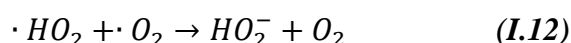
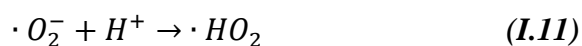


Hydroxyl radical formation



Superoxide radical anions and hydroperoxide radicals are produced when oxygen is reacted with





Degradation of organic pollutants by hydroxyl radicals [68].

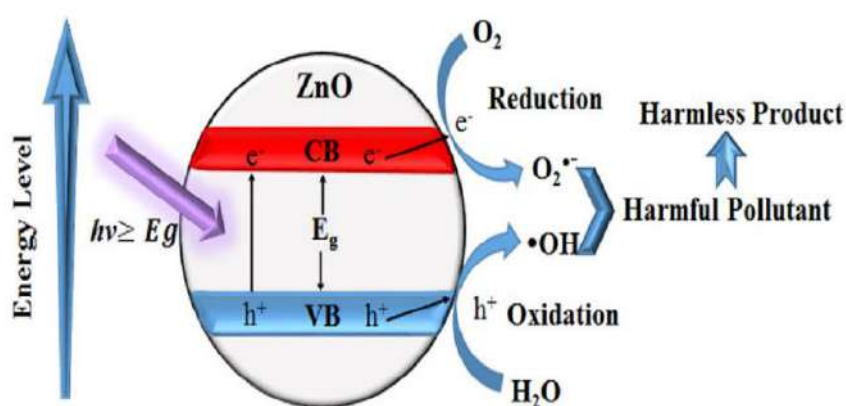


Figure I.14: Schematic of the photocatalytic degradation mechanism of pollutants on the ZnO surface [69].

I.9.3 Photocatalysts types

There are two types of photocatalysts based on mobility: mobilized photocatalysts (in *powder* form) and immobilized photocatalysts (*thin films*). The immobilized photocatalyst is cost-effective and easily recycled after washing compared to powdered photocatalysts owing to recycling and aggregation difficulties due to the higher powdered photocatalyst loading. Thin-film photocatalysts have several advantages over powder photocatalysts, such as a relatively favorable price due to reduced material usage, avoidance of costly recycling and recovery after degradation, less physical impairment, comparatively better long-term performance, and easy incorporation into various devices by simply adjusting their hardware properties and enabling miniaturization of devices. Many researchers have reported the synthesis of immobilized photoelectrodes [44].

An ideal photocatalyst must possess the following properties:

- Reduced recombination.
- Improved charge separation and charge transport.

I.9.4 Factors affecting photocatalysis degradation process (η %)

The photocatalytic degradation performance is largely influenced by several parameters, including the following factors:

I.9.4.1 Effects of pollutant concentration

In general, the degradation rate decreased with an increase in the pollutant concentration while maintaining a fixed quantity of catalyst. This can be rationalized on the basis that as the pollutant concentration increases, more organic substances are adsorbed on the photocatalyst surface, while fewer photons are available to reach the catalyst surface; therefore, less \bullet OH is formed, resulting in a lower degradation [44].

I.9.4.2 Effect of catalyst-specific surface area

The degradation of the dye is affected by the size and quantity of the particles, which are inversely proportional to the specific photocatalyst surface area. The photodegradation of the dyes increased with increasing catalyst loading. Increasing the amount of catalyst led to an increase in the number of active sites on the surface of the photocatalyst, thus causing an increase in the formation of numerous \bullet OH radicals, which can participate in the decolorization of the dye [44].

I.9.4.3 Temperature influence

It is often change in the photocatalytic system is not necessary, almost a process of photo activation and most photon reactions are insensitive to slight changes in temperature. The increase in the reaction temperature was proportional to the increase in the photocatalytic activity. Conversely, when the reaction temperature is above 80 °C, charge carrier recombination is preferred and adsorption is disfavored [70]. The optimal temperature is generally between 20 and 80°C. In this area, increasing the temperature activates photocatalytic decomposition. For example, an increase in temperature from 12 °C to 57°C increases the rate of decomposition of 4-chlorophenol (*Hofstadler et al. 1994* [71]). At low and high temperatures, the reaction rate decreased. Therefore, the photocatalytic reactor devices must be cooled [72].

I.9.4.4 Wavelength effect and light intensity

The "photo" prefix in the "photocatalysis" word is reverting to light. Without light irradiation, the process can be categorized as a catalytic process. Hence, the existence of light is necessary for the photocatalytic activity process and the degradation rate is directly proportional to the irradiation intensity [73].

Photocatalyst SCs with wide band gaps (ZnO, ZnS) may require excitation energy in the UV region (leading the electrons to jump from the VB to the CB and leave holes). The wavelength and intensity of the ultraviolet light irradiation source affect the pollutant degradation in an aqueous solution using these catalysts in a photocatalytic reactor [74].

Solar energy is expected to emerge as an alternative cost-effective light source because of its abundance and non-hazardous nature. Usually, solar photocatalytic degradation reactions can be performed directly using solar illumination [74].

I.9.4.5 pH Effect

The photodegradation of dyes is affected by the pH of the solution. The variation in the solution pH changes the surface charge of the photocatalyst particles and shifts the catalytic reaction potential. Consequently, the adsorption of the dye on the surface was impaired, thereby causing a change in the reaction rate. Depending on the pH of the solution, the surface of the catalyst has a positive, negative, or neutral charge. The case of zero catalyst surface charge is called the Zero Charge Point (PZC) or Isoelectric Point (IEP) [44,70]. Several studies have investigated the influence of pH on photocatalytic degradation.

Neatly, points of zero charge (PZC) are defined as pH values for which one or more of the surface-charge components are equal to zero at specified conditions of temperature and aqueous solution composition. This does not mean that there is no charge, but that there are equal amounts of negative and positive charges. The emphasis on pH is due to the large range of proton concentrations in solutions and the fact that the complexation of H^+ and OH^- at the surfaces of particles strongly affects the adsorption of other cations and anions [75]. For example, *N. S. Jyothi et al* [76] . Found the PZC of the ZnO film to be maximum at pH=8.1. Therefore, above this PZC, the surface of the ZnO is negatively charged, and hence a strong Coulombic charge interaction occurs between the surface of the catalyst and the MB (cationic) dye molecules.

I.9.5 Advantages of photocatalysis

Among the many advantages of photocatalysis [44,70], citing the

- Photocatalysis is a destructive and non-selective technology
- A potential for total mineralization through the formation of H₂O, and CO₂.
- Can operate at ambient temperature and pressure
- Non-toxic, low requirement, and active in various physical forms
- Effective with low pollutant concentrations
- Does not require high energy consumption.
- Exhibited considerable degradation efficiency without involving complex technologies
- An effective cheap beneficial and green technology (by using solar light).

I.9.6 Enhancing and improving Semiconductor-photocatalysis

The excitement of SCs by irradiation creates e-h pairs that can take role in a chemical interaction. The faster recombination of the photogenerated e-h pairs always weakens the photodegradation process. For enhancing it, the photo-generated pair recombination must be reduced, which was improved by divert methods: adding surface defects, doping SC, coupling this SCs heterojunction structure, etc.

As was mentioned before, doping or coupling SCs can make the band gap be moved through suitable to shift VB up or CB down. In addition, intermediate energetic states can be introduced for effective absorption under visible and solar-light irradiation. Moreover, SC thin films, particularly modified structures. They improved the photocatalytic activity under various light source types. Furthermore, in view of energy and environmental audits, the use of hazardous UV irradiation is discouraged; accordingly, many visible-light-active photocatalysts satisfying energy band requirements have been developed. Enhanced photocatalysts have shown improved capabilities under visible/solar irradiation. Moreover, natural solar light irradiation energy is considered an excellent choice because it is a renewable, friendly, and plentiful source of energy.

I.10 Application of photocatalysis to the treatment of water polluted by Organic dyes

Here, we are interested in the degradation of dyes in polluted water using photocatalysis. In view of their widespread use in industry (textiles, cosmetics, etc.), we chose to study the degradation of dyes in an aqueous medium.

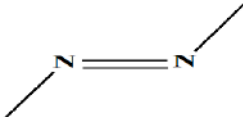
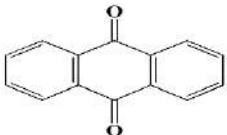
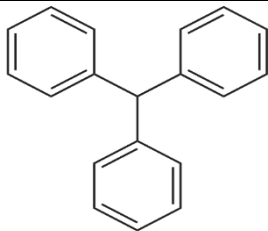
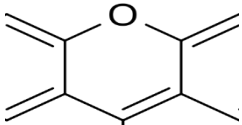
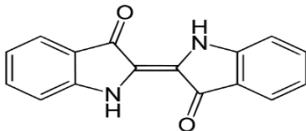
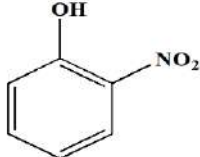
I.10.1 Organic dyes

They are generally complex compounds that are resistant to different processes such as the action of detergents or exposure to light. Until the 19th century, most dyes came from natural sources, such as plants and insects, and were generally produced on a small scale. The discovery of the first synthetic dye, "mauveine", in 1856 marked the beginning of the era of synthetic and large-scale dye manufacturing. Synthetic dyes are widely used in various industries, such as textiles, pulp and paper, leather tanning, food processing, plastics, cosmetics, rubber, and printing [44]. On the other hand, the washing of tinted or printed textile articles/fabrics produces a large volume of liquid effluents laden with these dyes and pigments in variable proportions (10–60 %), causing a waste of dyes per year, and chemical products and auxiliaries such as phosphates and nitrates, which have direct effects on aquatic fauna, flora, and human health [77].

I.10.2 Classification of dyes

There are several ways to classify dyes based on their chemical structure, ionic charge, and applications. Also classifies dyes based on their ionic charges and provides chemicals. The chemical classification of dyes revolves around the chemical structure and, more specifically, the nature of the chromophore present in the dye molecules. Dyes are classified into the following main types (*Table I.1*).

Table I.1: Classification of dyes, depending on their chromophores [44].

<i>Azo dyes</i>	
<p>belong to the (-N=N-) group consisting of azo chromophores, which form bonds between alkyl and/or aryl groups. Depending on the number of chromophores whether the dye is monoazo, diazo, or polyazo. It is known for its binding properties with cellulose fibers and is therefore widely used in dyeing.</p>	
<i>Anthraquinone dyes</i>	
	<p>Among the most commonly used dyes in the industry, after azo dyes. It is composed of a chromophore with a nucleus and carbonyl bonds, on which one part is added and the other hydroxyl or amine groups [77].</p>
<i>Triphenyl methane dyes</i>	
<p>Generally obtained from diphenylmethane or triphenylmethane, which are derivatives of methane, where substituted phenyl groups replace the hydrogen atoms and each group carries at least one oxygen or nitrogen atom in the para position with respect to the methane carbon. Thus, diphenyl-methane is used for coloring paper, jute,...and leather.</p>	
<i>Xanthene dyes</i>	
	<p>Xanthene dyes are rarely used in dyeing because of their strong fluorescence when excited under ultraviolet light. These dyes are composed of a pyran ring in the center surrounded by two benzene rings.</p>
<i>Indigo dye</i>	
<p>The indigo colors tend to be the names of the indigo of the base mole of this family. The chromophore of the molecule was composed of released molecules and their bonded carbonyls (>C=O).</p>	
<i>Nitro and Nitroso dyes</i>	
	<p>These colors present a nitro (-NO₂) group in the ortho position by reporting to a group of electrons (hydroxyl or amine groups). These nitrite components contain anionic or discrete pigments, with limited yellow and brown nuances.</p>

I.10.3 Contaminated dyes Examples

Congo red (CR) is one of the most commonly used azo dyes. It contains a double azo bond (-N=N-) and is a diazo-benzidine-based anionic dye. Maximum absorption wavelength at $\lambda = 498$ nm. CR is both toxic and carcinogenic. The complex aromatic molecules of CR offer physicochemical stability, which makes biodegradation difficult. Therefore, the presence of CR dye in water is extremely undesirable, even at low concentrations, because of health concerns. [78].

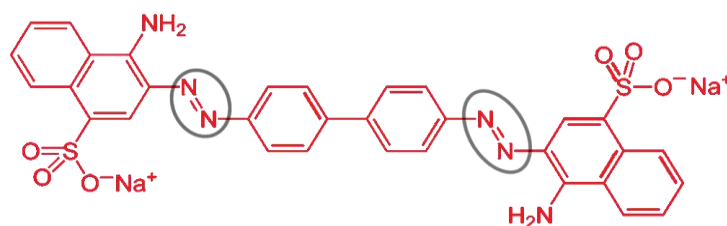


Figure I.15: Structure of the Congo red dye.

Crystal violet (CV) belongs to the class of triphenylmethane dyes. The maximum absorption wavelength was close to 583 nm. It is employed as a bacteriostatic agent in medicine and is the major ingredient of the Gram stain. CV is used as an external skin disinfectant in both humans and animals. It is frequently used as a purple dye in cotton fabrics and printing inks. The dye can permanently harm the eye cornea and conjunctiva and is responsible for unpleasant photosensitivity. The product contained a cationic dye, which has been shown to be hazardous to mammalian cells in several studies. It can be absorbed through the skin in dangerous amounts. All the aforementioned negative impacts led us to investigate how to remove it from wastewater [79].

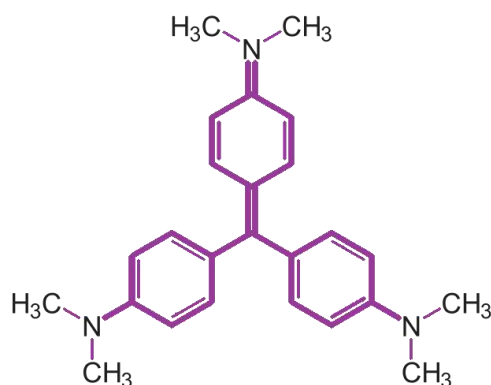


Figure I.16: Structure of the Crystal violet dye.

Methylene blue dye

In this work, methylene blue MB was chosen as the main model for organic dyes. MB ($C_{16}H_{18}ClN_3S$) is a cationic [80], bright greenish-blue organic dye with a maximum absorption wavelength of $\lambda = 664$ nm. One of the artificial colors used extensively as colorants is MB. Additionally, the food, cosmetics, and pharmaceutical industries consume large amounts of MB for their production. In reality, the safe use of MB, in accordance with clinical advice or prescription, has been shown to have some therapeutic effects, in contrast to consumption through contaminated water. However, the release of MB dye can cause many health risks and requires effective removal prior to industrial discharge [81].

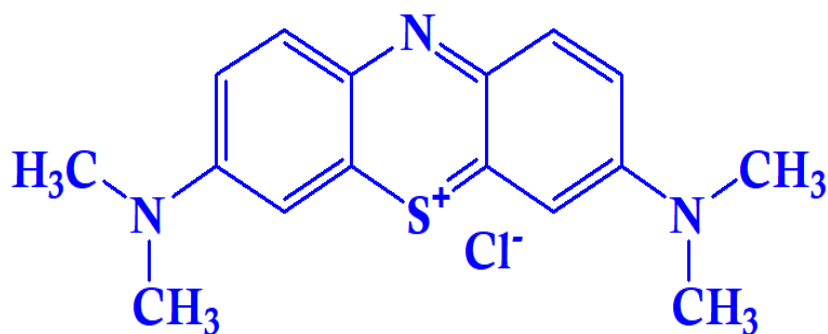


Figure I.17: Structure of the Methylene blue dye.

I.11 Literature review of ZnO thin films photocatalyst

The energy of the occupied photon must be equivalent to or greater than the forbidden bandgap of the selected semiconducting photocatalyst in the photocatalytic mechanism to excite e^- into the CB and produce charge transporters. Among metal oxide photocatalysts, ZnO has a larger negative CB potential, making it the best contender for restricting water and CO_2 . Usually, pure ZnO E_g requires irradiation in the ultraviolet region. Under natural sunlight irradiation, ZnO is excited merely by the energy of UV light, which accounts for only 5% of the total sunlight irradiation. Thus, ZnO is not photocatalytically active at longer wavelengths, except when the synthesized ZnO thin films exhibit native defects, which can make them efficient, even under visible irradiation. Consequently, the ZnO band structure may be altered through doping, the creation of nanocomposite materials, and heterojunctions with other semiconductors. These modifications can significantly improve the light-harvesting potential of ZnO, resulting in improved photocatalytic performance [82].

I.12 Advances in ZnO photocatalysis strategies

The significant improvements in the ZnO thin films are described. They are:

- ✓ Doping with cationic dopants like Al, Co, In, Ag, Li, and Cu.

Tabel.I.2: The degradation efficiency of enhanced ZnO films has been reported by literature

<i>Dopant</i>	<i>Deposition tec.</i>	<i>Illumination setup</i>	<i>Organic contaminant</i>	<i>Degradation time/efficiency</i>		<i>ref</i>
				<i>pure</i>	<i>enhanced</i>	
<i>Al (6%)</i>	Sol-gel on glass sub.	UV 15W	MB/ 8ppm	380min/ 60%	380min/ 80%	[83]
<i>Al (2%)</i>	Sol-gel on glass sub.	Sunlight	Phenol/ 10ppm	300min/40%	300min/80%	[32]
<i>Al (5%)</i>	Spray pyrolysis	UV 7 W	MO/	5h /90%	3h /90%	[84]
<i>Al (25%)</i>	Spray pyrolysis	UV 9 W	MO/ 10 ⁻⁵	180min /60%	180min /90%	[85]
	Spray pyrolysis	Sunlight	MO/ 10 ⁻⁵	180min /60%	180min /100%	
<i>Ag (5%)</i>	Spray pyrolysis	LED 17 W	50ml/10ppm	2.7%	45.1%	[86]
<i>Co (1%)</i>	Spray pyrolysis on PEI substrate	UV 100 W	CV	210min/86%	210min/91,3%	[19]
	Spray pyrolysis on PEI substrate	Sunlight	CV	210min/78%	210min/85%	
<i>In (1%)</i>	Spray pyrolysis on PEI substrate	UV 100 W	CV	210min/86%	210min/85%	[19]
	Spray pyrolysis on PEI substrate	Sunlight	CV	210min/78%	210min/88.5%	
<i>Li (2%)</i>	Spray method	UV	RhB	90min/20%	90min/86%	[2]
	Spray method	UV	MB	90min/27%	90min/43%	
<i>Cu</i>	electrochemical deposition on ITO	UV lghit 30W	MB/10um, 25ml	150min/74%	150min/95%	[26]
			MO/10um, 25ml	150min/67%	150min/81%	
			CR/10um, 25ml	150min/39%	150min/67%	

- ✓ Development of photocatalytic degradation by the coupling of ZnO thin films with other phases such as heterogeneous p-n nanocomposite (coupled CuO–ZnO) or multilayer (ZnO/ZnS, ZnO/AZO/ZnO).

Table.I.3: Coupled ZnO photocatalysts has been reported by literature.

<i>Dopant</i>	<i>Deposition tec.</i>	<i>Illumination setup</i>	<i>Organic contaminant</i>	<i>Degradation time/efficiency</i>		<i>ref</i>
				<i>pure</i>	<i>enhanced</i>	
<i>Coupled CuO 75%-ZnO</i>	Spray Pyrolysis on glass sub.	Sunlight	MB/50 ml	-	3h/99%	[87]
<i>ZnO/AZO/ZnO</i>	spin coating	Visible light 750 W	40 ml/ 30mg/l	-	3h/95.2 %	[5]
<i>Al-ZnO/ZnS</i>	spin coating	100 W mercury lamp	20 ml	60min/25%	60min/98%	[33].

Chapter II.

Film Growth Processes & Characterization Tools



This chapter initially presents a brief description of the thin film growth mechanism. Additionally, a detailed description of the thin film deposition methods and physicochemical characterization tools that were used in this work will also be presented.

II.1 Thin Films Formation

The concept of the thin film formation process is the solubility relaxation phenomenon. The atomic process of film growth in the deposition time permits the doping and alloying of films. This enables the production of custom materials with desired characteristics, which adds a new development in the domain of material technology [35].

II.2 Mechanism of thin film formation

Thin films can be synthesized on substrates through various methods, including physical approaches such as irradiation with energetic species or photons for evaporating source materials, as well as chemical methods involving thermal evaporation and chemical decomposition of dissolved precursors. Each technique for depositing thin-film materials typically involves three main steps [78]:

- Creating suitable ionic, molecular, and atomic species.
- Transfer or deposit of created elements to the substrate.
- Condensing on the same substrate to form the solid deposition, this step often passes through nucleation, coalescence, and growth.

II.2.1 Nucleation stage

Nucleation is a process that accompanies the changes in the matter's state and involves the appearance, inside a specific environment, of transformation points from which a novel substance or chemical structure grows. Species that reach the substrate lose their component normal to the substrate due to their velocity and are physically adsorbed on the substrate surface. These species are not in thermodynamic equilibrium with the substrate and move over their surface. Therefore, they interact with each other and form clusters. These clusters, also known as nuclei, are unstable and tend to desorb, depending on deposition conditions. They began to expand when they collided with other adsorbent species. Once the clusters reached a threshold size and crossed the nucleation barrier, they became thermodynamically stable [53,88].

II.2.2 Growth stage

Up until they achieve the maximal nucleation density, the nuclei increase in size and quantity. The average size of the nuclei and the nucleation density, called islands, depend on certain parameters that strongly relate to the deposition technique such as the energy and rate of the flowed species, activation energy, thermal diffusion, substrate temperature, topography,

and nature of the substrates. The nucleus may expand perpendicular to the substrate through the surface diffusion of the adsorbed species or perpendicular to it through the direct flow of the incident species. Generally, the lateral growth was much more significant at this stage than the perpendicular growth; this can also depend on the deposition conditions. The last step in the film-forming process is the coalescence stage. To obtain a uniform film and cover the surface area of the substrate, the formed islands begin coalescing with each other to form larger island agglomerations, which can be enhanced by increasing the surface mobility of the adsorbed species. Moreover, surface mobility can be improved by increasing the substrate temperature. Furthermore, the sparse agglomeration or larger islands still grow but may leave holes and channels in the substrate (making defects and voids in the depositing film network). This stage involves the transition of the film structure from a porous network type to a discontinuous island type. The holes and channels in the film were closed and covered to create a continuous film [53,78].

II.2.3 Growth Modes

When material B is deposited on support A, this film growth is experimentally a non-equilibrium kinetic process, in which the rate-limiting steps affect the net growth mode. Three growth modes were observed. These modes are named according to their original investigators as follows:

Layer-by-layer, or two-dimensional (2D) growth mode, where material B deposits an atomic layer after the atomic layer on A, is commonly referred to as the Frank-Van der Merwe (FM) growth mode. In this case, the film atoms were more strongly bound to the substrate than to each other [89].

Island, or the three-dimensional (3D) mode of growth, where material B grows in 3D islands directly on the A surface. This mode is called the Vollmer-Weber (VW). In this case, the film atoms were more strongly bound to each other than to the substrate [89].

The layer-plus-island or mixed mode is called the Stranski-Krastanov (SK) growth mode. SK represents a mixed case between FM and VW growth, which starts with 2D growth and then becomes 3D after a certain critical thickness. All these modes are presented in *Figure II.1* [89].

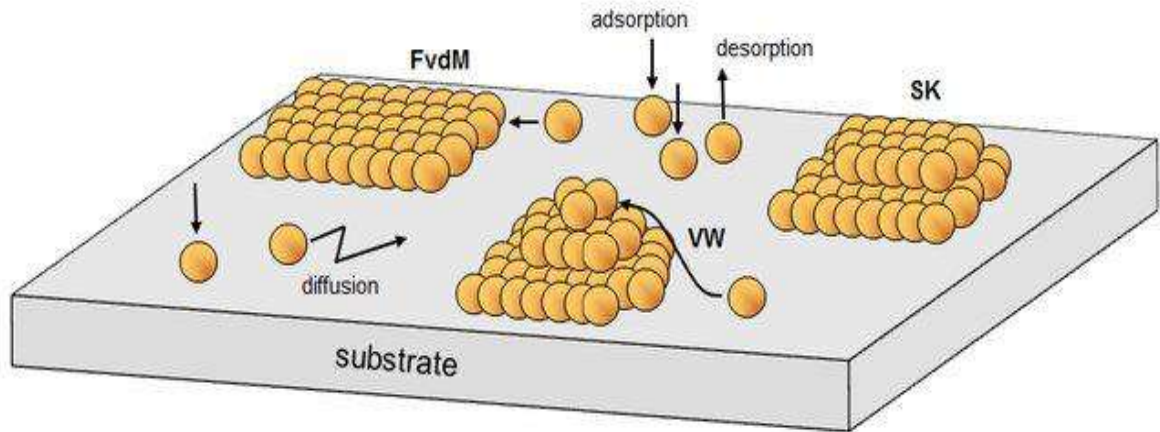


Figure II.1: Schematic representation of film growth modes on the substrate [53].

II.3 Thin Film Deposition Techniques

Thin films are generally deposited to provide particular characteristics, such as electrical, optical, morphological, and structural properties, that meet the needs of specific applications. The desired properties are determined by the structure of the resulting film, which is highly dependent on the deposition method, film material, and substrate. Generally, thin films can be produced based on two technological groups:

- physical deposition methods
- chemical deposition methods

The most commonly used thin-layer deposition techniques resulting from these two groups of categories in the following diagram (*Figure II.2*):

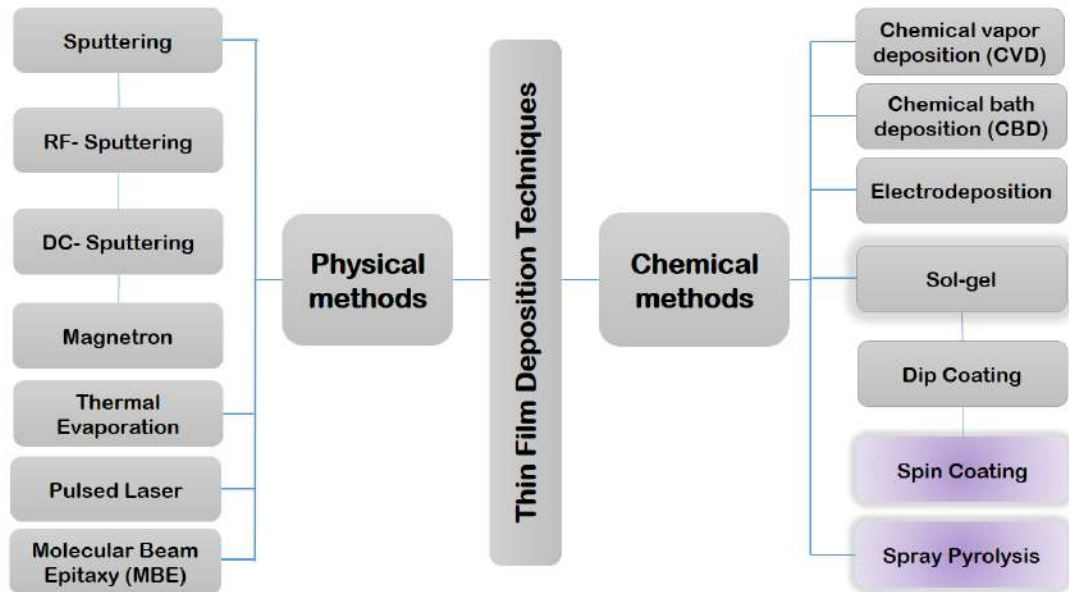


Figure II.2 Diagram of thin-film deposition techniques.

As we can see from the diagram represented in **Figure II.2**; the thin layers used in this study were produced and deposited using spray pyrolysis/sol-gel chemical methods. Therefore, spray pyrolysis and sol-gel (spin coating) processes will be reviewed in this section.

Notably, regardless of the method used to prepare the thin film, the film was always embedded in the support on which it was constructed. Thus, a thin layer of the same material of the same thickness can have substantially varied physical characteristics depending on whether it is formed on a monocrystalline silicon substrate or an amorphous insulating substrate like glass [36].

II.3.1 Spray Pyrolysis Technique (SPT)

SPT is a common process. It consists of Spray and Pyrolysis " Spray " is the English name, which means spraying liquid (perfume, deodorant, insecticide, etc.). "Pyrolysis" means heating the substrate [36]. Spray pyrolysis has been considered in research to produce thin or thick layers and ceramic coatings. In contrast to several other thin-layer deposition methods, SPT is an extremely simple, cost-effective, easy-to-deposit film of various compositions, and no high-quality substrate is required. Spray pyrolysis has been easily used for the fabrication of dense or porous layers and mono-or multilayer films [53].

Typically, the SPT is composed of an atomizer, a precursor solution, a heating substrate above a heating plate (required to trigger the chemical interaction between the compounds), and a temperature regulator. The deposition of thin layers by this chemical method occurs by spraying a metal salt solution onto the preheated substrate (*Figure II.3*). Droplets that reach the substrate break down on the surface and chemically react to form deposits.

In typical, the systems utilized to create a spray fall into two groups [36].

- The pneumatic spray method sprays liquid into fine droplets under the action of gas pressure.
- Ultrasonic spray method, atomization of the solution generated by ultrasonic waves. In this case, the droplet size is very small and uniform (homogeneous).

II.3.1.1 Principle of the spray pyrolysis technique

Using an ordinary pneumatic system or an atomizer with an ultrasound generator, fine droplets of a solution containing various parts of the substance to be deposited were sprayed. These systems can transform solutions into jets of very fine droplets with tens of microns (μm) diameters. The jet reached the surface of a hot substrate at a temperature sufficient to decompose the product dissolved in the solution and activate a reaction capable of producing the desired material. At these temperatures, some reaction products can be removed immediately; therefore, only the compounds remain on the substrate. Film formation by spray pyrolysis can be described as follows:

- At the exit of the nozzle, the formation of droplets with a certain average size.
- Decomposition of the precursor solution on the substrate surface.

The changes in the droplets after their formation can be summarized as follows: changes in temperature, speed, size, and composition caused by evaporation [36].

II.3.1.2 Spray pyrolysis process

The deposition of thin films by spray pyrolysis (*Figure II.3*) can be performed in three steps.

- **1st stage:** atomization of the precursor solution.

- **2nd stage:** transport of the generated aerosol.
- **3rd stage:** decomposition of the precursor on the substrate.

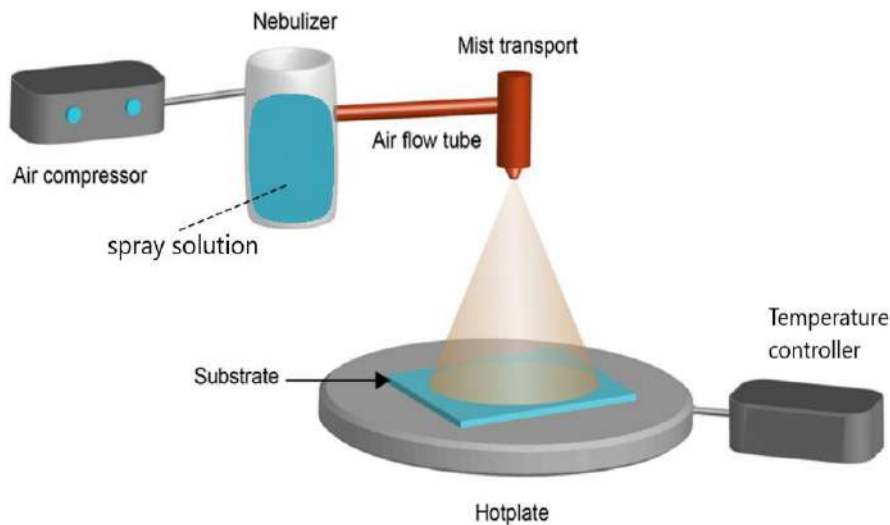


Figure II.3: Schematic diagram of spray pyrolysis equipment.

a. Atomization of the precursor solution

This is the 1st step in the pyrolysis spray process. The aim was to create droplets from a precursor solution and launch them toward the hot substrate surface with a certain initial speed (spray flow). Typically, air-blast or ultrasonic methods are used in this step of the spray process [53].

b. Transport of the aerosol generated (Sprayed solution)

After the created droplet (in aerosol form) leaves the atomizer, it moves toward a substrate at a starting velocity set by the atomizer in an effort to obtain as many droplets as possible to the surface. As the aerosol is transported, it undergoes physical and chemical changes, as shown in *Figure II.3* [53].

c. Decomposition of precursor

The final step of the spray process. When a droplet hits the substrate surface, many mechanisms can occur simultaneously: remaining solvent evaporation, droplet spreading, and salt decomposition. Diverse models exist for the precursor solution decomposition. The

temperature of the substrate depends on the temperature. *Viguie and Spitz* proposed the following processes (*Figure II.4*) [90].

Process A: At lower substrate temperatures, the direct projection of liquid droplets onto the substrate evaporates and leaves a dry precipitate in which decomposition occurs.

Process B: At higher temperatures, the solvent evaporated completely during transport and before the droplets reached the substrate surface. Subsequently, the dried precipitate hit the substrate and decomposed.

Process C: At even higher temperatures, the solvent evaporates as the droplets approach the substrate. At this moment, the precipitate formed after decomposition dissipates and sublimates (goes directly from the solid to the gaseous state). The vapor then diffuses into the substrate and can cause a heterogeneous reaction.

Process D: At the highest temperatures, the precursor (metal compound) evaporates before reaching the substrate, so that solid particles form after the chemical reaction in the gas phase.

Figure II.4 represents a schematic of the four processes that can occur during droplet breakdown [36,53].

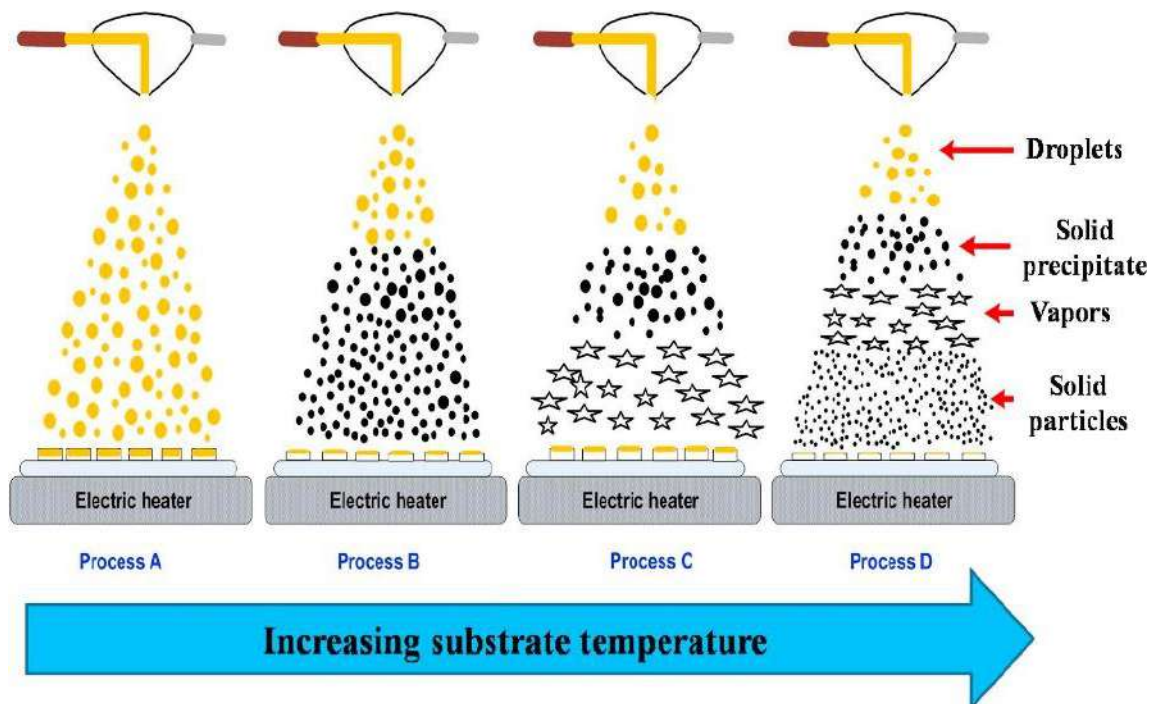


Figure II.4: Description of films deposited by Spray pyrolysis method [91].

II.3.1.3 Spray pyrolysis parameters

Before each elaboration of the thin films. The choice of the precursor (salts or organometallic source material) is required. The precursor type influences 3 parameters: temperature (which should be enough to cause the source sol to break down), concentration (which limits the maximal concentration in the solution), and type of solvent (which limits the options for salts because some solvents may not dissolve them). Thus, the ideal spray settings typically vary significantly depending on the precursor type. The main spray parameters are as follows [53]:

- Substrate temperature (to achieve high adhesion layers).
- Solution flow rate.
- Type of source salt (nitrate, acetate, chloride, etc.)
- Solvent.
- Deposition period.
- Spray nozzle diameter.
- Nozzle-substrate distance.

II.3.1.4 The advantages of the SPT

STP is a relatively easy technique with several advantages.

- Speed and simplicity of film preparation.
- Several products can be used simultaneously, particularly as stimulants.
- The layer prepared using this technique was of good quality. No annealing temperature was required after deposition, and the films were neither amorphous nor of poor quality.
- This is a cheap and economical technology. It can be industrialized [36].

II.3.2 Sol-Gel Technique

The sol-gel process is a so-called gentle chemistry method. The name sol-gel is a contraction of the term "solution-gelation", and it is among the chemical techniques used for the preparation of thin-film deposits of transparent and conductive oxides. This method is implemented under mild chemical conditions with temperatures significantly lower than those required for other conventional synthesis techniques. These conditions usually allow the association and coupling of new families of organo-mineral hybrid molecules to be formed by organic and mineral

species possessing new properties. This process can be used in various fields such as encapsulation and the development of hyper-porous materials, but its main application is in the production of thin film deposition [36]. It is one of the simplest and purest techniques for fabricating thin films on metal or glass substrates. The formation of a thin film by sol-gel involves three steps: (a) preparation of a precursor solution, (b) deposition of sol on the substrate using the appropriate method and (c) heat treatment of the deposited film. The sol-gel technique involves two methods for depositing the sol onto a substrate:

- ✚ **Spin coating:** This technique uses centrifugal and adhesive forces to create a homogeneous coating by placing the sol on a horizontal disk that rotates evenly. The rotational velocity, material viscosity and concentration affect the film thickness.
- ✚ **Dip coating:** This entails the quick drying of the substrate after it has been submerged in the prepared sol. A consistent and high-quality film can be produced by maximizing the number of cycles, soaking time and drying time [44].

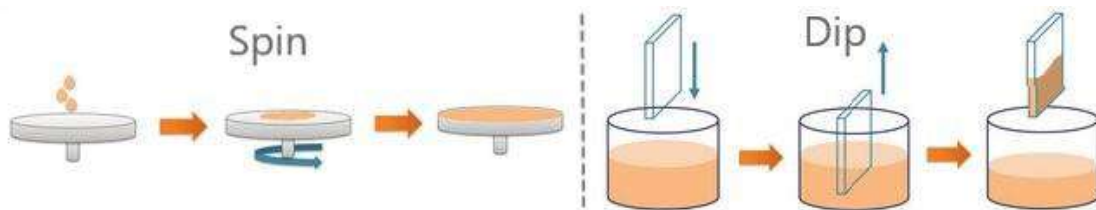


Figure II.5: The two sol-gel techniques for depositing the sol onto a substrate [92].

II.3.2.1 Sol-Gel principle

This technique involves the production of a solid material from a liquid solution, through chemical reactions at a temperature close to ambient temperature (20–150°C). These mechanisms are based on the transformation of a stable liquid solution (Sol) into a solid material (a dry gel called a xerogel) via an inorganic polymerization process. The time it takes for "sol" to turn into "gel" is called freezing time (or freezing point) [36]. Depending on the nature of the precursors used. We distinguish between two synthesis methods type:

The inorganic approach involves dissolving metal salts in an aqueous solution, such as nitrates, sulfates, chlorides, or acetates.

Metal alkoxides in organic solutions are the most commonly utilized precursors in the organometallic approach [43].

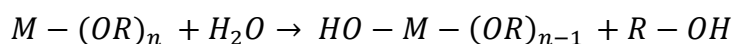
In both cases, the reaction is initiated by hydrolysis (addition of water to the alkoxides pathway and modification of the pH of the inorganic pathway to form hydroxides) to form gels composed of molecules called hydrogels, whose chemical nature corresponds to an aqueous oxide: MOX, nH_2O [36].

II.3.2.2 Sol-Gel process

In the sol-gel method, the chemical mechanism usually decomposes in two stages: hydrolysis and condensation. Each gel obtained was linked to the appropriate materials.

Hydrolysis

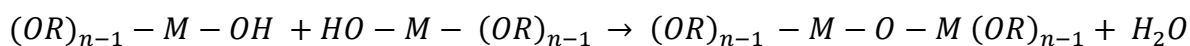
The hydrolysis of substances is the decomposition of water due to H^+ and OH ions coming from the dissolution of water. Therefore, substitution of the $-OH$ ligand by the $-OR$ ligand occurs. This interaction is accompanied by the consumption of water and the release of alcohol, namely, the hydroxyl group ($R-OH$), as shown in the following chemical reaction:



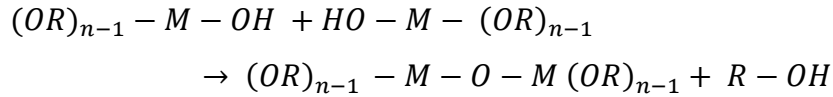
The goal was to generate reactive $M-OH$ functions. This involves the conversion of alkoxides functional groups to hydroxyl functional groups. The obtained solution is called a sol [36].

Condensation

The groups ($HO-M (OR)_{n-1}$) generated during hydrolysis react with each other to give a water molecule (reaction below).



Either with a molecule of the alkoxide $M (-OR)$ giving an alcohol molecule (as follows reaction at room temperature.):



The leads to the creation of bridges M–O–M, or each O atom forms a bridge between 2 metal atoms, corresponding to the gradual creation of a gel with increasing viscosity. Solvents and unreacted precursors may be present in this gel [36].

Because the hydrolysis and condensation reactions have similar procedures, the factors affecting the hydrolysis also affect the condensation reaction mechanism and kinetics, and as a result, the properties of the gel that is produced [43]. These reactions gradually lead to the formation of (M-O)_n polymer chains (polycondensation) and eventually stabilize. The sol can then be deposited on a substrate to form a thin film using deposition techniques, such as dip coating or spin coating. The progressive evaporation of the solvent present in the deposited film increased the concentration of the reactive species, thereby activating hydrolysis-condensation reactions. The inorganic polymerization then continues until a three-dimensional oxide network is formed, called a “gel” or, if all the solvent has evaporated, a “xerogel”. This sol → gel → xerogel transformation generally lasts only a few seconds. Finally, heat treatment can be carried out to evaporate or decompose the organic residues and to condense the last hydroxyl groups to obtain a dense film of pure oxide [93].

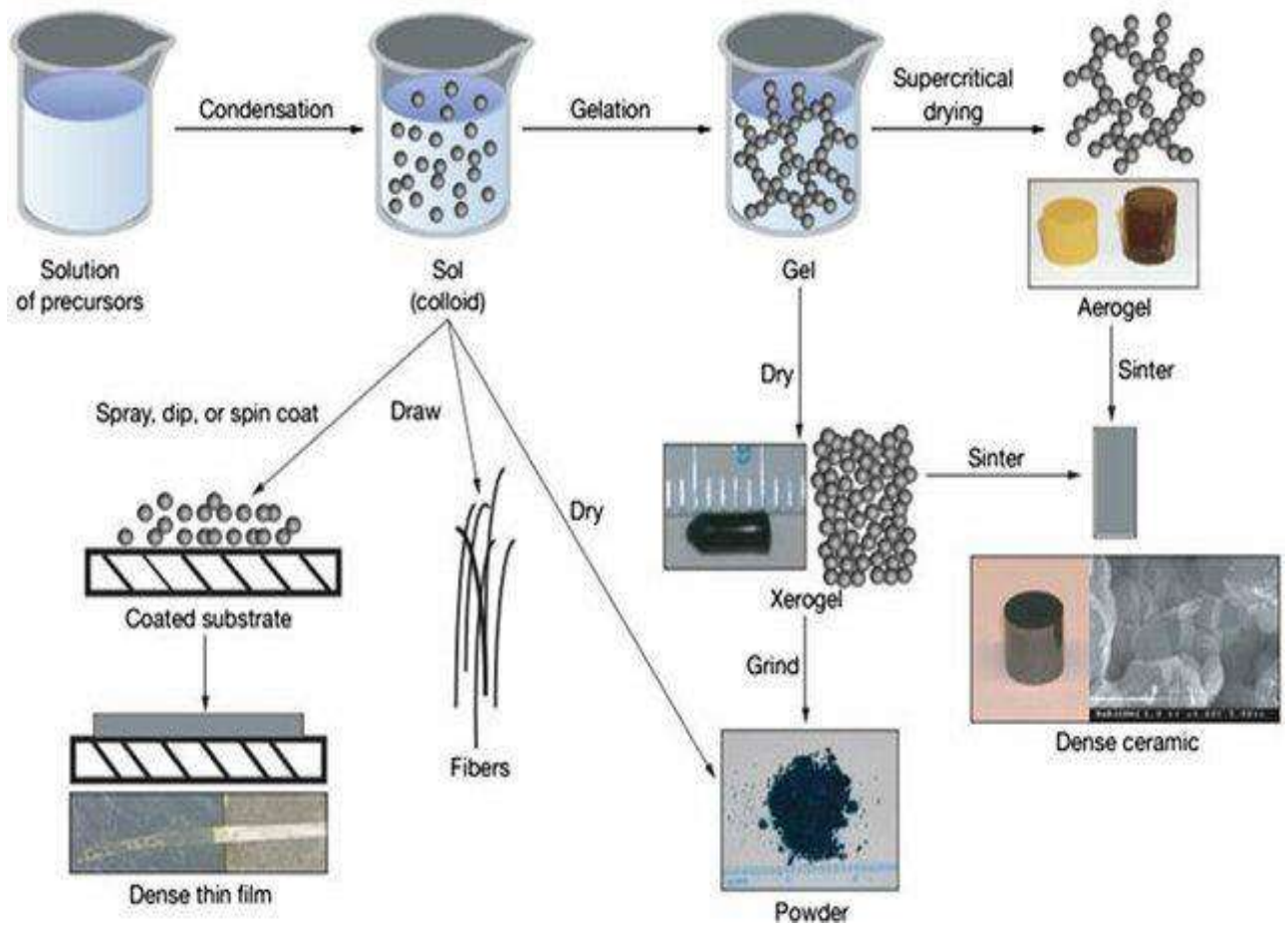


Figure II.6: The schematic diagram of sol-gel method [94].

In the remainder of this chapter, we present in detail the sol-gel technique used, which is the spin-coating technique, because of its importance in our current research.

II.3.2.3 Spin-Coating

It is one of the sol-gel methods for coating thin layers. The material to be formed into a layer will be a coating solution that will be applied to the substrate surface after being first dissolved in an appropriate solvent. Subsequently, the substrate was rapidly rotated to create a thin homogeneous layer [44]. Spin coating is an inexpensive, quick, and easy-to-use method. One of the advantages of spin coating is that it produces uniform and continuous films. The deposited film had a high optical quality and purity. Nevertheless, it needs flat substrates since big substrates are hard to spin quickly enough to produce a thin layer, and the spin coating does not function with uneven substrates [44].

II.3.2.4 The process of the Spin-coating technique

Figure II.7 demonstrates the spin-coating procedure. This simple approach usually consists of 4 steps.

1. **Centrifugation:** a high speed (thousands of rotations per minute) was applied to the substrate.
2. **Deposition:** this process involves depositing a residual solution made up of inorganic or organic components on the substrate's surface.
3. **In the spinning stage:** centrifugal forces encourage the drop sol radial diffusion at fast rotation, helping a thin layer form on the substrate.
4. **Evaporation:** is the drying process that creates a thin layer by evaporating the solvent for a few minutes at a certain temperature [44].

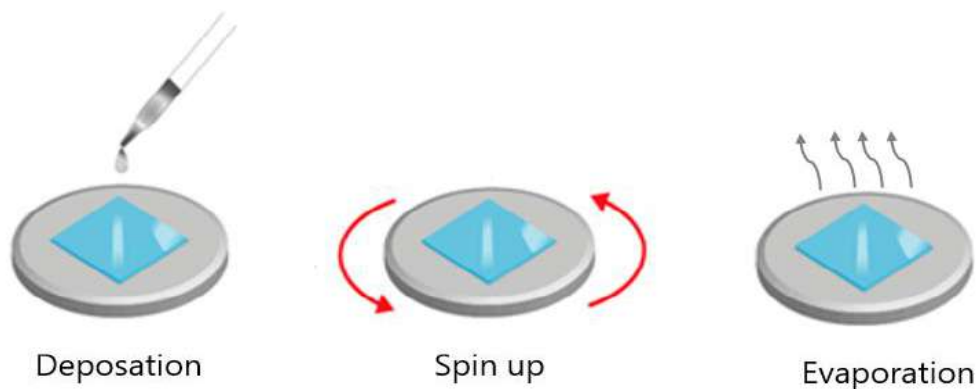


Figure II.7: Schematic of spin coating process.

II.4 Characterization tools

When manufacturing or using fabricated thin-film materials and devices, it is important to illustrate the different properties or characteristics of the synthesized films and novel materials according to the characterization process. The latter includes the crystalline structure, morphological surface, compositional, optical, electrical, etc. This section describes the various analytical tools used to characterize the deposited thin films in this study. We will see through a few theoretical surveys the main information they can provide for the characterization of our layers.

II.4.1 X-Ray Diffraction

Structural analysis plays an important role in determining the growth-correlated properties of semiconductor structures. X-ray diffraction is used to determine several structural parameters, such as identical phases (qualitatively), lattice structure parameters, preferred orientation, crystallite sizes, lattice strain, and dislocation. It is a non-destructive method used for crystal phase identification of materials based on their diffraction patterns. X-ray diffraction needs no specific sample preparation methods, which makes it easier to understand the structural properties of elaborated materials. A diffraction spectrum was obtained when the samples were irradiated with a collimated X-ray beam with a wavelength close to the crystal lattice spacing (λ), as illustrated in **Figure II.8 (a)**. The X-ray peak pattern produced by this method provides a structural fingerprint of the material (unknown) [95].

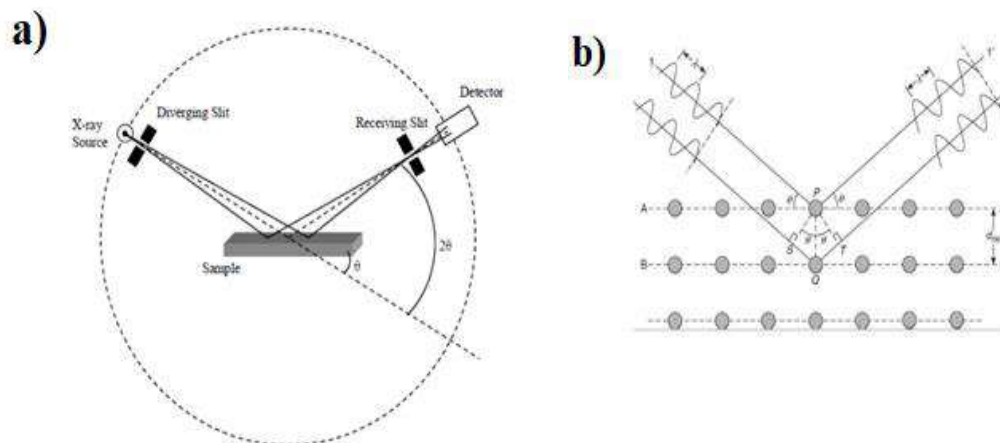


Figure II.8: a) Schematic diagram of X-ray diffractometer [66]. b) X-ray beam interacting with a sample [95].

The cathode ray tube generates X-rays and monochromatic radiation that is filtered, collimated, and directed over the sample. X-rays can be considered as electromagnetic wave radiation, whereas crystals can be considered as a regular arrangement of atoms. X-ray beams are first scattered by the electrons of an atom. X-ray When an electron is struck, secondary spherical waves emerge from it [66].

The incoming diffracted X-rays were recorded with a detector as a function of the diffraction angle 2θ and the orientation of the specimen. In most directions, X-ray waves cancel out one another owing to destructive interference; however, in a few specific directions, constructive waves were added according to Bragg's law:

$$2d \sin \theta = n\lambda \quad (\text{II. 1})$$

Where

- θ : Angle incidence.
- λ : incident beam wavelength.
- d : Interplanar distance.
- n : diffraction order.

This is the basis of Bragg's law; which connects (d) the interplanar distance of atoms from which diffraction occurs to (θ) the angle at which the incident beam must probe the plane to produce constructive interference (**Figure II.8. (b)**). The crystalline phase structure of the films synthesized in this work was defined using Cu radiation $\lambda_{K\alpha} = 1.54 \text{ \AA}$ of X-Ray diffractometer using a PANalytical Empyrean diffractometer (**Figure II.9**).



Figure II.9: X-ray-Diffractometer in the CRAPC Laghouat.

II.4.1.1 Structural parameters

After structural phase identification by X-ray diffraction, we can introduce the main structural parameters as follows:

TC_{hkl} "**texture coefficient**" is an important parameter in the XRD study used to determine the preferential growth orientation of the grains in the deposited layers, which may give an idea about the probability of nanocrystallite formation, which should be calculated for every plane from the diffraction data using Eq.2 **II. 2** [96]:

$$TC_{hkl} = \frac{I(hkl)}{I_0(hkl)} \left[N^{-1} \sum_{i=1}^n \frac{I(hkl)}{I_0(hkl)} \right]^{-1} \quad (\text{II. 2})$$

where $I(hkl)$ is the intensity of the measured (hkl) peak, $I_0(hkl)$ is the standard peak intensity reported in the JCPDS cards for each phase, n is the diffraction number of the peaks, and N is the number of reflections in the XRD pattern. When $TC_{hkl} = 1$, the sample was a randomly oriented crystallite. In contrast, $TC > 1$ was more abundant along the crystallites oriented at this plane.

The lattice constants "a, c"; for the hexagonal structure and "a" for the cubic structure can be calculated using Eq. II.3 [17] and Eq. II.4 [97].

$$\text{For hexagonal:} \quad \frac{1}{d_{hkl}} = \frac{4}{3} \left(\frac{h^2 + hk + k^2}{a^2} \right) + \frac{l^2}{c^2} \quad (\text{II. 3})$$

$$\text{For cubic:} \quad \frac{1}{d_{hkl}} = \frac{h^2 + k^2 + l^2}{a^2} \quad (\text{II. 4})$$

Where d_{hkl} value can be calculated by Bragg's Law: $2d_{hkl}\sin\theta = n\lambda$ [98] (λ : $K\alpha_{Cu} = 0.154$ nm, θ : $\frac{1}{2}$ Bragg angle).

The **crystallite size** (D_{cs}) of the samples can be estimated by using Scherer's formula Eq. II.5 [17]:

$$D_{cs} = \frac{0.9\lambda_{Cu}}{\beta \cos\theta} \quad (\text{II. 5})$$

Where β is FWHM (full width at half maximum: The width of a spectrum is measured at half of the height of a spectral peak) and $\lambda_{Cu} = 1.54$ Å.

D_{cs} used to evaluate the dislocation lines' lengths per volume unit (**dislocation density**) [97] using Eq. II.6.

$$\delta = \frac{1}{D_{cs}^2} \quad (\text{II. 6})$$

The **micro-strain** (ϵ_{ms}) is an interesting value for deposited films that develop from structural defects. It can induce the diffraction peaks broadening that is associated with FWHM (β) and can be determined as follows [99]:

$$\epsilon_{ms} = \frac{\beta}{4\tan\theta} \quad (\text{II. 7})$$

When D_{cs} decreases, compression occurs because of the inside surface tension-induced lattice strain, and the number of crystal borders increases along the layer surface area. Therefore, the lattice strain weakens when the crystallite size increases due to a lower compression via the grain edges, and the dislocation lines decrease due to the low number of grain boundaries, which means that the grain boundary is a trap of dislocations [28,97].

II.4.2 Fourier-transform infrared spectroscopy

The word "infrared" (IR) refers to electromagnetic radiation with wavelengths between one micron and one millimeter. FTIR is one of the analytical methods for forecasting chemical identification. It offers useful details on the molecule's structure [66].

As long as the chemical bonds in the sample are IR-active, that is, they have a dipole moment that allows them to absorb electromagnetic radiation; the absorption spectrum serves as "an image" of the chemical bonds that exist in the sample. The analytical method known as Fourier Transform-Infrared (FTIR) Spectroscopy is used to distinguish between organic and, in certain situations, inorganic materials [95].

The method is based on the well-known selective IR absorption of a chemical substance, as illustrated in *Figure II.10 (a)*, which depicts a block schematic of a conventional spectrophotometer's parts [66]. Both monochromatic and broad-spectrum IR sources can be used in IR absorption spectroscopy. A beam splitter splits the incident light split into two light beams. Then reflected by a fixed and moveable mirror before reaching the sample. The two light beams that have been reflected join again and experience interference, as illustrated in *Figure II.10 (a)*. The analyzed materials are illuminated by recombined light, which also allows for the detection of transmitted or deflected light. The gathered signal may be used to determine the transmittance spectrum, and a Fourier transform is applied to the interferogram. Utilizing the software included in the FTIR instrument, the transmittance spectrum can also be transformed into the absorption spectrum [95].

After absorbing IR radiation, the molecules of a chemical substance move in a variety of vibrational modes, giving birth to tightly packed absorption bands known as IR absorption spectra. In the IR spectrum, band intensities can be expressed as either transmittance (T) or absorption (A). The distinctive functional groups and bonds present in a chemical compound provide a fingerprint for its identification, and different bands in the IR spectrum arise

corresponding to these groups and bonds. When an atom or a group of atoms constituting a molecule vibrates at a fundamental frequency equal to the frequency of the incident radiation, the molecule absorbs the radiation. Understanding the relationship between a material's structure and its electromagnetic response is helpful in determining its characteristics. The transmission bands in the fingerprint area below 1000 cm^{-1} are often produced by the bands in the range $300\text{--}700\text{ cm}^{-1}$, which correspond to the fundamental vibration of the ions of the crystal lattice [66].

FTIR analysis in this study was performed using a Cary660 FTIR spectrometer to record the attenuated total reflectance (ATR-FTIR) spectra (**Figure II.10 (b)**).

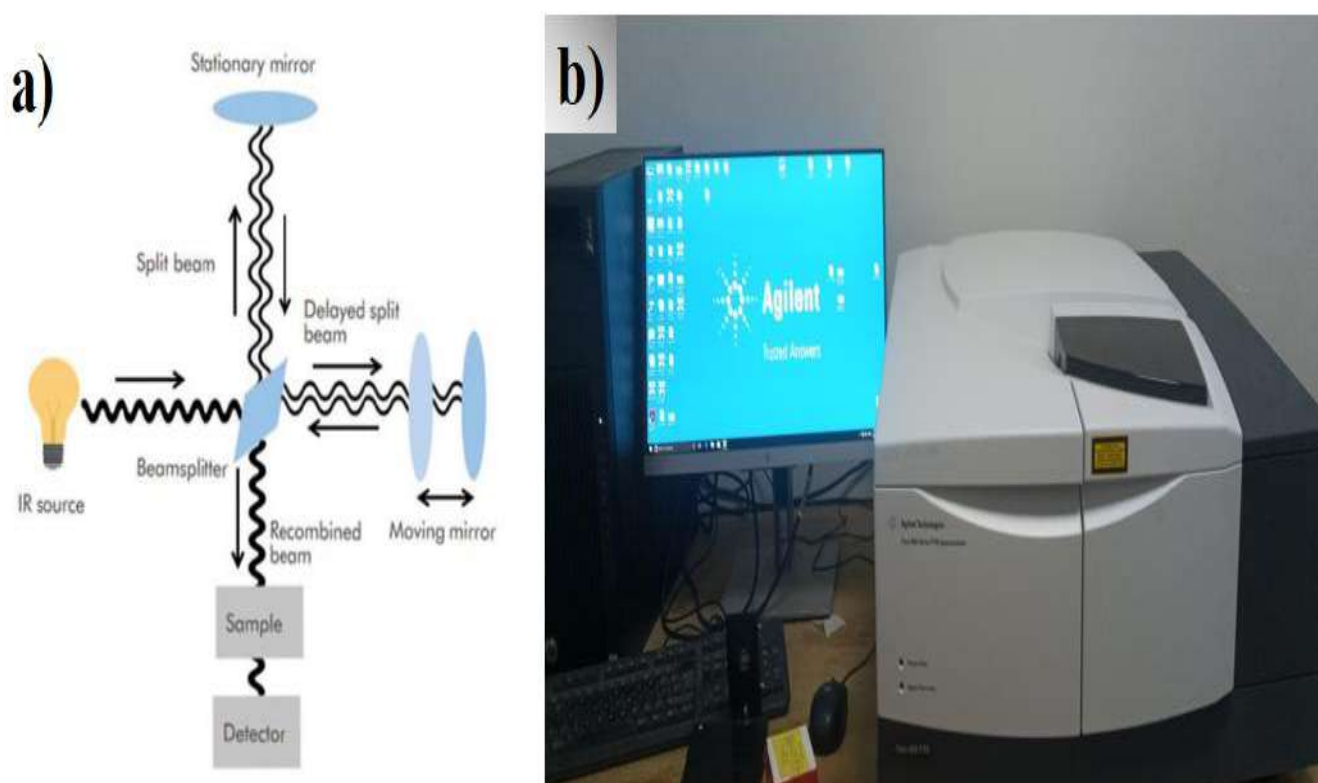


Figure II.10: *a) Schematic diagram of FTIR Spectrophotometer [95]. b) Cary 660 FTIR spectrometer equipment.*

II.4.3 Surface morphology

II.4.3.1 scanning electron microscopy (SEM)

SEM is a technique used for high-resolution imaging of surfaces and is a fundamental instrument in many scientific disciplines. by concentrating the electron beam on a specific area of the material [95]. A schematic of the scanning electron microscope is shown in *Figure II.11 (a)*.

SEM is a potent microscope that creates a picture of items like broken metal pieces, foreign particles and residues, thin-film electronic components, biological samples, and countless others using electrons as opposed to light. Compared to traditional light microscopy's maximum magnification of approximately 2,000 ×, the lower wavelength of electrons allows for picture magnifications of up to 100,000 ×. A tungsten filament cathode-equipped electron gun emits a thermionic electron beam in a conventional SEM. By utilizing one or two condenser lenses, the electron beam, whose energy ranges from a few hundred electron volts to 40 KeV, is focused on a point with a diameter between 0.4 and 5 nm. The last lens commonly deviates the beam in the x- and y-axes so that it scans in the raster mode over a rectangular section of the sample. The atomic number, density, and rate of energy decrease all affect the interaction volume. The exchange of energy between the sample and the electron beam results in electromagnetic emission, secondary electron emission, and inelastic scattering of high-energy electrons, all of which may be checked using specific detectors [66]. There must have been some conductivity in the sample. Thus, non-conducting samples may require electrical contact by coating with a very thin layer (~ 2–5 nm) of a conductive material, such as iridium or a gold-palladium alloy. In addition, materials that are exposed to an electron beam must be completely free of dirt and fingerprints [95].

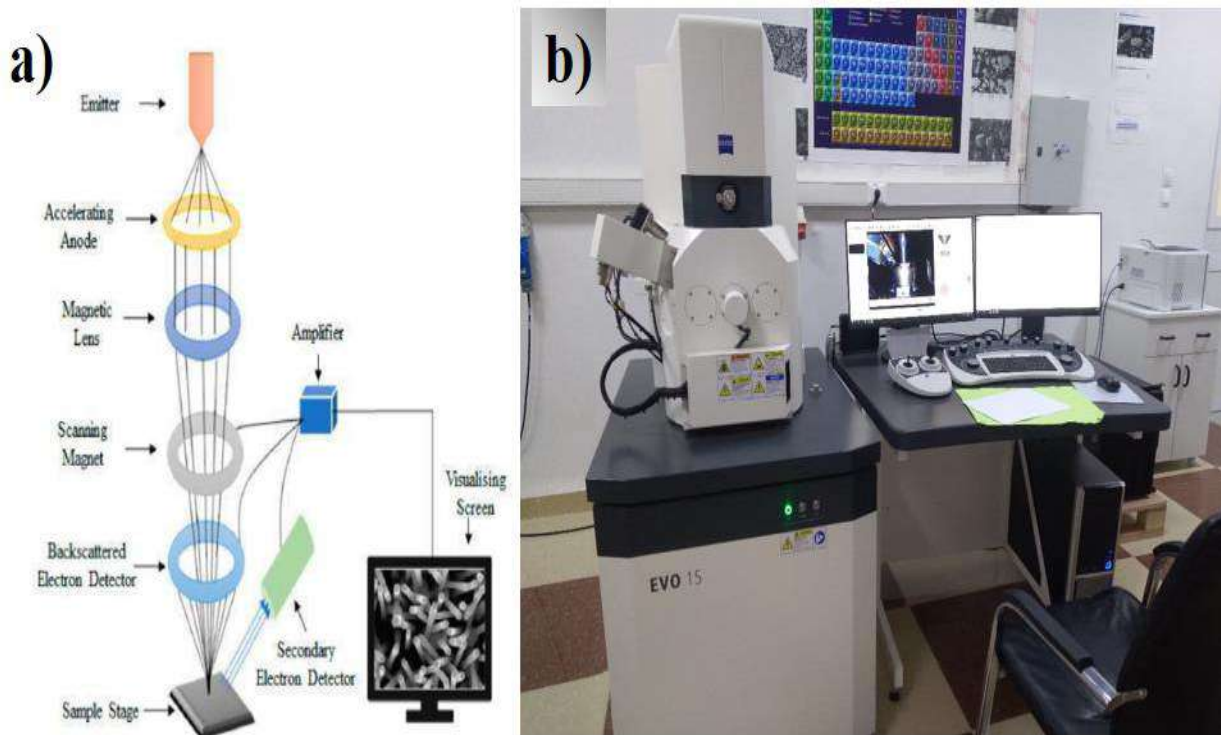


Figure II.11: a) Schematic diagram of SEM [40]. b) The ZEISS EVO 15 SEM equipment.

For this work, SEM ZEISS EVO 15, equipped with energy-dispersive X-ray spectroscopy (EDS) (**Figure II.11 (b)**), did the SEM images of the obtained thin films, The EDS technique is described as follows.

II.4.3.2 Energy Dispersive Spectroscopy

In order to analyze samples, energy-dispersive spectroscopy (EDX or EDS) is frequently employed in conjunction with SEM technology. It is an analytical method used to determine the elements of a sample. Its characterization skills are largely attributable to the fundamental idea that every element has a different atomic structure, which makes it possible to distinguish one element's characteristic X-rays from another in a distinctive manner. When the electrons from the electron beam hit the electrons of the inner orbital of the atom of the specimen, they produce distinctive X-rays. The impact force drives the electron out of the atom's orbitals and into the "free" state. To correct this, the ionized atom adjusts, and electrons from higher orbitals start to move to lower orbitals, releasing energy in various forms, including X-rays. The energy difference between the two levels is equivalent to the energy of the released X-ray photons. The solid-state detector subsequently converts the X-ray energy emitted by the electron into signals, which are then processed into an X-ray energy spectrum. Therefore, the identification of the

atom from which the X-ray was generated may be determined by measuring the energies present in the X-rays released by a specimen during electron beam bombardment. The concentrations of various elements in the material were determined using the characteristic X-rays from each element. Because each of these peaks is specific to each atom, they represent a separate element. The concentration of an element in a specimen is indicated by its peak height in the spectrum. There are a few points to consider when using EDS. EDS is a volume analysis rather than a surface analysis. This is significant when analyzing thin films, as the depth is often wider than the thickness of the deposited layer. This implies that components of the substrate are observed and must be accounted for. In addition, it is important to carefully assess the peaks produced by the EDS [95].

II.4.3.3 Atomic Force Microscope

Characterization by Atomic Force Microscopy (AFM) is a non-destructive method for analyzing the topography of a given sample. From there, we can obtain additional information to the SEM, such as the morphology of the surface through a 3D view and the roughness of the surface analyzed [50]. Contact between the surface of the material to be studied and a nanometric probe is the foundation of the AFM principle, as shown in *Figure II.12 (a)*. The mode of operation of the atomic force microscope is essentially based on scanning or rubbing the surface of the sample with a tip fixed on the arm of a flexible lever. The tip-lever system can be moved in the X, Y and Z directions. A laser diode was used to measure the deflection of the lever. The laser beam emerging from the diode is focused on the end of the lever. Then, the latter reflected toward the photodetector. As a result, the deflection of the lever causes movement of the reflected beam [50].

The tip of the probe was fixed under a flexible or cantilever microlever with a predetermined rigidity. The tip creates a three-dimensional picture of the substance under analysis by scanning the surface and following the topography of the sample.

Historically, the contact mode was the first operating mode created for AFM. The lever arm's tip, which is connected to the end, sweeps the surface while staying in constant contact with it. The fundamental disadvantage of this method is its significant frictional force. The tip or observed sample may be damaged as a result of these pressures [95].

The non-contact mode is used when the tip produces an attractive force with the sample, rather than contacting it.

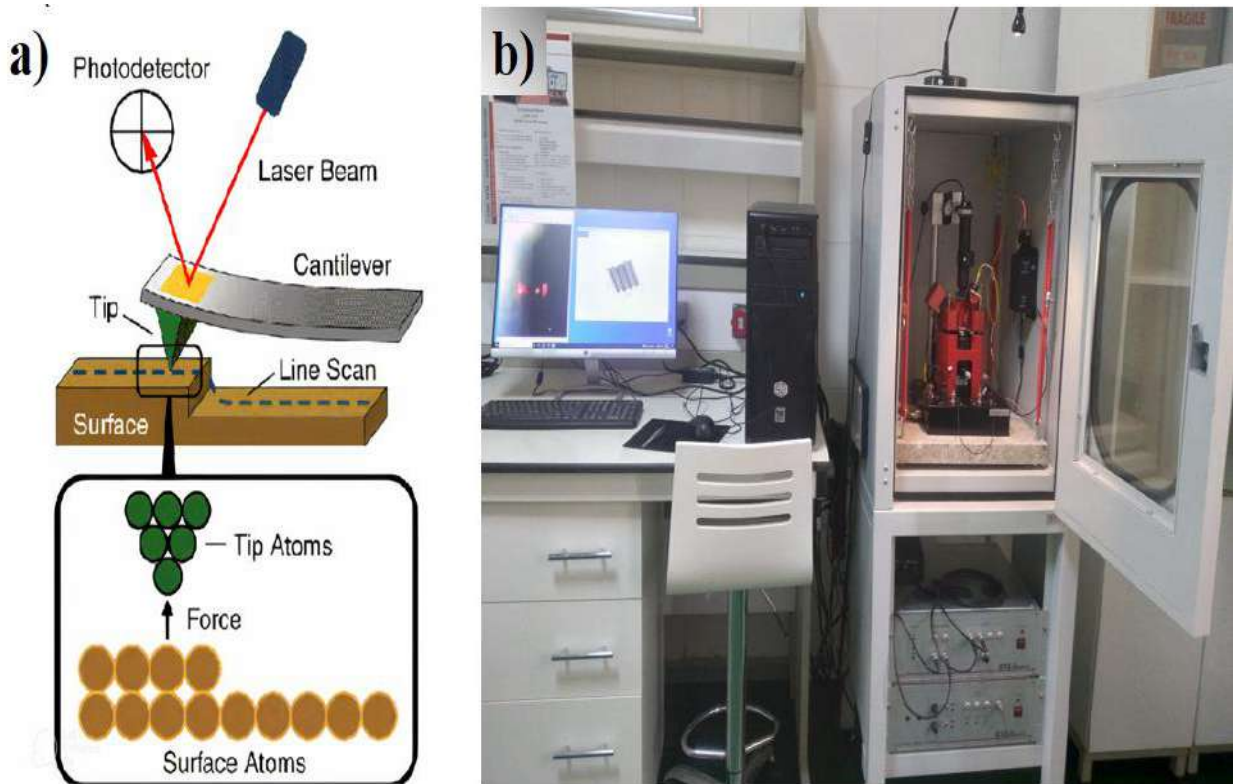


Figure II.12: a) Schematic diagram of AFM [95]. b) APE Research A100 AFM equipment.

It is feasible to assess the roughness of the sample from the topological image.

- ✚ RMS roughness, in roots. Rms or Rq: Root mean square of height deviations over the evaluation length and measured with respect to the mean line [95]:

$$Rq = \sqrt{\frac{\sum_{i=1}^N (Z_i - \hat{Z})^2}{N}} \quad (II. 8)$$

Where:

- Z_i : The height value for the scan surface at point i .
- \hat{Z} : The arithmetic average height in the scanned region. ($\hat{Z} = \frac{\sum_{i=1}^N (Z_i)}{N}$)
- N : total number of points in the scanned region.

In this thesis, the surface topography images and roughness values of the deposited films were determined by use an atomic force microscopy (APE Research A100 AFM; **Figure II.12 (b)**).

II.4.4 Optical Characterization

II.4.4.1 UV-Vis Spectrophotometer

UV-visible spectroscopy is a non-destructive optical analysis technique that enables the measurement of the optical transmittance of a material and the determination of the bandgap energy (E_g) of the film. It involves photons with wavelengths in the ultraviolet (100 nm-400 nm), visible (400 nm-750 nm), and near-infrared (750 nm-1400 nm) ranges, which is based on the transition of electrons, atoms, or molecules from the ground state to the excited state via the excitation of electromagnetic waves. The spectrophotometer consists of a source consisting of two lamps that provide an emission continuum over the entire UV-visible wavelength range.

- A deuterium lamp (D) emits wavelengths of 180–400 nm (ultraviolet).
- A tungsten lamp (W) that allows waves from 400 to 800 nm (visible) was selected.

The monochromator can select the wavelength by moving it to scan the spectral range. The photon beam of the selected wavelength passes through a mirror that moves synchronously with the monochromator, and the beam passes through the sample and reference. Finally, the amplifier compares the output intensity to the emission intensity. As shown in *Figure II.13 (a)*.

The experimental measurements in this work were carried out by a UV–Vis spectrophotometer (Cary 100 UV–Vis; *Figure II.13 (b)*) [36].

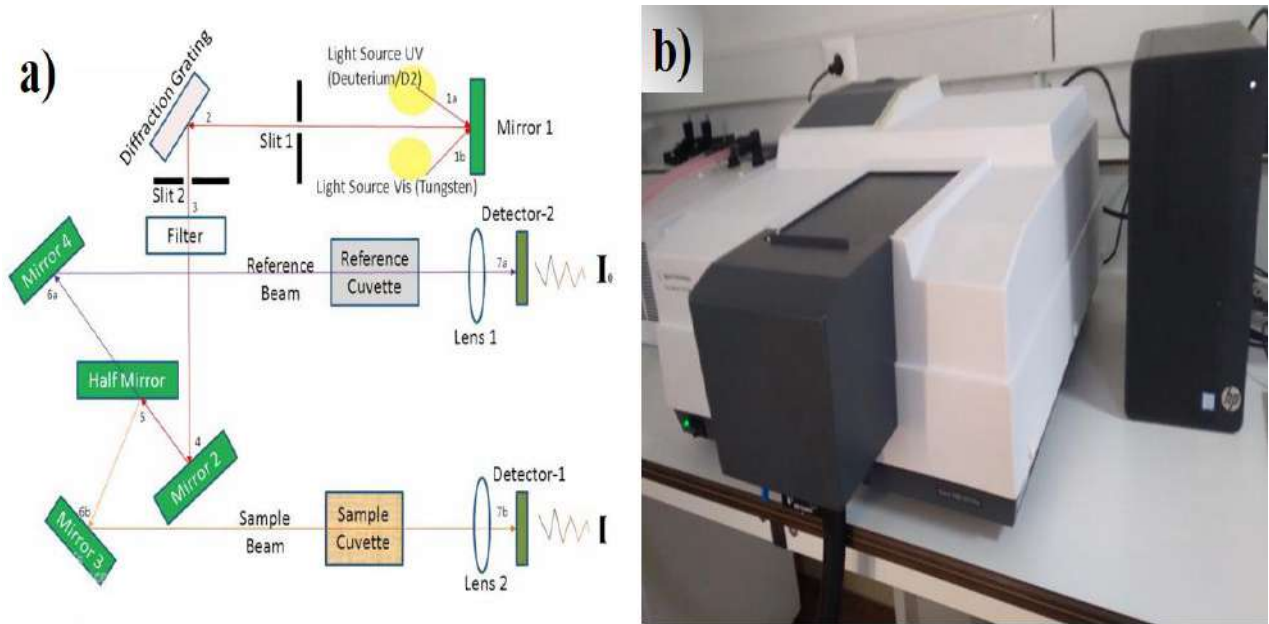


Figure II.13. a) Schematic diagram of UV-Vis spectrophotometer [95]. b) Cary 100 UV-Vis equipment.

II.4.4.2 Optical constants

II.4.4.2.1 Absorption coefficient

The electronic transitions between the CB and VB in the materials begin at the absorption edge because it corresponds to the least energy variation between the highest maximum of the VB and the lowest minimum of the CB. The optical absorption of the materials and their coefficient of absorption, α , are directly related. Determining the absorption properties of glasses and deposited thin layers is essential, particularly when it comes to the optical material properties that are being explored for potential applications. Some of the energy of light that strikes thin films is reflected, some is absorbed, and the remainder is transmitted [66].

The optical absorption coefficient in thin films is a function of their structural properties, and it varies according to the layer thickness and wavelength. The Beer-Lambert law was used to obtain the absorption coefficient values from the Absorbance or Transmittance spectra [100] :

$$\alpha = 2.303 \frac{Abs}{th(cm)} \quad (II. 9)$$

Abs: is the absorbance, th: thickness of the deposited film.

To learn more about the optical gap energy, the absorption coefficient is used.

II.4.4.2 Determination of the bandgap width

Several methods can be used to determine the energy gap of a semiconductor, depending on whether it is in the form of a thin film. The absorption spectrum of a sample is usually recorded in transmission mode. The optical gap was determined by applying the Tauc model in the high-absorption region [101]:

$$(\alpha h\nu)^2 = C(h\nu - E_g) \quad (II. 10)$$

Where A constant, $h\nu$ is the photon energy (in eV), and the value of n depends on the type of transition between the valence and conduction bands. The values of n allowed were 2 for a direct transition allowed (such as ZnO) and 1/2 for an indirect transition allowed (such as CuO). By extrapolating the curve to the energy axis, the optical gap can be derived from the square curve of the product of the absorption coefficient and the photon energy ($h\nu$) as a function of the photon energy. We extend the linear part of α^2 up to the x-axis (i.e. $\alpha^2 = 0$), and we obtain the value of E_g (*Figure II.14*)

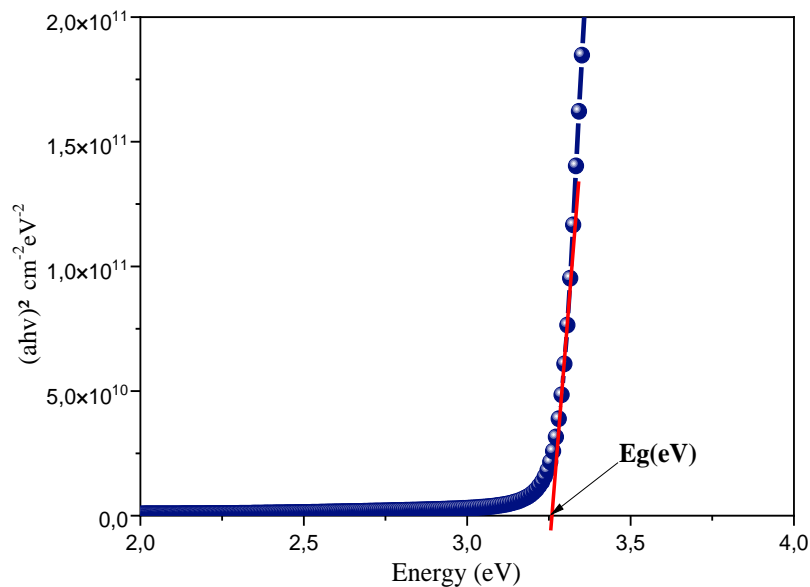


Figure II.14: Estimated of E_g of the thin film using the Tauc method.

II.4.4.2.3 Urbach Energy

Typically, in absorption near the band edges, an electron via the highest point of the VB is excited into the minimum of the CB through the gap energy. At the transition time procedure, if these electrons are disorganized, the density of their states $\rho(h\nu)$, ($h\nu$: photon energy), and tailing into the energy gap. This tail of $\rho(h\nu)$ growing into the gap energy is known as the Urbach tail, as demonstrated in **Figure II.15**. Therefore, the absorption coefficient $\alpha(h\nu)$ tails off in exponential mode, and the energy associated with the corresponding tail is called the Urbach energy [66]. Thus, the width of the tails of the localized states in the gap region is attributed to defects or trap state levels within the bandgap, and the absorption coefficient follows an exponential relationship with the energy [32]:

$$\alpha = C \exp\left(\frac{h\nu - E_b}{E_U}\right) \quad (II. 11)$$

Where C is a constant, $h\nu$ is the incident energy, and E_U is the Urbach energy, which is obtained by taking a linear fit (slope) by plotting $\ln(\alpha)$ vs. $h\nu$.

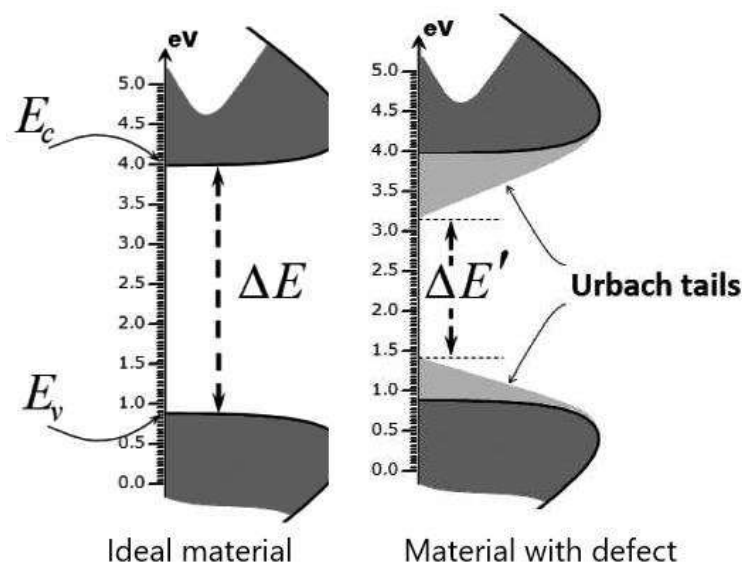


Figure II.15: Urbach tails description [66].

II.4.5 Thickness measurement

Film thickness is the most common and significant factor in the investigation of sample characteristics. The film thickness was determined using various techniques.

✚ Weight difference method

The thickness of the deposited thin film can be measured using the weight difference technique (Eq. II. 12), which is easy and practical [66].

$$th = \frac{\Delta m}{\rho \cdot S} \text{ (nm)} \quad (\text{II. 12})$$

Where

- ρ denotes the bulk density of the material.
- Δm is the difference in the substrate mass before (cleaned substrate) and after (substrate + thin film) the deposition.
- S is the deposited surface.

✚ SEM micrographs

In this case, the film thickness can be directly estimated by SEM observation of the edges or cross sections of the samples. Usually, in cross-sectional SEM, the sample needs to be cut. (See the example in *Figure II.16*).

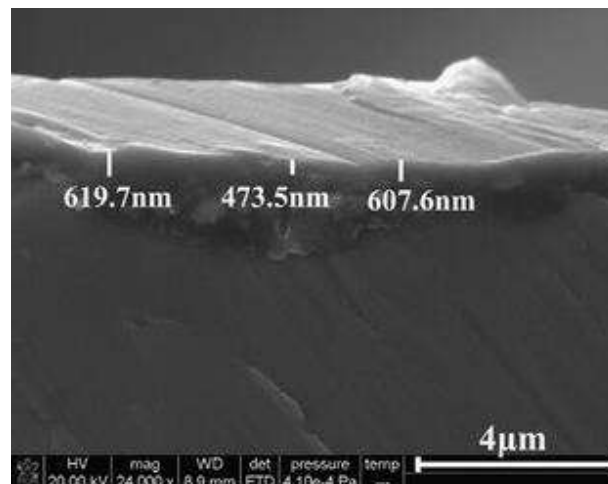
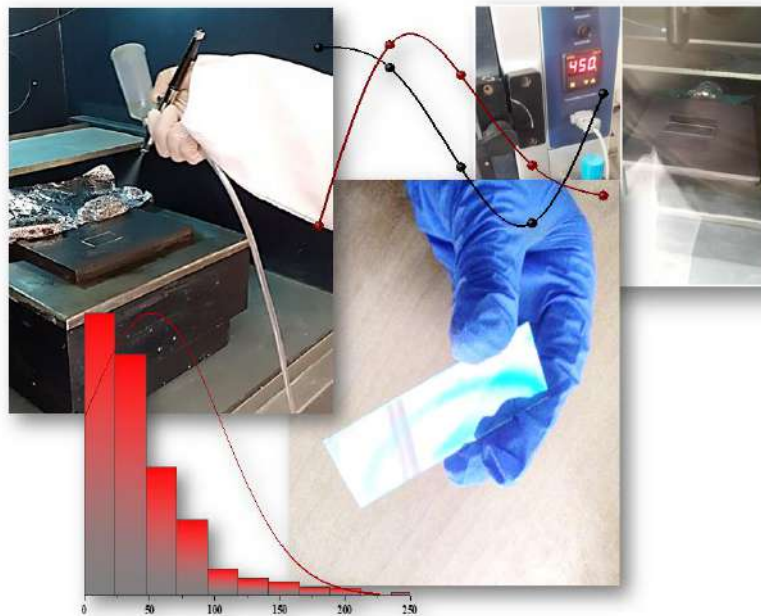


Figure II.16: SEM cross-section image (show the direct thickness estimated)[102].

Chapter III.

Synthesis & Characterization of pure, Doped, and Co-doped ZnO Metal Oxide Thin Films



This chapter aimed to synthesize pure ZnO, Al-doped, and Al, Ni co-doped ZnO thin layers by spray pyrolysis method. The obtained were investigated using structural, morphological, and optical characterization tools. The pure and doped ZnO thin films also were tested in the photocatalytic degradation activity for MB dye under UV light irradiation.

III.1 Introduction

A lot of studies are extensively proved the exclusive properties of nano-layers that belong to the SC materials, due to their unique properties which are being used in a several applications [1,2] such as gas sensors [2], antimicrobial [3], antibacterial [4] and photocatalytic degradation of organic dyes [5]. Since photocatalysis shows significant degrading efficiency without needing complicated technology, it is a viable, affordable, and advantageous method of dealing with polluted wastewater [13,14,31]. Additionally, thin films have a number of benefits over powder nanoparticles in the photocatalytic procedure, including ease of use, controllability, and avoidance of expensive powder cleaning and recycling after each degradation [9]. In general, doping ZnO thin films can increase or improve their photocatalytic activities. Therefore, the present chapter's study's object is synthesizing undoped, doped, and co-doped ZnO thin films by spray pyrolysis. The obtained films were analyzed by the characterization tools mentioned in *Chapter II*. Then they were tested in the photocatalytic activity by using MB as a pollutant organic dye.

III.2 Thin films Elaboration

III.2.1 Preparation of the substrates

The films were prepared on inexpensive and helpful common glass substrates (7.5 cm × 2.5 cm × 1 mm). The substrates were cleaned in an ultrasonic ethanol bath for 15 min. Then they rinsed with distilled water to remove any pollutants on their surfaces.

III.2.2 Preparation of thin films by spray pyrolysis

This section uses nanocrystalline films of pure ZnO, Al-doped ZnO, and (Al, Ni) co-doped ZnO (labeled as Z, to Z4) were prepared on glass substrates. *Figure III.1*. Shows the Spray pyrolysis equipment used in this study. The films were prepared at the **LRPPS laboratory** in the physical department of Ouargla University.



Figure III.1: Spray pyrolysis equipment used in LRPPS laboratory (Inset shows the obtained pure ZnO film).

Typically, solutions were produced by using an appropriate amount of zinc acetate dihydrate ($\text{Zn}(\text{CH}_3\text{COO})_2 \cdot 2\text{H}_2\text{O}$) as a starting ZnO precursor to generate thin layers via spray pyrolysis. First, 0.1 M of the precursor was dissolved at 80°C in DW: Ethanol: Methanol with a molar ratio: of 5:3:2 respectively. Following that, acetic acid drops were applied to it.

To obtain the doped and co-doped samples, were added to the prepared precursor solutions of 2 wt% of aluminum acetate ($\text{Al}(\text{OH})_2(\text{CH}_3\text{COO})$) as Al source (the sample labeled as Z1). For the co-doped, there was an addition to the solution amount of 2, 3, and 4 wt% to the ZnO:Al solution from the source and nickel chloride hexahydrate ($\text{NiCl}_2 \cdot 6\text{H}_2\text{O}$). The co-doped layers are labeled as Z2, Z3, and Z4 respectively. The solutions were then sprayed at 450°C onto a glass substrate that had been prepared previously. With a ~8 min deposition period, a 0.5 mm nozzle width, and a distance (nozzle–substrate) of approximately 35 cm, the flow rate reached 5 ml/min. Notably, the conditions for all the films grown by spray pyrolysis were the same.

• **Characterization of films**

After the preparation of the films, they should be analyzed using the previously mentioned characterization tools (*Chapter. II*). The physical properties of the samples are discussed below:

III.3 Results and Discussion

At first, the film thickness measurements were performed by the weight difference method using (Eq *II.12*) with $\rho = 5.61 \text{ g/cm}^3$ for zinc oxide in its bulk form. The ‘‘th’’ values for the obtained samples are listed in *Table III.1*.

III.3.1 Optical Characterization

The transmittance and absorbance spectra of the film measurements between 300 and 800 nm in wavelength are displayed in *Figure III.2 (a, b)*. As we can see the transmittance and absorbance change oppositely. The films have a high transmittance in the visible range. They were transparent in 400-800 nm, with average T% ranging between 81~ 79 %. In addition, *Figure III.2 (a)* The Z, Z1, Z2, Z3 and Z4 Owing to the doping effects, the films vary slightly near the UV absorption edge, moving toward shorter wavelengths near 370 nm. This phenomenon is mainly attributed to the Burstein–Moss effect [103].

Tauc Equation (Eq. *II.10*) was used to estimate the E_g of Samples and α is estimated by (Eq. *II.9*).

Figure III.3 (a-e) demonstrates the optical gap value estimation using the Tauc plot in the absorption edge zone. It is evident from the figures (*Figure III.3 (a-e)*) that the bandgap values ranged from 3.22 to 3.28 eV for the obtained samples. The Z1 result shows that the doped ZnO by Al is augmented by the optical band gap. Unlike the doped by Ni displayed a remarkable decrease in its E_g value, which was associated with an increase in the addition of Ni.

The Urbach energy was also obtained by taking a linear fit (slope) by plotting $\ln(\alpha)$ vs $h\nu$. The results obtained are 0.256, 0.154, 0.226, 0.230 and 0.238 eV for Z, Z1, Z2, Z3, and Z4, respectively, which increased with the decrease of the Optical gap (*Figure III.3 (f)*). This increase can be attributed to the narrowing of the E_g of intrinsic ZnO (3.37 eV).

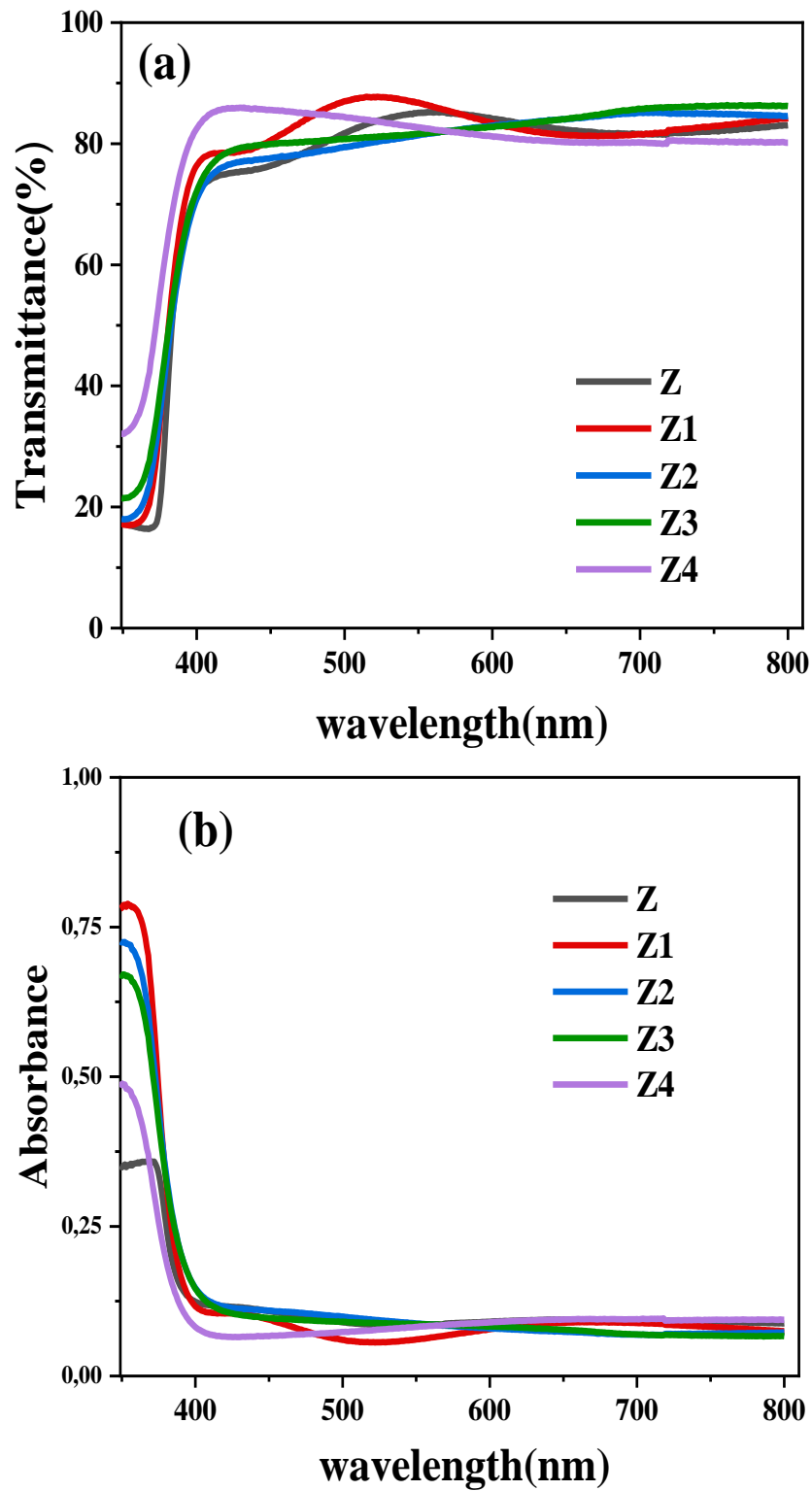


Figure III.2: a) Transmittance spectrum, b) Optical Absorbance spectrum of as-deposited thin films (ZnO, Al:ZnO, Al:Ni: ZnO).

Chapter III. Synthesis and Characterization of Pure, Doped and Co-doped ZnO Metal Oxide Thin films

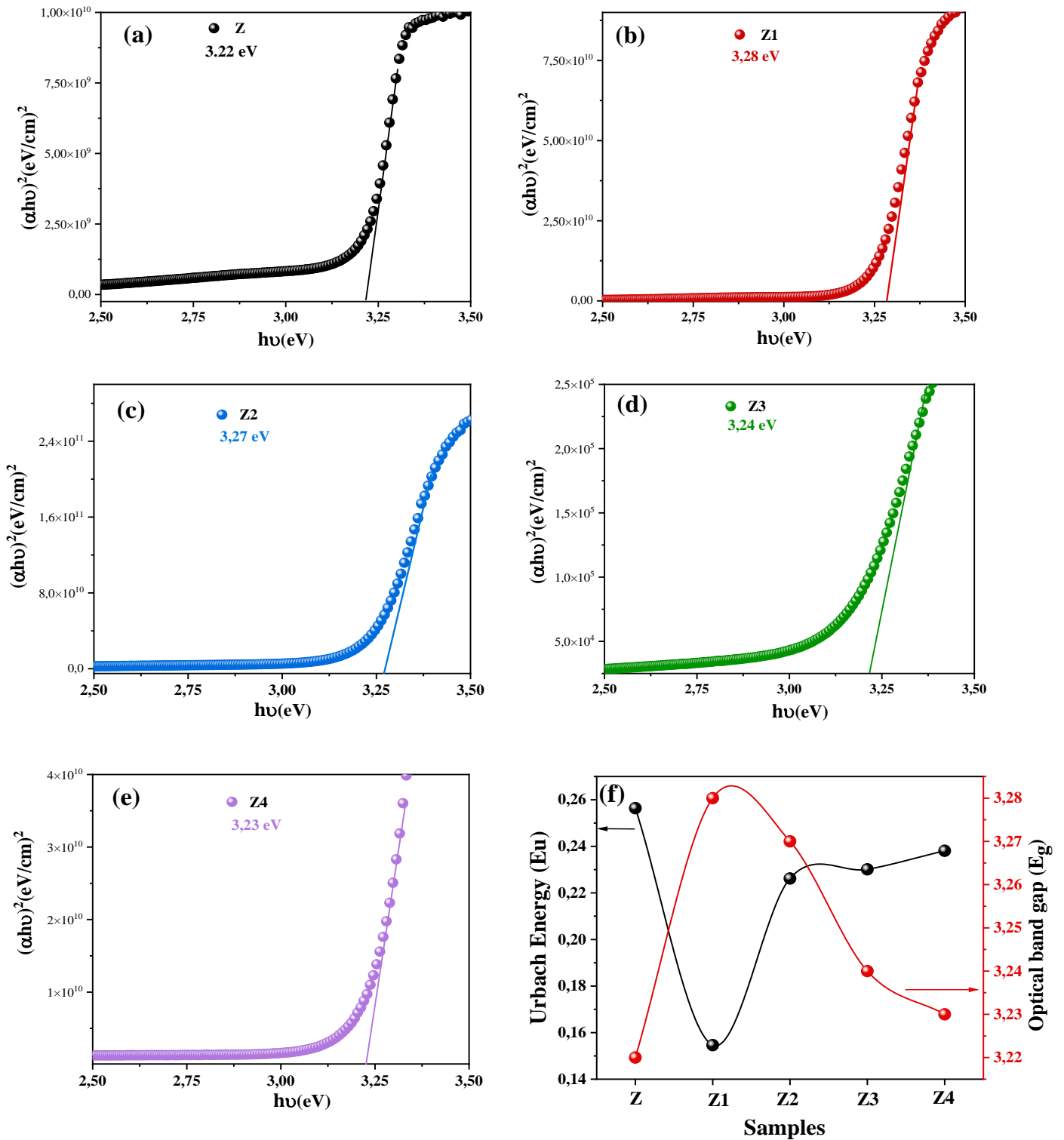


Figure III.3: (a-e) Tauc plot of the sprayed layers, f) Variation of E_g and E_u of the sprayed layers.

Chapter III. Synthesis and Characterization of Pure, Doped and Co-doped ZnO Metal Oxide Thin films

Table III.1: Optical parameters of as-deposited Z, Z1, Z2, Z3 and Z4 films.

<i>Thin films</i>	<i>T (%)</i>	<i>E_g (eV)</i>	<i>E_u (meV)</i>	<i>th (nm)</i>
ZnO pure (Z)	81.0	3.22	0.256	282
2% Al-ZnO (Z1)	80.6	3.28	0.154	208
2% Al 2% Ni- ZnO (Z2)	79.6	3.27	0.226	114
2% Al 3% Ni- ZnO (Z3)	79.4	3.24	0.23	184
2% Al 4% Ni- ZnO (Z4)	79.0	3.23	0.238	117

III.3.2 by X-Ray Diffraction study

It is extremely necessary to use XRD to determine the crystalline nature and phase of the produced samples. Consequently, X-ray diffraction was used to examine the structural crystallinity in the different resultant films, scanning a 2θ (diffraction angle) between 10° and 70° , as seen in **Figure III.4 (a)**. As we can see from **Figure III.4 (a)**, the films prepared by the spray pyrolysis indicate specified reflections. at $2\theta = 31.8^\circ, 34.5^\circ, 36.3^\circ, 47.6^\circ, 56.6^\circ, 63.0^\circ$ and 68.1° matching with (100), (002), (101), (102), (110), (103) and (112) planes, respectively, according to the wurtzite hexagonal ZnO structure (JCPDS no. 1-70-2551) [104]. Low doping concentrations in ZnO did not result in any aluminum-related peaks in the XRD patterns, suggesting that aluminum did not alter the ZnO polycrystalline structure. Unless Ni which is indicated in the Z4 sample may be due to the presence of 2 wt% of Al in crystalline lattice structure and with the addition of Ni. The Z4 pattern contains a very small peak detected at $2\theta = 42.7^\circ$ matched with (200) plane correspond to the cubic $\text{Ni}_6\text{Zn}_4\text{O}$ (JCPDS no. 1-075-0273) [105]. Furthermore, the XRD analysis demonstrated the excellent crystal structure of the sprayed layers.

III.3.2.1 Structural parameters

The crystallite sizes (D_{cs}) of the samples were estimated using Scherrer's formula (Eq. II.5). As we can see in the films Z, Z1, Z2 and Z3, D_{cs} is decreased with an increase in the doped concentration, which indicates that the doped amounts occupied interstitial sites in the ZnO lattice structure. In the Z4 layer, the D_{cs} is increased, and Ni is well substituted for Zn^{2+} in the unit cell due to the presence of the Al with small ionic radii Al^{3+} (0.53 \AA) and the matching of ionic radii of Ni^{2+} (0.69 \AA) as compared to Zn^{2+} (0.74 \AA) at the same tetrahedral fold coordination [105].

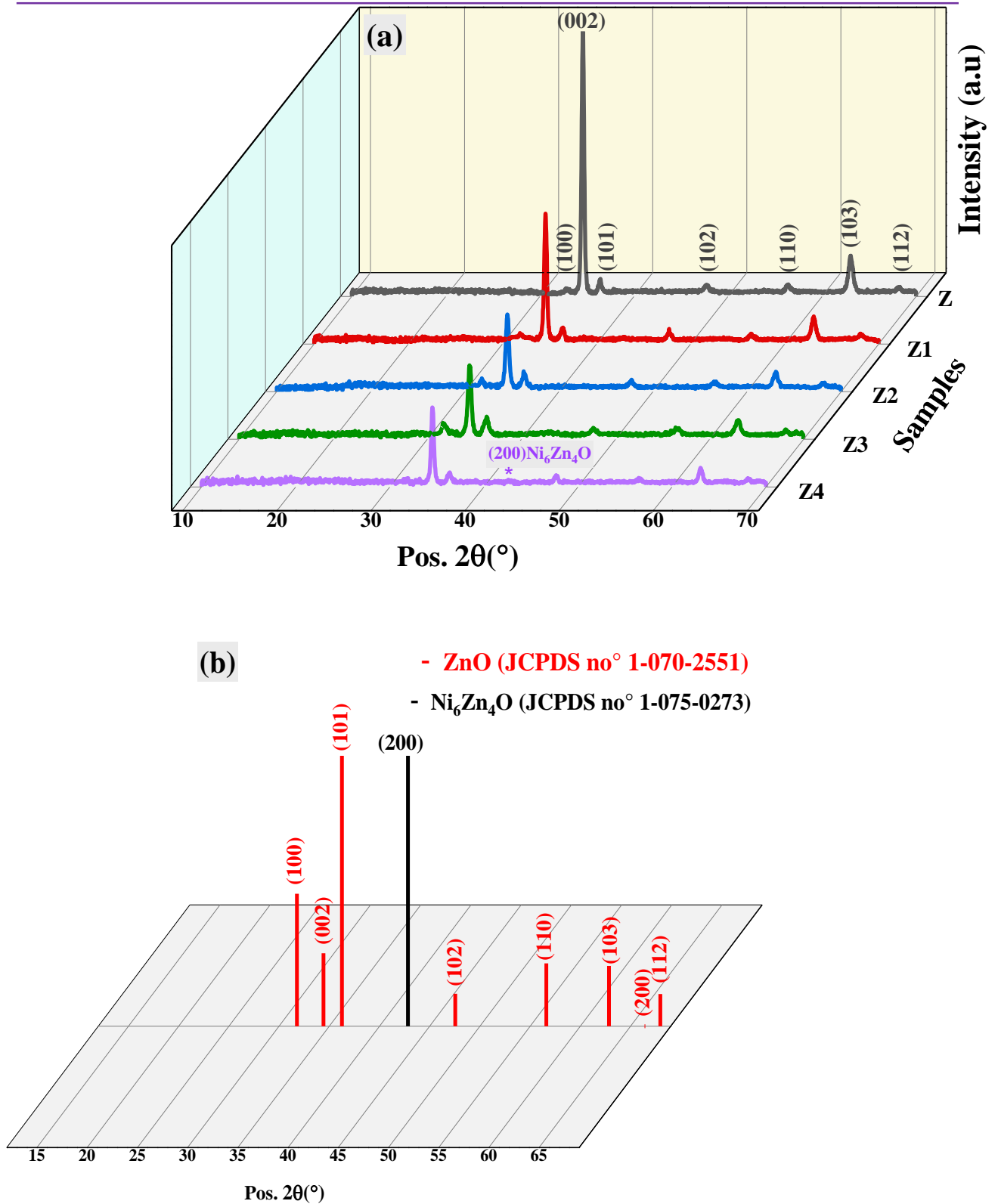


Figure III.4: a) The X-Ray diffraction patterns of as-sprayed films, b) the corresponding JCPDS cards pattern.

**Chapter III. Synthesis and Characterization of Pure, Doped and Co-doped
ZnO Metal Oxide Thin films**

D_{cs} of the sprayed films have been estimated using (Eq. **II.6**). The micro-strain (ϵ_{ms}) was calculated using the following relation (Eq. **II.7**).

Figure III.5 displays D_{cs} , ϵ_{ms} , and δ . It also shows the opposite correlation between them.

TC_{hkl} (texture coefficient) is also an important parameter in the XRD study used to know the growth preferential orientation of the grains in the deposited layers that may give an idea about the probability of nanocrystallite formation, which was calculated for every plane from the diffraction data, using (Eq. **II. 2**). **Figure III.6** shows that the preferred orientations along the plane (002), that considerably higher TC_{hkl} values than the resting planes of the samples ($TC < 1$).

All the structural parameters have been measured and listed in **Table III.2**.

Table III.2: Structural parameters of as-deposited Z, Z1, Z2, Z3, and Z4 films.

Samples	2θ ($^{\circ}$)	hkl	TC	D_{cs} (nm^3)	ϵ (10^{-3})	δ (10^{14} lines/m^2)
Z	34.58	002	4.69	29.16	4.17	11.75
Z1	34.58	002	4.55	28.21	4.31	12.56
Z2	34.58	002	3.98	23.48	5.18	18.12
Z3	34.58	002	3.63	20.84	5.83	23.01
Z4	34.58	002	4.21	26.98	4.52	13.73

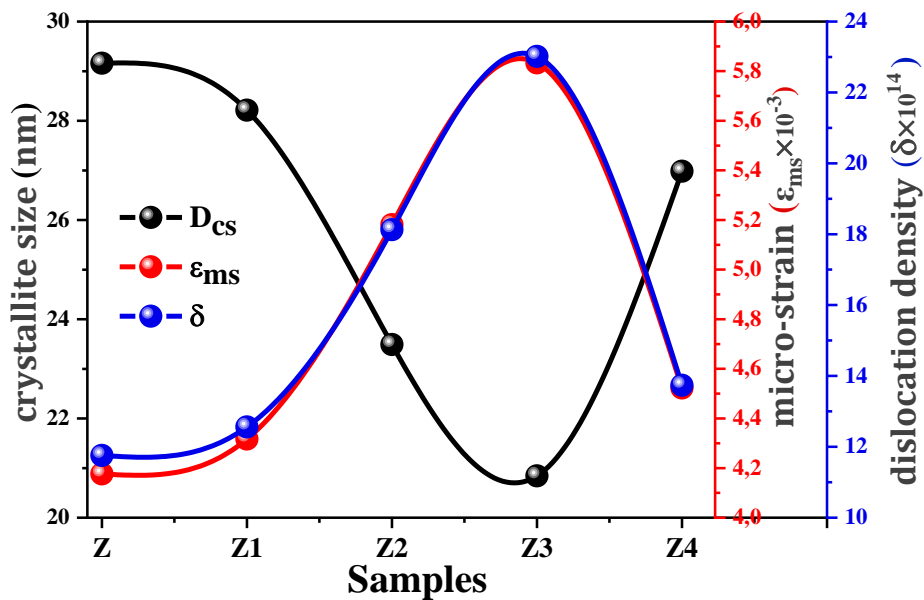


Figure III.5: Structural parameters (D_{cs} , ϵ_{ms}) and δ of the sprayed films.

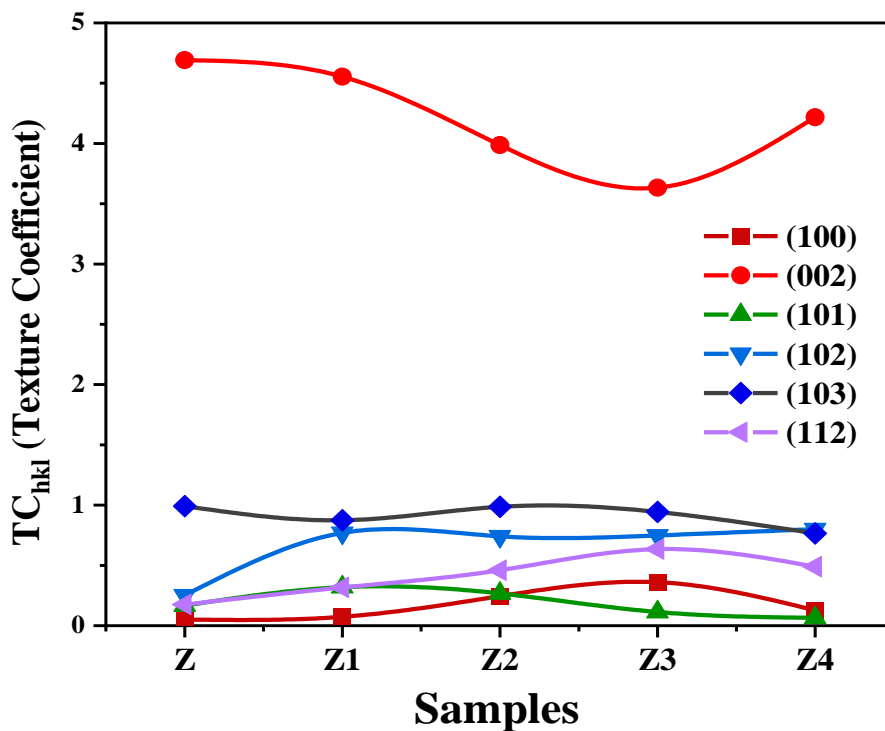


Figure III.6: Variation of the texture coefficient values for pure and doped ZnO thin films.

III.3.3 ATR-FTIR analysis

ATR-FTIR spectroscopy can be employed as an additional analytical technique for XRD investigations. As seen in **Figure III.7**, FTIR investigations were carried out in the transmission mode between 400 and 4000 cm^{-1} . In the fingerprint area, metal oxides often exhibit absorption at particular wavenumbers [19]. The pure and doped ZnO layers samples reveal the vibration of Zn–O stretching at approximately 418, 442, 459, 523 and 552 cm^{-1} [106–109], as illustrated in **Figure III.7** spectrum. For each sample, it observed a broad absorption band located around 911 ± 6 and 764 cm^{-1} characteristic absorption bands between 1240 and 660 cm^{-1} corresponding to the glass substrates [110]. In addition, for the Z4 sample which is co-doped by 2% of Al and 4% of Ni, observed the stretching vibrations of the Ni–O bonds at 520 cm^{-1} [111]. The absence of Ni- and Al- in the Z1, Z2 and Z3 transmittance spectra further confirms that the Al and Ni ions were completely doped with the regular lattice sites of ZnO.

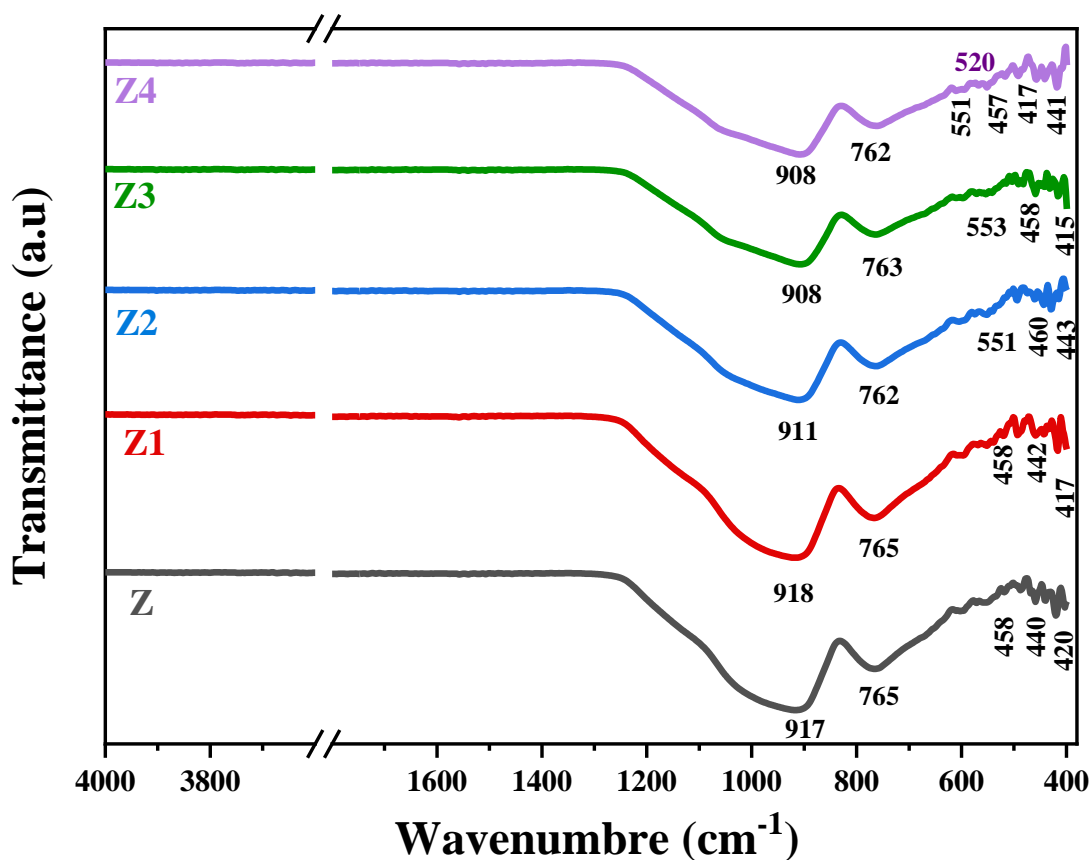


Figure III.7: ATR-FTIR spectra of sprayed films.

III.3.4 Surface morphology

The surface morphologies of the thin films were determined by SEM, are shown in **Figure III.8** and **Figure III.9**. The SEM micrographs revealed notable variations in the surface morphology based on the top surface. The SEM micrographs appear a remarkable roughness with a disorganized granular structure along the surface, which was crack-free. As observed in **Figure III.8 (a, b)** for Z and Z1 SEM micrographs, the presence of aggregates along the film network structure. The nanograin agglomerations decrease by Al doping. Z and Z1 SEM show also some nanorice-like scattered along the surface of the scanned area. Z and Z1 types of nanostructures exhibit nanoagglomerations of grains with several shapes. Thus exhibit a greater surface-to-volume ratio than that of the smooth layers. Additionally, the presence of the nanoporous morphology in Z and Z1 can augment the photocatalytic activity rate.

Figure III.9 displays the results of SEM images of Z2, Z3 and Z4; they have homogeneous and uniform grain distribution on the surface with a spherical shape overlapping. In Z2 and Z3 samples, the grain sizes became smaller with increased Ni doping concentration, indicating that appropriate Al and Ni doping content could improve the Zinc Oxide surface morphology of thin films. However, the presence of aggregates or big grains on the layer can affect its homogeneity but it may display a rough texture that helps dye adsorption during photocatalytic processes. The histogram distributions of the grain size of the samples (**Figures III.8** and **III.9**) display average grain size confirming the D_{cs} measured by the XRD study with a slight difference, this lateral can attributed due to the D_{cs} was measured for only the high intense peaks (002).

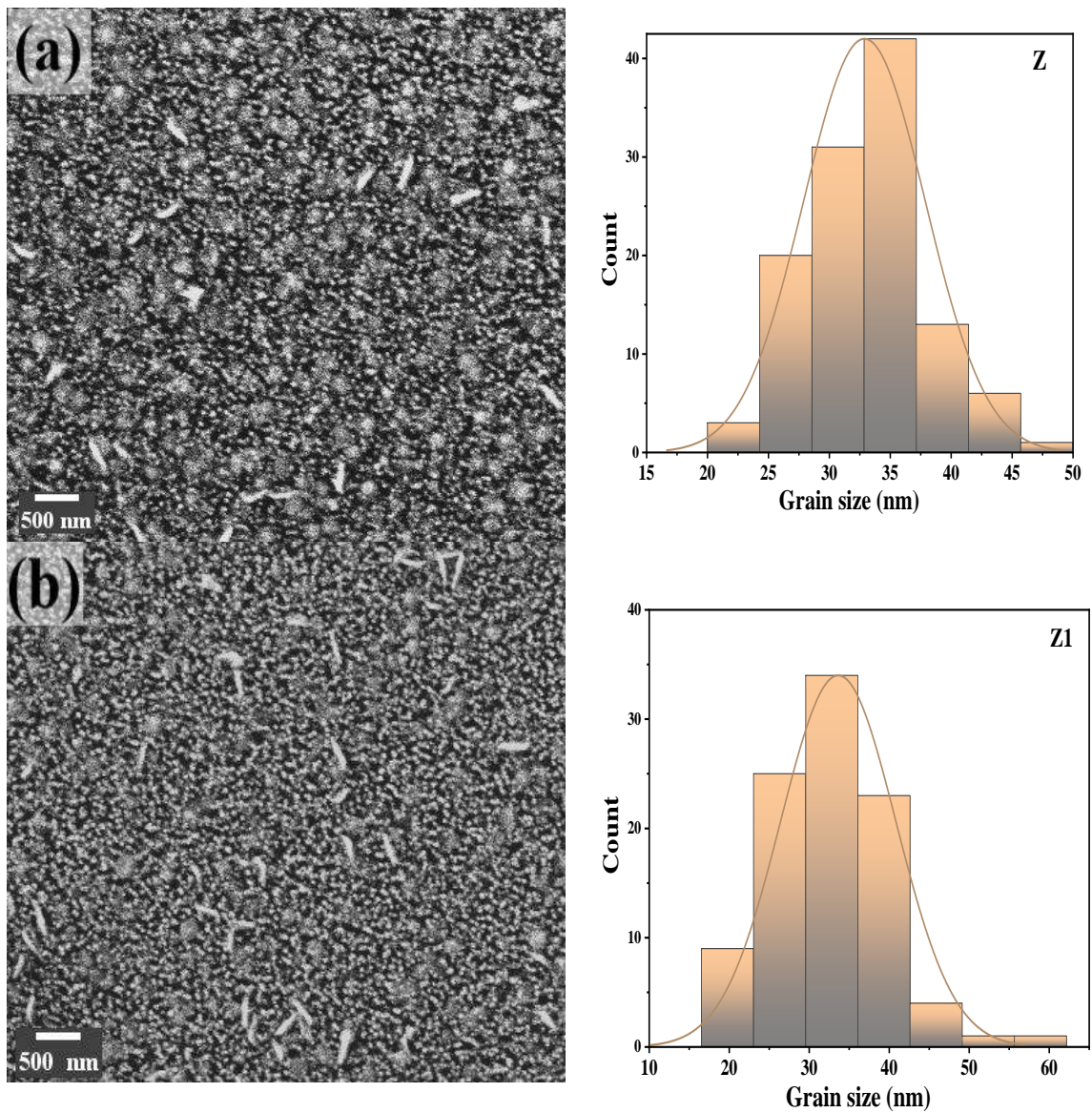


Figure III.8: SEM surface with the histograms of grain size of as-sprayed films a) Z, b) Z1.

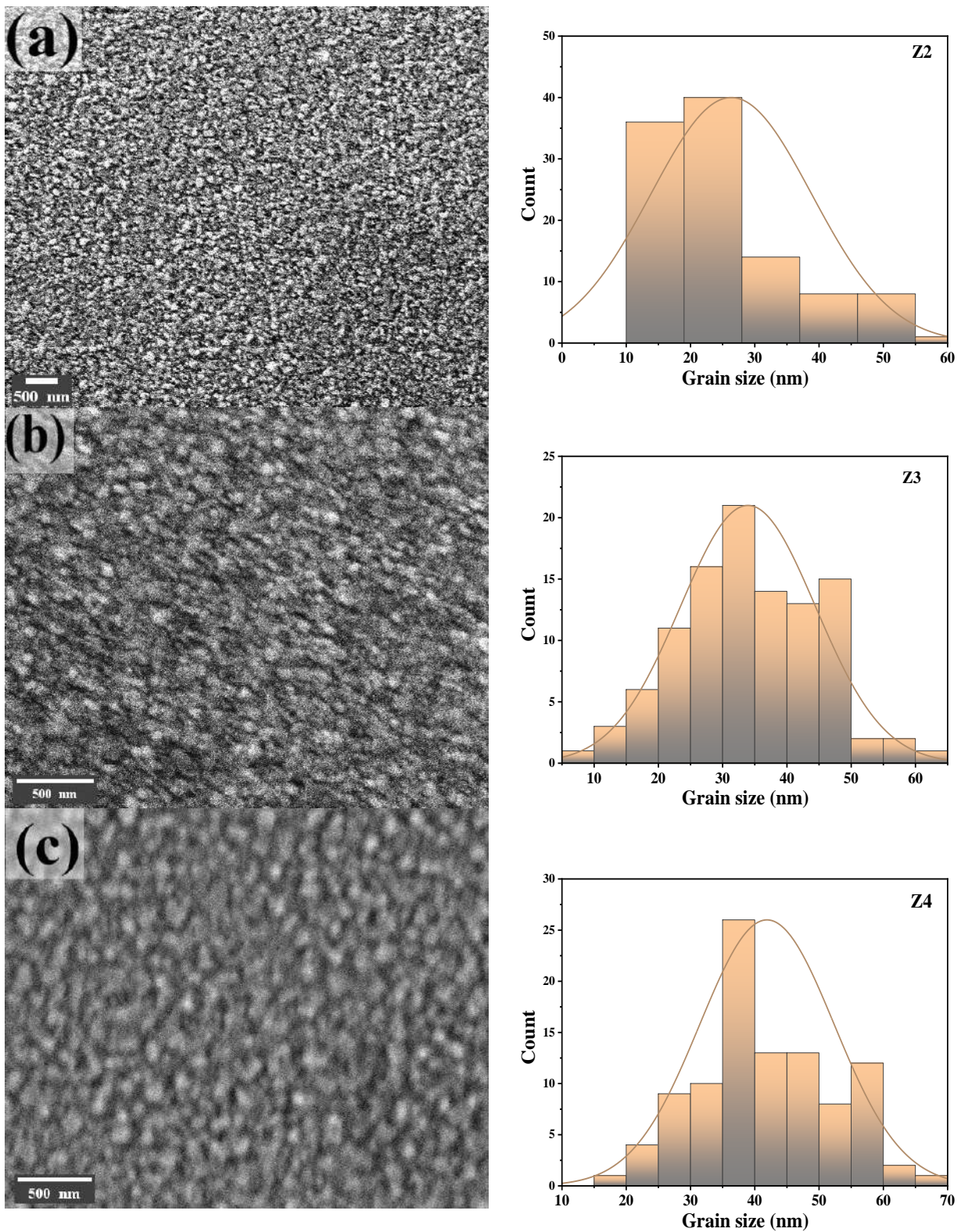


Figure III.9: SEM surface with the histograms of grain size of co-doped sprayed films a) Z2 b) Z3 and c) Z4.

Chapter III. Synthesis and Characterization of Pure, Doped and Co-doped ZnO Metal Oxide Thin films

As shown in **Figure III.10**, EDS was used to verify the chemical elements of the pure and doped ZnO samples sprayed on a glass substrate. To verify the existence of the fabricated components Aluminum, Zinc, Nickel and Oxygen were detected in this study. Additionally, because of the glass substrate, the EDS spectrum also revealed the presence of Silicon, Oxygen and Calcium [98] and the Au peak generated from the Au electrical contact. The presence of glass substrate elements also has been observed in the FTIR study.

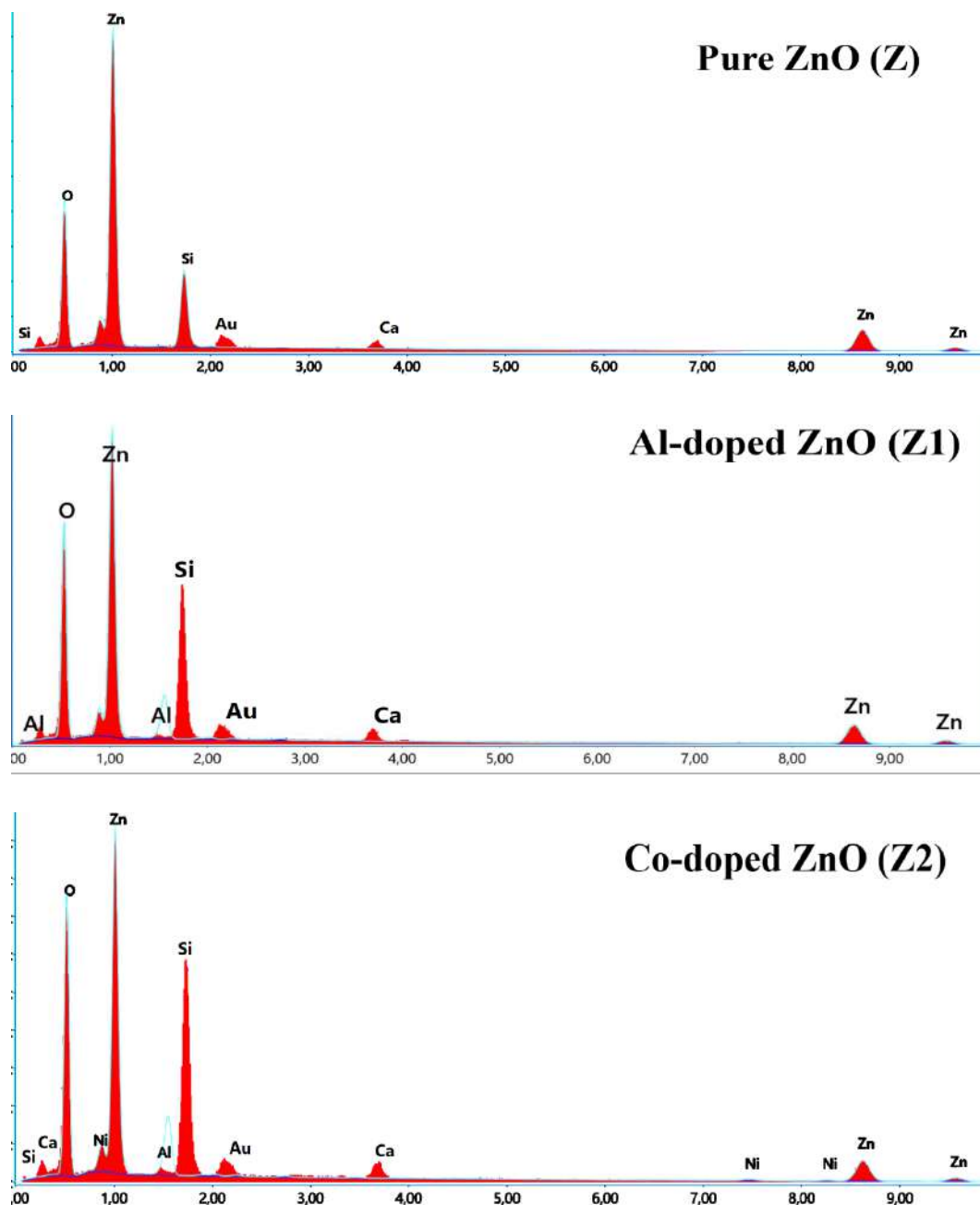


Figure III.10: EDS spectra of undoped and doped of as-sprayed films.

III.4 Tested of thin films in the photocatalytic activity

III.4.1 Experimental protocol (Photodegradation test)

The photocatalysis tests were evaluated by measuring the photodegradation of pollutant methylene blue (MB) solution under UV irradiation. A sample of $1.5 \times 2.5 \text{ cm}^2$ dimensions was horizontally immersed in an 8 ml MB volume solution of initial concentration $2.5 \times 10^{-5} \text{ mol/L}$. The irradiation source was by a mean of a Philips germicide lamp (G15T8/15W) emitting UVC light ($\lambda=254 \text{ nm}$) which was fixed at a distance of 10 cm above the non-transparent glass cell containing the film and the MB solution, settled on a magnetic agitator to ensure the whole contact between the solution and the surface film. A magnetic stirring in the dark for 20 minutes was sufficient to achieve the adsorption-desorption equilibrium. To follow the evolution of photocolorization of the pollutant, the concentration spectra of the MB were recorded, after each 30 min of UV irradiation, 3 ml of MB solution was analyzed and this volume was sent back. The concentration was determined by registering the absorbance at $\lambda = 664 \text{ nm}$ of the MB. The procedure's efficiency was determined using Eq. **III.1** [2]:

$$\text{Dye degradation rate \%} = \left(\frac{C_I - C_t}{C_I} \right) \times 100 = \left(\frac{A_I - A_t}{A_I} \right) \times 100 \quad (\text{III.1})$$

Where C_t , A_t are the concentration, absorbance at actual measurement, respectively. C_I , A_I are initial concentration, absorbance values, respectively.

III.4.2 Photocatalytic degradation

The organic pollutant used in this study was an aqueous MB solution, and its purpose was to examine the degradation behavior of the pure and doped films. UV-vis at the max absorbance during the procedure was used to quantify the dye's evolution, as demonstrated in **Figure III.10 (a-e)**. The MB absorption peak ($\lambda_{\text{max}} = 664 \text{ nm}$), in line with the MB molecules. The rate of degradation increased with increasing duration of exposure to light. After 120 min, the photocatalytic degradation efficiency nearly vanished ($\eta\%$) by ~84% for pure ZnO. The degradation of the doped samples reached only 26% for the Al-ZnO, and decreased to 23 and 22% for 2%:Al- 3%:Ni-ZnO (Z4) and 2%:Al- 2%:Ni-ZnO (Z3) samples, respectively. The degradation efficiency of the Z4 compared to Z3 and Z2 is increased to 46% after 120 min. **Figure III.10 (f)** shows that the pure one exhibited high efficiency. In this case, doping with Al

Chapter III. Synthesis and Characterization of Pure, Doped and Co-doped ZnO Metal Oxide Thin films

did not augment the photocatalytic performance, which may be due to the larger optical band gap, which may demand a large photon energy for the catalyst exciton, and the E_g of undoped-ZnO may also exhibit a native defect, which makes it narrower than the intrinsic one (3.37 eV). Nevertheless, the high Ni concentration in the AZO film narrows its E_g and increases the degradation rate. However, in this case, the opposite effect on the photocatalytic degradation performance can be attributed to several parameters that should be fixed from the starting conditions (synthesis conditions) next time. Moreover, our co-doped films can work with extra performance with other organic dyes that have other properties (such as anionic dye).

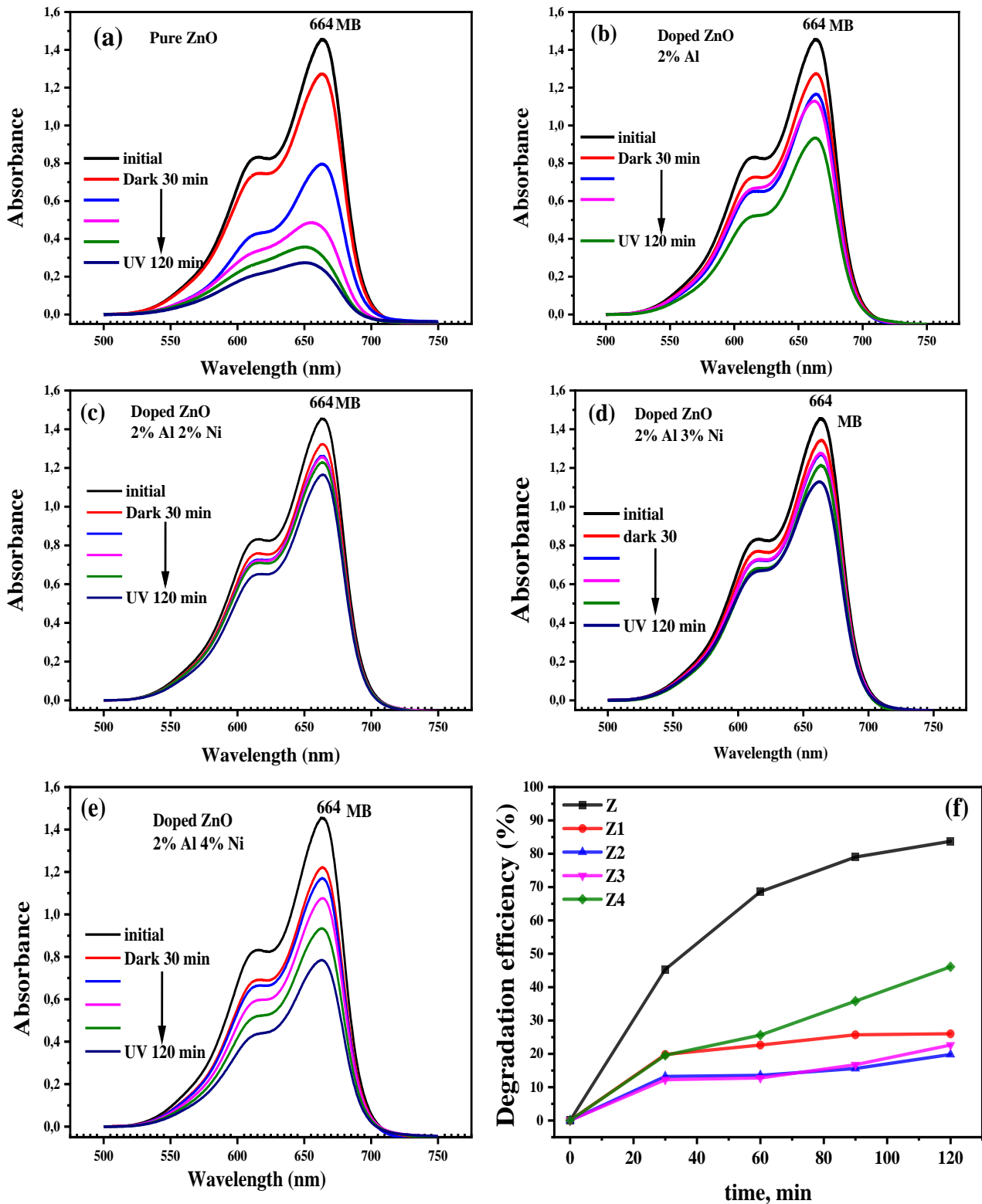


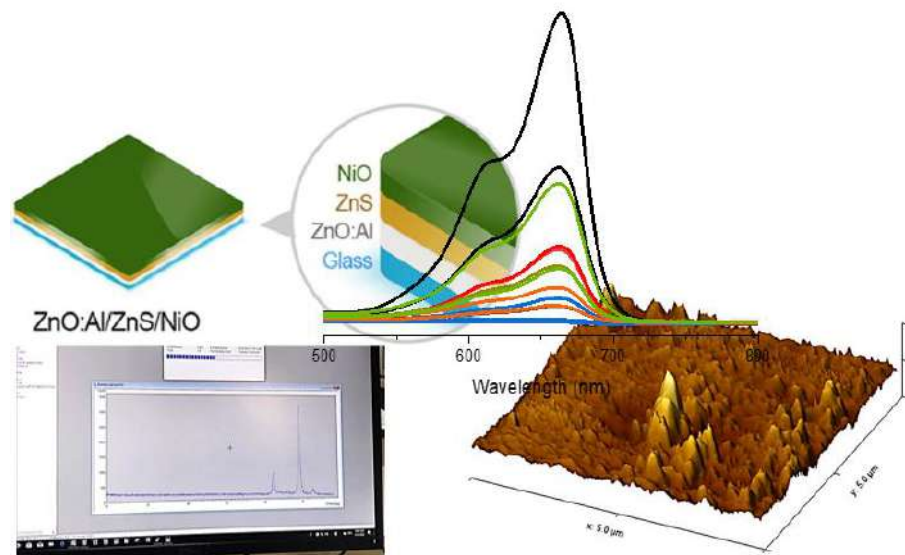
Figure III.11: (a-e) MB UV-visible spectra under UV illumination using as-sprayed Z catalysts, f) MB Photodegradation efficiency of as-sprayed films.

III.5 Conclusions

This work demonstrated a simple cost-effective spray pyrolysis method to fabricate pure ZnO, Al-doped ZnO, and Al-Ni: co-doped ZnO on a glass substrate. The coated films were characterized by typical techniques. XRD study demonstrated the existence of high ZnO crystallinity with Wurtzite structure preferentially oriented along the planes (002) perpendicular to the surface of the substrate. SEM characterization indicated the presence of aggregates along the film network structure. The EDS mapping confirmed the existence of Al and Ni elements in the sprayed doped and co-doped films. The optical study of the sprayed layers have been reported that the E_g value of Al- ZnO is larger than the pure and decreases with the second doped by Ni. The results indicate that pure ZnO exhibits a high photodegradation efficiency (~84%) against MB within 120 min under UV light. This work is suggested for cost-effective synthesis of pure ZnO film by spray pyrolysis for efficient photocatalytic activity at first. Second, the doped and co-doped ZnO films have a good optical and structural characterization that can suggested for other optoelectronic applications. Furthermore, this section leads us to the conclusion that the selection of SC thin films for use as photocatalysts affects both their native quality and the conditions under which they are synthesized, both of which affect the final physical attributes of the samples. In general, doping ZnO thin films can increase or improve their photocatalytic activity.

Chapter IV.

Doped and Coupled ZnO for Enhancing Photocatalytic Activity



The goal of this chapter is to create ZnO:Al/ZnS/NiO heterojunction multilayers using spray pyrolysis and low-cost spin coating as photocatalysts for the degradation of organic dyes. Tools for structural, morphological, and optical characterization were used to examine sample characteristics.

IV.1 Introduction

Thin-layer SCs have been improved under a variety of light sources (UV and sunlight) when used as photocatalysts. Multilayer structures, which have two or more layers of SC structures, are alternate semiconductor-deposited films developed for optoelectronic applications [31,112] due to their superior optical and electrical properties compared with those of typical monolayers [9], whereas few studies exist on photocatalytic applications [31]. Indeed, from the above chapter, we concluded that the selection of photocatalyst SC thin layers is not only based on their intrinsic characteristics but also on the elaboration and growth film conditions, that influence their obtained characteristics. Moreover, the enhancement of these semiconductors forbids the challenging aspects of photocatalytic performance that weaken the process. Therefore, the object of the present chapter study toward the synthesis of Al-ZnO as a signal layer and Al-ZnO/ZnO, Al-ZnO/ZnS/NiO as multilayer thin films. To our knowledge, this is the first study on the role of Al-ZnO/ZnS/NiO in the photocatalytic activity of organic dyes under visible and solar light irradiation. The main idea of doping ZnO and coupling it simultaneously is to enhance its photocatalytic degradation performance. Thus, the doped Al-ZnO was coated with ZnS and NiO to improve charge separation.

IV.2 Elaboration of thin films (Thin Films Preparation Protocols)

This section uses thin films Al-ZnO monolayer, Al-ZnO/ZnS bi-layer, and Al-ZnO/ZnS/NiO tri-layer (labeled as **Z**, **ZS**, and **ZSN**, respectively) were deposited on glass microscope lamella as substrates (3.6 cm × 2.5 cm × 1 mm).

IV.2.1 Signal-layer Preparation by Sol-gel

First, it was necessary to clean the substrates before they were coated, with ethanol and deionized water in an ultrasonic bath for 15 min to remove any contaminants on the surface of slide substrates.

We made a **Z** layer as the first bottom layer by a spin-coating sol-gel technique using a 0.1M aqueous solution of zinc acetate dihydrate ($\text{Zn}(\text{CH}_3\text{COO})_2 \cdot 2\text{H}_2\text{O}$). Aluminum acetate ($\text{Al}(\text{OH})_2(\text{CH}_3\text{COO})$) was added as an aluminum source, with a concentration chosen 2wt% to the previous solution. The precursor solution was prepared by dissolving the required amount of zinc acetate in absolute ethanol ($\text{C}_2\text{H}_6\text{O}$) used as the solvent whereas monoethanolamine (MEA: $\text{C}_2\text{H}_7\text{NO}$) was used as the stabilizer. The molar ratio of the precursor and the stabilizer (MEA)

was kept at 1:2. The solutions were stirred for 2 h using a magnetic stirrer at 75°C to get a clear and homogeneous transparent sol, this sol was aged for 48 h. The sol was then dropped on the substrate and then it was coated for 25 s using a spin coater with 1500 rpm at ambient temperature. and then each coating was followed by subsequent drying at first at 200 °C for 10 min to evaporate the residue solvents in the film, the same procedure (spin-dry) was repeated 6 times to obtain the film with the desired thickness. At last, the final coated films were annealed in the tubular furnace for at 500°C for 90 min then let cool to room temperature.

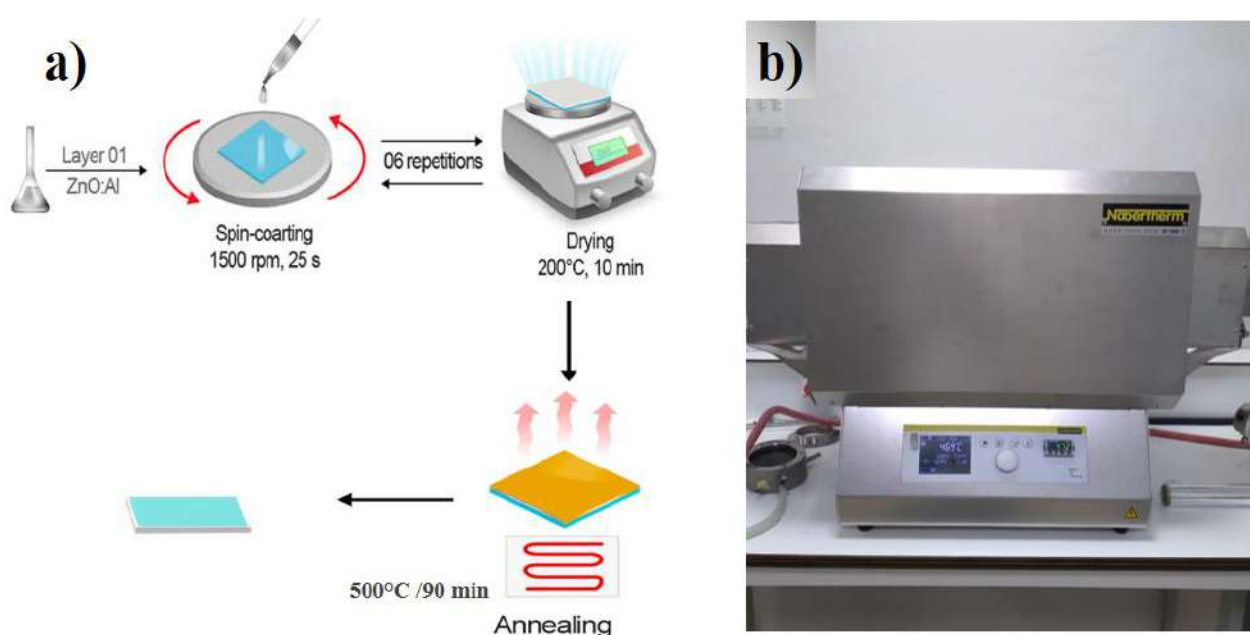


Figure IV.1: a) descriptive diagram of the stages of deposition of the thin layers by spin coating, b) a tubular furnace was used for annealing in the CRAPC Ouargla.

IV.2.2 Multilayer Preparation by Spray Pyrolysis

In the next step; to obtain **ZS** and **ZSN** multilayer, the 2nd and 3rd upper layers (ZnS and NiO films) were coated by the spray pyrolysis technique. Typically, elaborated independently in the appropriate amount of thiourea (SC (NH₂)₂) with zinc acetate dihydrate (Zn (CH₃COO)₂·2H₂O) and nickel chloride hexahydrate (NiCl₂·6H₂O) were employed as starting precursors. First, using a 0.1M solution of zinc acetate (Zn (CH₃COO)₂·2H₂O) and 0.1 M of thiourea (SC (NH₂)₂) dissolved in ultrapure water and some drops of acetic acid added in the solution to prevent solution deposition, were mixed for 30min with a magnetic stirring at 80°C (Molar ratio of Zn²⁺ to S²⁻ kept 1:1). On the other hand, NiO solution was obtained by dissolving nickel chloride in double distilled water with a molar concentration of 0.1 M. The solutions were left in

a magnetic stirring for 30 min at 80°C. Then, the fabrication process of ZnS over the prepared Z layer was by spraying the mixture of ZnS precursor solution onto a preheated substrate (Substrate + Al-ZnO as bottom film) for good quality polycrystalline films at a fixed T= 450°C, the spray flow rate of 5ml/min. The distance between the nozzle and the substrate was ~35 cm, with a nozzle diameter of 0.3 mm and the spraying time varied between ~8 min. The last step was to coat a NiO layer on the top of the ZS bilayers thin film, in the same manner. Notably, the conditions for all the films grown by spray pyrolysis were the same.

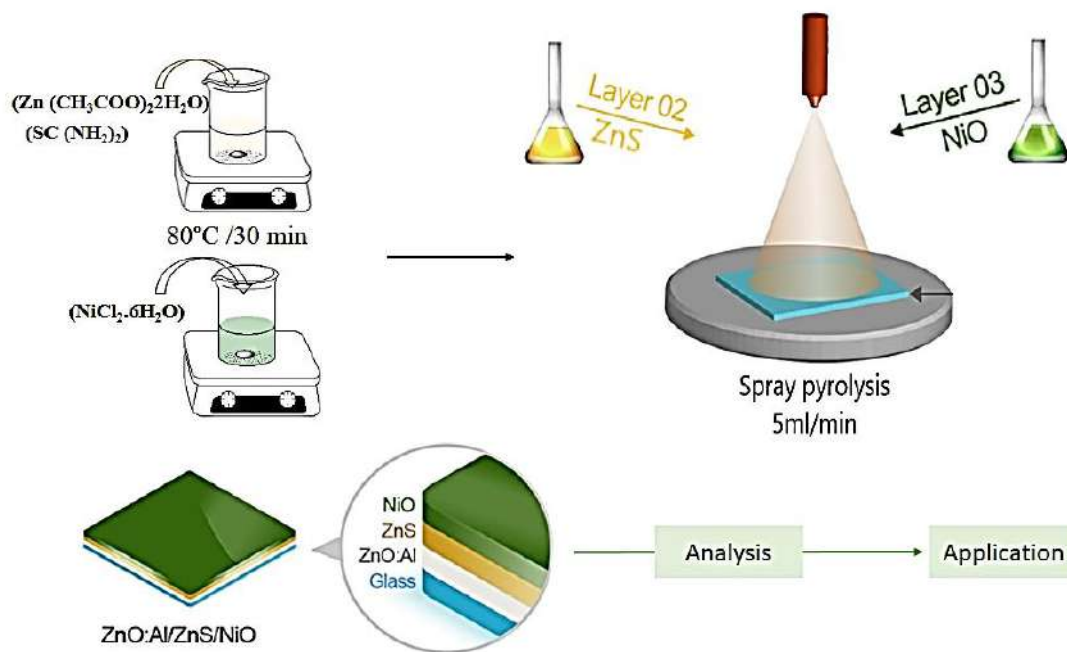


Figure IV.2: descriptive diagram of the steps of deposition of the thin layers by spray pyrolysis.

IV.3 Results and Discussion (Characterization of thin films)

IV.3.1 Structural analysis by XRD

It was essential to use XRD to clarify the nature phases of the produced films. Thus, utilizing XRD means with 2θ (diffraction angle) checking from 20° to 70° , the crystal structures of single Z, multilayer ZS, and ZSN layers were analyzed, as seen in **Figure IV.3 (a)**. As shown in **Figure IV.3 (a)**, the Z monolayer prepared by the spin technique indicated well-defined peaks at $2\theta = 31.9^\circ, 34.5^\circ, 36.4^\circ, 47.6^\circ, 56.9^\circ, 63.0^\circ$ and 68.2° corresponding with (111), (002), (101), (102), (110), (103) and (112) planes, respectively, identical to the ZnO wurtzite hexagonal

structure (JCPDS no. 1-75-576) [113]. Confirming the presence of the just Zinc Oxide phase in the XRD pattern (low doping concentrations in **Z**), the presence of several peaks suggests that the film is polycrystalline in nature. The **ZS** XRD exhibits the most intense peak, 28.7° of (111) plane of the zinc sulfide cubic phase (JCPDS no. 1-080-0020) [106], which is a high-intensity peak in the typical diffraction pattern of cubic ZnS with high crystallinity. Similarly, the NiO phase was found in the **ZSN** pattern has two additional peaks at $2\theta = 43.2^\circ$ and 62.7° , matching (200) and (220) planes of cubic-NiO (JCPDS no. 47-1049) [20]. Furthermore, the XRD study confirmed the good crystalline quality of the single- and multilayer samples.

IV.3.1.1 Structural parameters

The crystallite sizes (D_{cs}) of the three phases were estimated using Scherrer's formula (Eq. **II.5**) to estimate the dislocation density were using (Eq. **II.6**). The micro-strain (ϵ_{ms}) is related to FWHM (β) and can be calculated using (Eq. **II.7**).

When D_{cs} decreases, the lattice strain caused by internal surface tension causes compression, and as the surface area of the film grows, so does the number of crystal edges. As a result, when the crystallite size increased, there was less compression from the grain borders, which weakened the lattice strain. Additionally, because there were fewer grain barriers, there were fewer dislocation lines, indicating that the grain boundary was a trap for dislocations [97,98]. Accordingly, **Figure IV.3 (b)** displays the opposite correlation between D_{cs} , ϵ_{ms} and δ for every structural phase. All these structural parameters were calculated and are listed in **Table IV.1**.

Table IV.1: Structural parameters of mono- and multilayer samples.

Samples	phase	structure	2θ (°)	hkl	D_{cs} (nm ³)	ϵ_{ms} (10 ⁻³)	δ (10 ¹⁴ lines/ m ²)	RMS (AFM)
Z	ZnO	hexagonal	31.94	100	18.4	6.625	29.543	12.07
			34.60	002				
			36.42	101				
ZS	ZnS	cubic	28.78	111	10.9	13.389	84.451	10.66
SZN	NiO	cubic	43.14	200	15.4	4.507	42.004	21.36
			62.73	220				

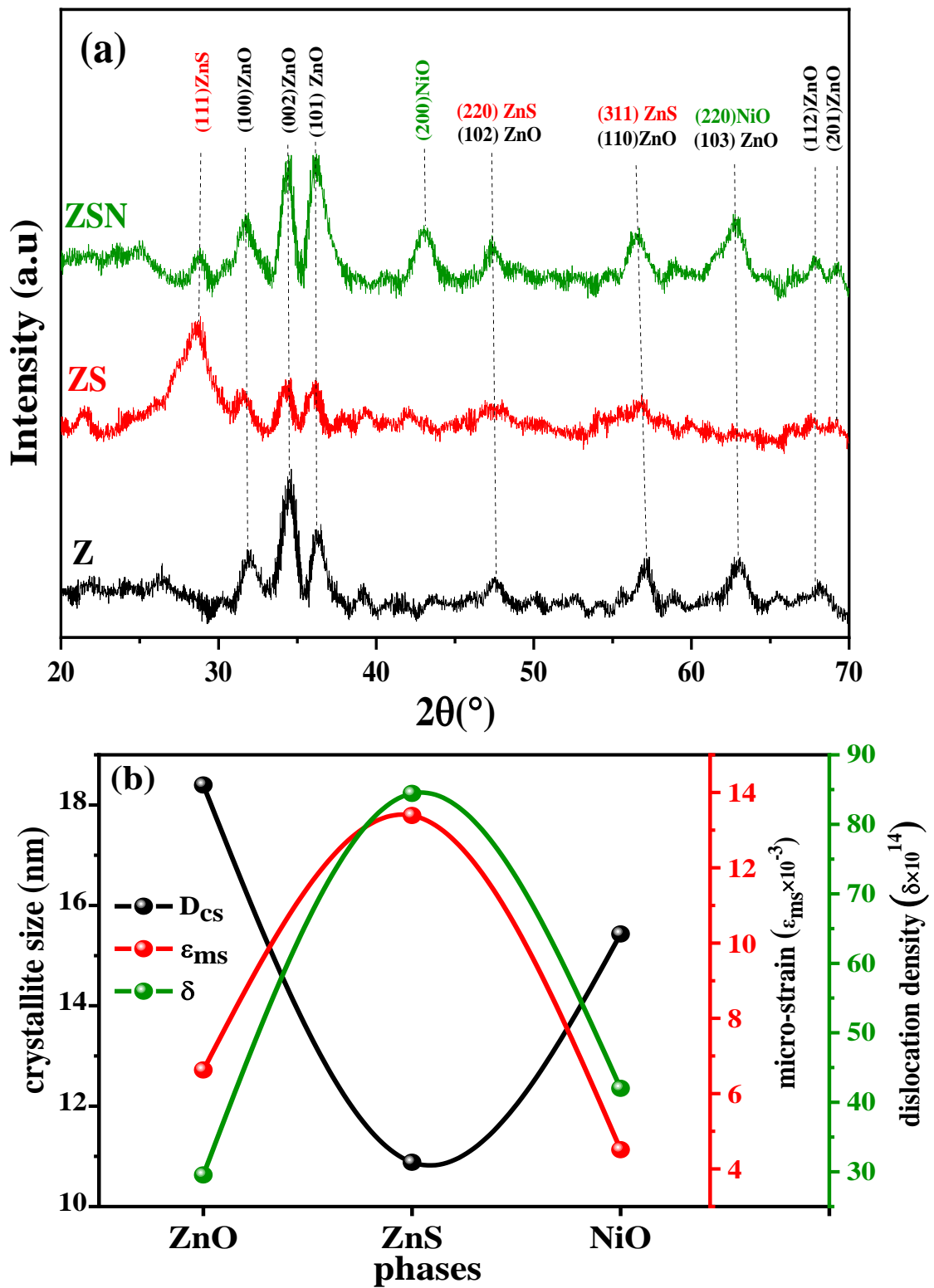


Figure IV.3: a) The XRD. of mono, multilayer samples, b) Structural parameters

IV.3.2 ATR-FTIR study

For XRD investigations, an ATR-FTIR spectrophotometer can be employed as an additional analytical technique. As seen in **Figure IV.4**, ATR investigations were carried out in the transmission mode between 400 and 4000 cm^{-1} . In the fingerprint area, metallic oxides often exhibit absorption at particular wavenumbers. In the fingerprint area, metallic oxides often show absorption at particular wavenumbers [19]. The Zn–O stretching vibration is seen in the **Z** signal layer sample at around 418, 442, 459, 523 and 552 cm^{-1} [106–109]. The bilayer **ZS** exhibited typical ZnO absorption peaks at 416, 460, and 480 cm^{-1} . Furthermore, it displays 2 additional peaks around the peak reported in the literature [114,115] at 555 and 605 cm^{-1} , which are attributed to ZnS's stretching vibration mode. The vibration peaks of the **ZSN** multilayer film were found at 416, 440, 555 and 599 cm^{-1} , where the NiO stretching mode was found [116]. Broad absorption bands returning to the glass substrates between 914 and 764 cm^{-1} were seen for all samples [110]. Notably, the FTIR results validated the XRD results.

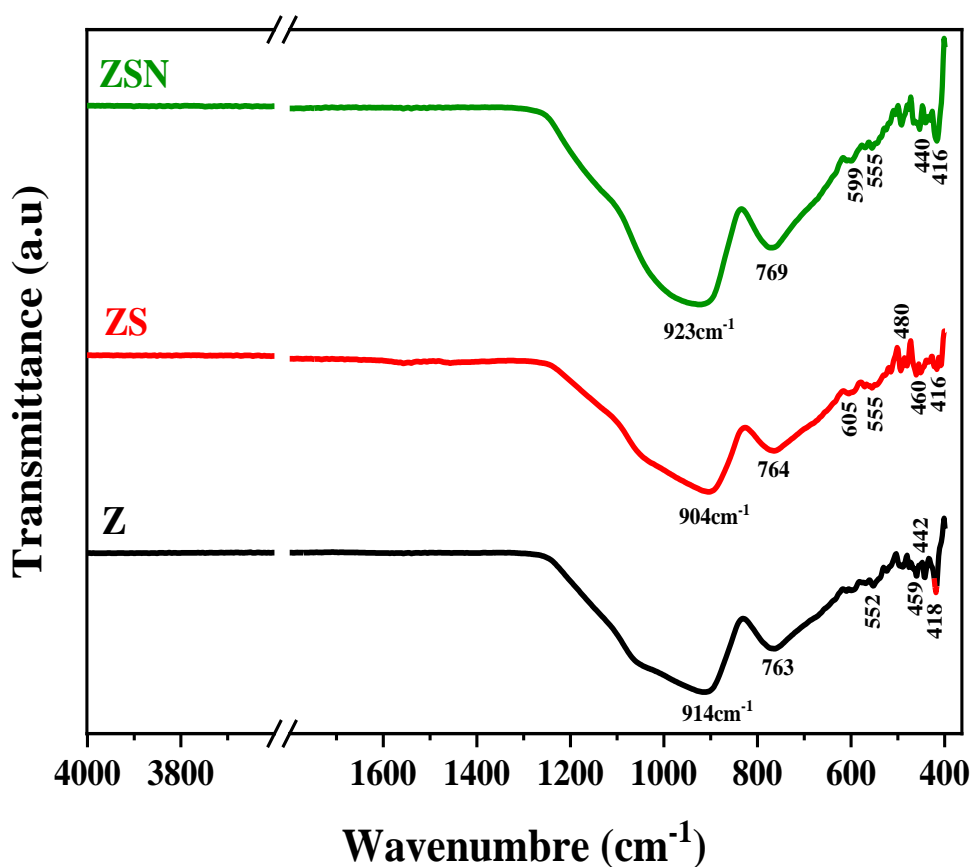


Figure IV.4: ATR-FTIR spectra of monolayer, bilayer and multilayer Samples.

IV.3.3 SEM micrographs

The surface morphologies of the deposited layers were SEM analysis, and are displayed in **Figure IV.5 (a–c)**. Significant alterations in the surface morphology were observed in the SEM micrographs, in accordance with the top layer deposition. Sol-gel ZnO:Al (**Z**)'s SEM micrograph shows an intriguing surface with a wrinkled root-like network dispersed throughout the surface that is free of cracks. The **Z** micrograph shows that these wrinkles are neither symmetrical nor have certain orientations. The quick drying that occurs after every coating layer during the deposition process causes a wrinkle-like network structure. Furthermore, X. Li et al. [99] investigated the soft and wrinkled surfaces observed in pre-annealed layers, which were slowly and rapidly annealed, respectively. The same wrinkle morphologies for pure and Al-ZnO films have been observed in other studies. [98,117,118] using the sol-gel technique. Compared with smooth thin films, these types have a larger surface-to-volume ratio. **Figure IV.5 (b)** displays the micrographs of the sprayed Zinc Sulfide on the ZnO:Al (**ZS**) at various magnifications. This demonstrates that the ZnS, due to its good cohesion with the **Z** layer, **ZS** displays a smooth and packed morphology with a disk-like form of various sizes along its surface. ZnS morphology resembling a disk was observed in Ref [97]. **Figure IV.5 (c)** displays a micrograph of the surface morphology of the upper layer of **ZSN** and NiO deposited on top of the ZnS layer. Nonuniform surface structures were observed, and the sprayed NiO precursor solution exhibited low adhesion. Low adherence was detected in the sprayed NiO film, and surface morphology was seen. Non-homogeneous overlapping was observed in the nickel oxide over the zinc sulfide layer, together with nanoparticle agglomerations with different-sized and shaped grains. In addition, the nickel oxide layer has a void and a cracked nature. The existence of nanovoids on the film morphology may influence its adherence and uniformity; nevertheless, it may also have a rough surface that allows dye adsorption in photocatalytic uses.

As shown in **Figure IV.5**, EDX was used to verify the elements of the **Z**, **ZS**, and **ZSN** films deposited on the glass substrates. To verify the existence of the peaks of coated element (Aluminum, Zinc, Nickel, Sulfide, and Oxygen), and they were found actually exist. Furthermore, because of the glass substrate, the EDX spectrum reveals the existence of (Silicon, Oxygen, and Calcium) [98] and the Gold (Au) peak that results from the Au electrical contact.

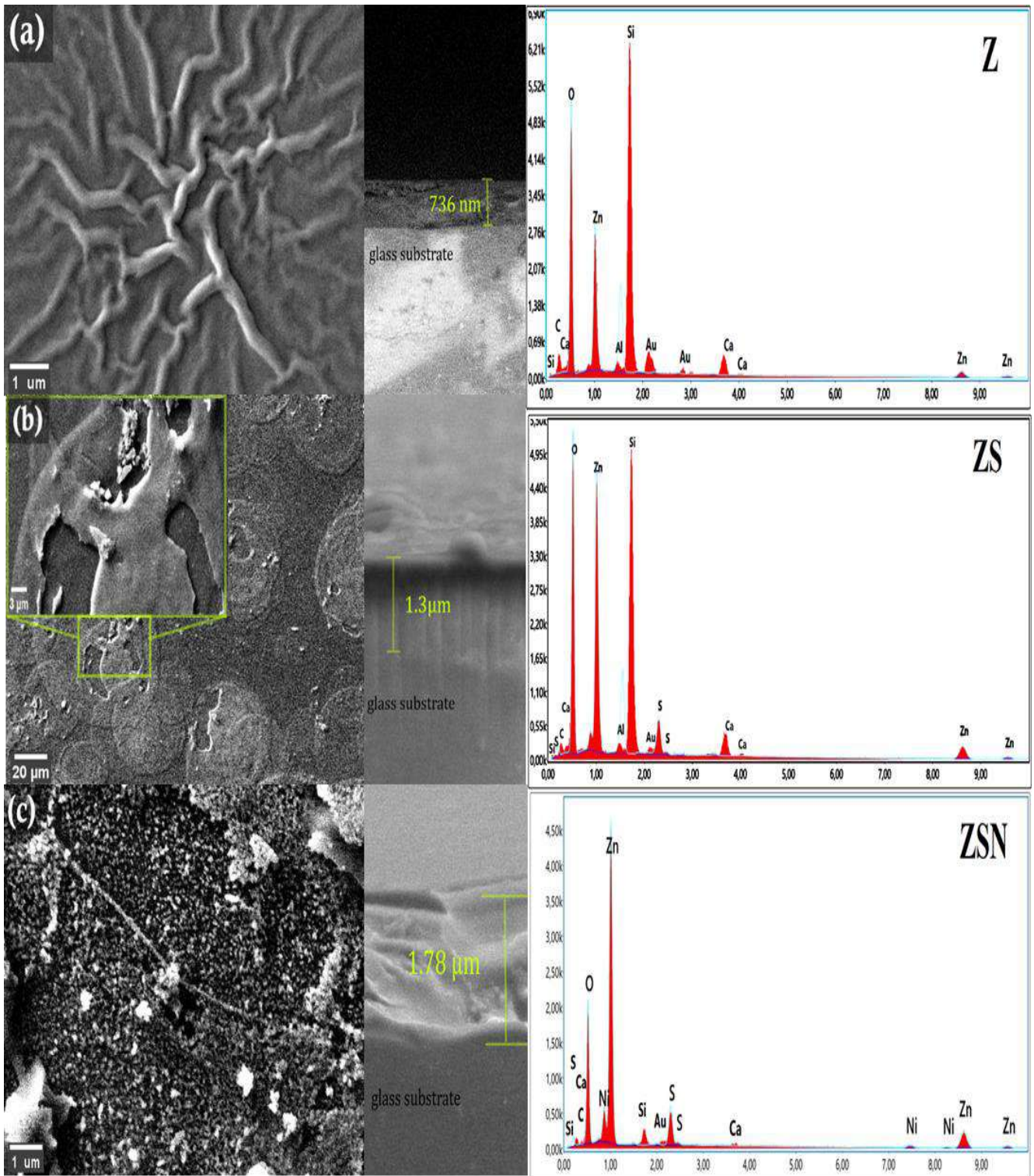


Figure IV.5: SEM micrographs with the cross-sectional and EDX of a) monolayer, b) bilayer and c) multilayer Samples.

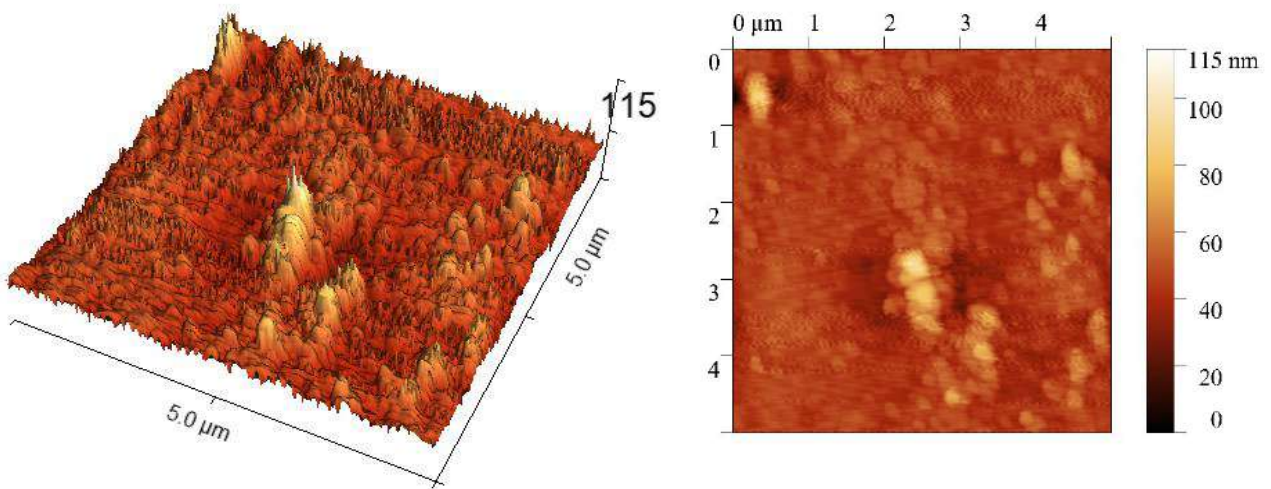
The direct measurement of the layer width of the **Z**, **ZS**, and **ZSN** films acquired by the cross-sectional micrographs is also shown in **Figure IV.5 (a-c)**, which indicates an increase in thickness from the signal- and multilayer samples. The thicknesses average of the **Z**, **ZS**, and **ZSN** layers are 736 nm, 1.3 μm , and 1.78 μm , respectively.

IV.3.4 AFM Analysis

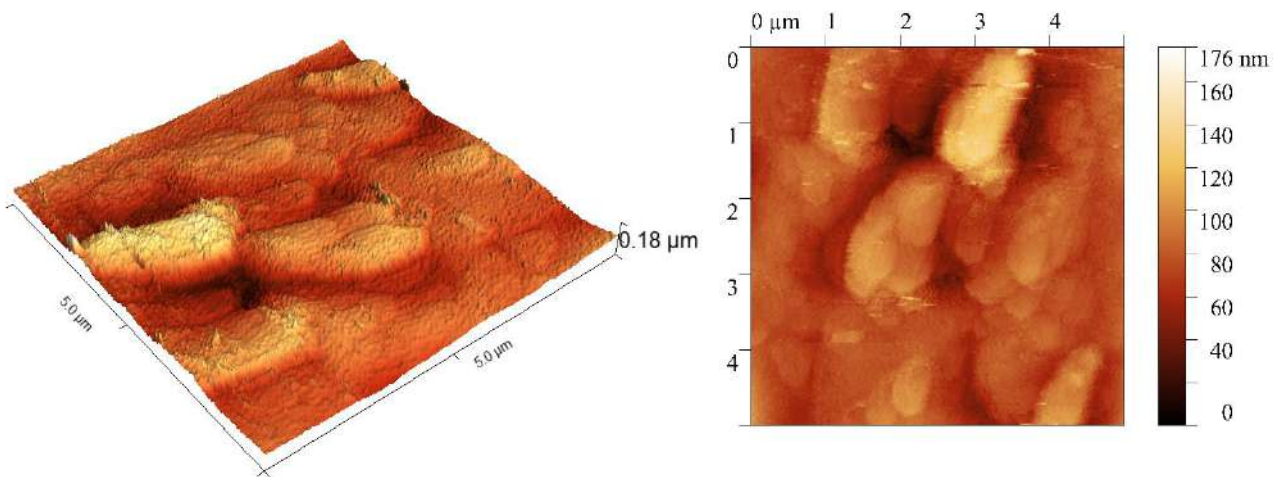
AFM analysis yielded surface topography and roughness data. Significantly, as the Scanning electron microscopy results indicate, surface roughness affects how well thin-film samples operate photocatalytically. The 2- and 3-D AFM images spanning a $5 \times 5 \mu\text{m}^2$ scanned region are shown in **Figure IV.6**. The surfaces of the samples showed agglomerations of varying sizes, as well as various surface topographies. Unlike the other films, granular forms in surface topography of the monolayer was observed (**Z**). Contrary to the earlier SEM images, which this revealed no distinct crystal grain boundaries in zones with wrinkles or smooth surfaces.

Moreover, the three dimensional **Z** film topography exhibited a granular distribution, as shown in **Figure IV.6 (a)**, with some grains aggregates growing preferentially the c-axis (perpendicular the film surface). The morphological results published by M. A. Bouacheria et al. [98] were similar to the Atomic-FM and Scanning-EM results for ZnO: doped-Al. The topography of the **ZS** layers showed thick grain aggregations covering the surface with a disk-like structure over each other to produce ellipsoidal particles with various sizes (see the 3D topography in **Figure IV.6 (b)**). **Figure IV.6 (c)** displays the NiO spraying layer on **ZS** bilayer for the trilayer **ZSN** film. It exhibits island-like grain formation development, which is a sign of nanocrystals agglomeration with some gaps between the agglomerated grains. **Table IV.1** lists the average surface root-mean-square (RMS) roughness values for each sample.

(a)



(b)



(c)

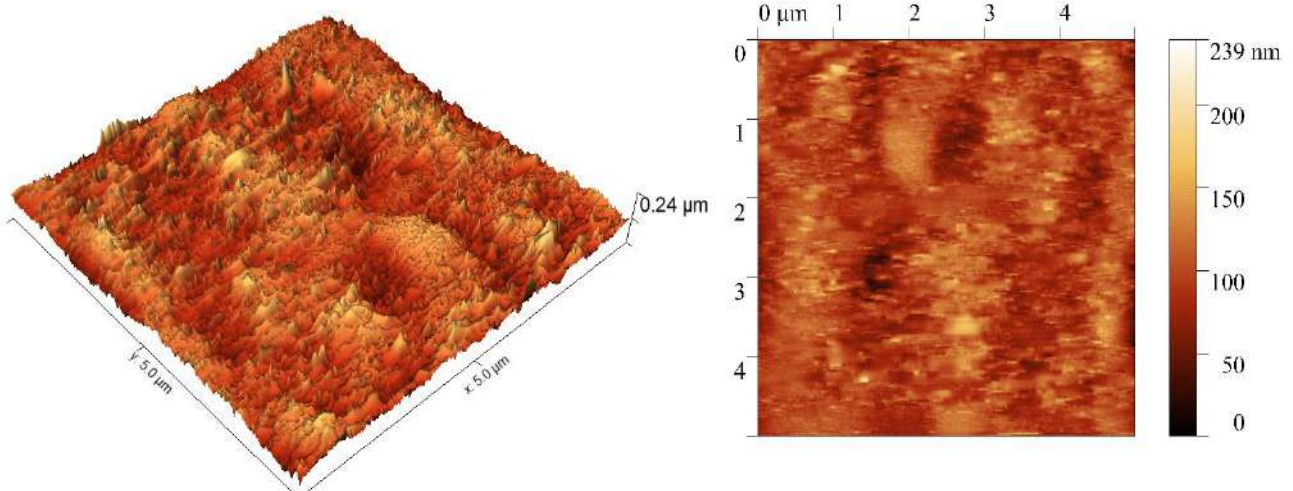


Figure IV.6: The AFM images of a) monolayer, b) bilayer and c) multilayer Samples.

IV.3.5 Optical study

The films' transmittance spectra, which were evaluated between 300 and 800 nm in wavelength, are displayed in **Figure IV.7**. The films exhibited high transmittance in the 400–700 nm visible range. In this area, ZnO:Al (**Z**) film had an average transmittance of 85%, making it extremely transparent. The aforementioned ZnS and NiO depositions, with typical values of 75% and 65%, respectively, decreased the transmittance of the film. Furthermore, **Figure IV.7 (a)** shows little variation among the **Z**, **ZS**, and **ZSN** layers in the ultraviolet region at the absorption edge. This variation moved toward shorter wavelengths at approximately 370 nm and was mostly linked to the Burstein–Moss effect [103]. Tauc equation was used to estimate the E_g of Samples.

Figure IV.7 (b) depicts the Tauc plot in the absorption edge area used to determine the optical gap values. **Figure IV.7 (b)** demonstrates that the bandgap measurements for **Z** and **ZS** were 3.26 and 3.15 eV, respectively. **Z**-film results matched findings published by other researchers [119]. Because of the hybrid band that results owing the ZnS phase being added upon ZnO, ZnO:Al/ZnS (**ZS**) displays a notable drop in its E_g value [22]. On the other hand, trilayer **ZSN** film displays two absorption band values in its direct band gap at 3.15 and 3.52 eV, respectively, which correspond to the n-ZnO/n-ZnS and n-ZnS/p-NiO junctions. A literature study [25] described an E_g finding for a core-shell n-ZnS/p-NiO junction that was comparable. This double bandgap enables absorption in various electromagnetic ranges.

The Urbach energy was also obtained by taking a linear fit (slope) by plotting $\ln(\alpha)$ vs. $h\nu$. The results obtained are 0.161 and 0.322 eV for **Z** and **ZS**, respectively, which increased with the decrease of the Optical gap (**Figure IV.7 (c)**). As the same with E_g , we estimate two values for **ZSN** film 0.312, which is associated with **ZS** the bi-layer film, and 0.357 eV for the **ZSN** tri-layer Sample. This increase can be attributed to the narrowing of the E_g (3.52 eV) of intrinsic NiO and ZnS which them in the range of 3.6–4 eV for NiO [120], of 3.54–3.72 eV for the cubic structure of ZnS [11] also because of the coupling of NiO with the zinc sulfide phase.

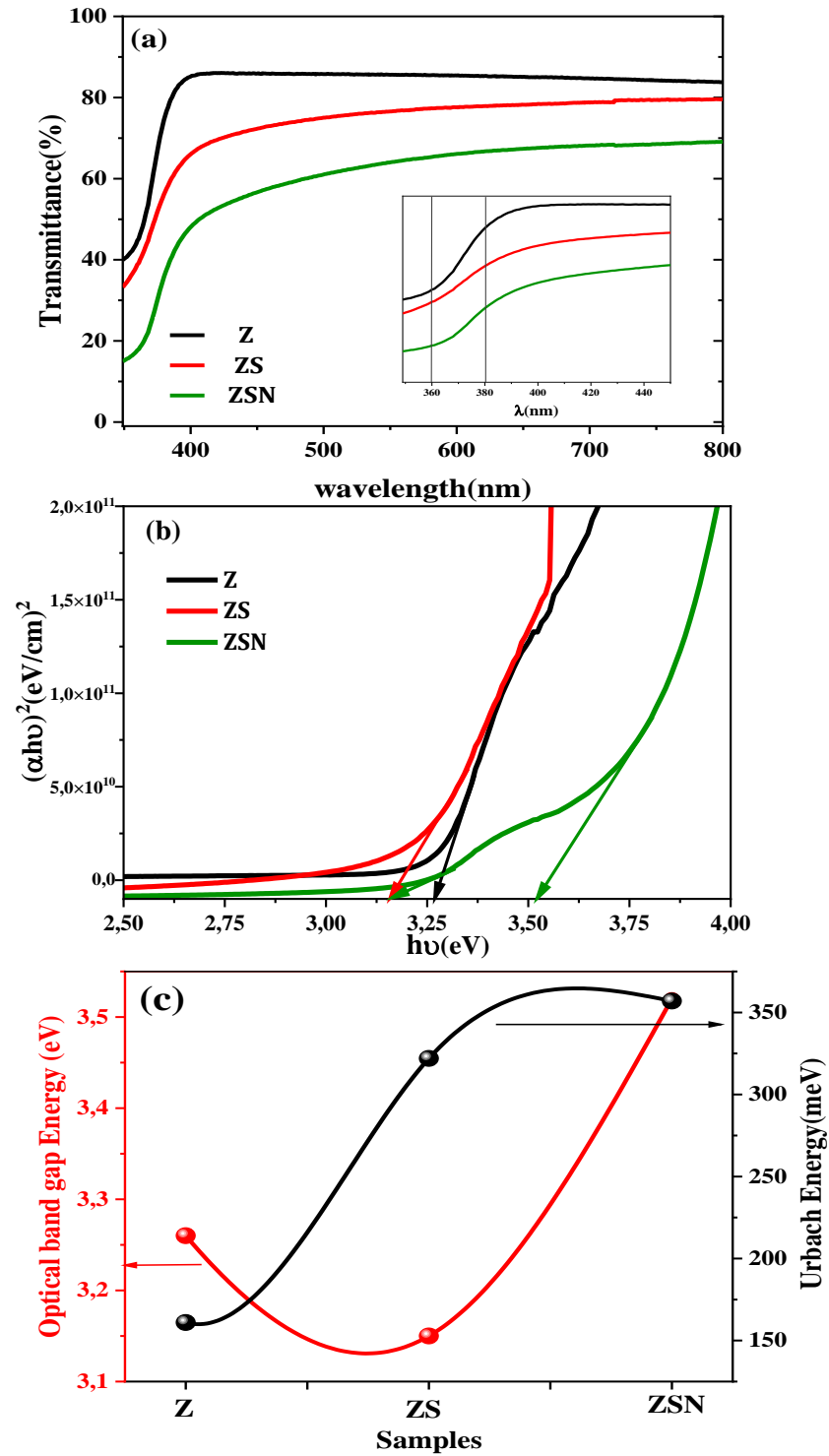


Figure IV.7: **a)** Transmittance spectra of the mono and multilayer samples (Inset display the band-edge absorption zone), **b)** Tauc plot of the mono and multilayer samples, **c)** Variation of E_g and E_u of signal and multi-layer thin films.

IV.4 Application of thin films in the photocatalytic activity

IV.4.1 Experimental protocol (Photodegradation measurement)

In order to study the photocatalytic activity, the developed films (15 cm²) were used to break down 25 ml aqueous solution of 5 mg/l MB (C₁₆H₁₈ClN₃S) dye, which is utilized as a typical dye contaminant with a pH ~ 6. The photodegradation of MB was carried on in May 2022 in Ouargla, Algeria, utilizing two distinct irradiation sources: sunshine and a 1000 W Halogen lamp exposing it as a visible light source, for 75 minutes. The samples were then immersed in a dye solution. The beaker solution was placed ~20 cm from the lamp and completely covered the films. **Figure IV.8** illustrates a schematic of the photocatalytic reactor with a visible-light lamp.

Additionally, crystal violet (CV) and Congo red (CR) dyes have been employed as pollutants under similar MB photocatalytic process conditions but just under sunlight. To reach equilibrium, dye adsorption was carried out for 30 minutes in the dark before irradiation. The photodegradation was determined by recording the dye solution absorbance (λ_{\max}). The efficiency was measured via the efficiency equation ($\eta\% = \left(\frac{C_I - C_t}{C_I}\right) \times 100 = \left(\frac{A_I - A_t}{A_I}\right) \times 100$).

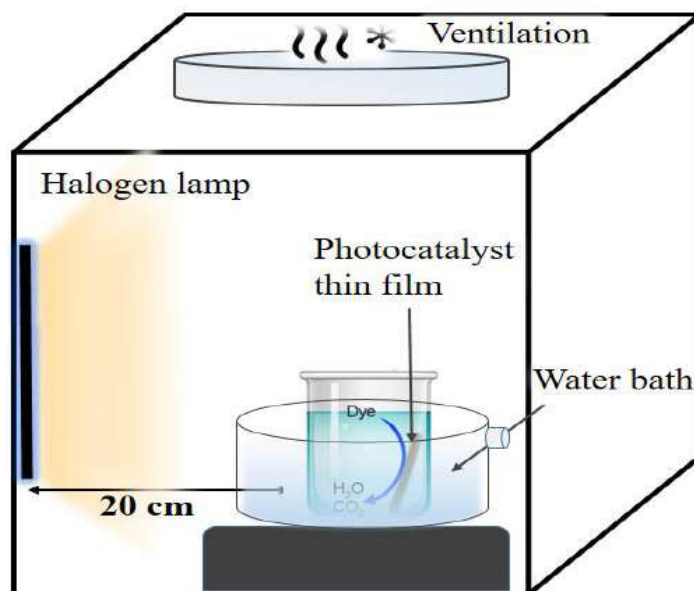


Figure IV.8: schematic of the photocatalytic reactor with a visible-light lamp.

IV.4.2 Mechanism of photodegradation behavior

Because of the trapping of $-e-h+$ pair in radiationless relaxation that might lead the SC to revert to its inactive state even after exposure to photon energy excitement [121], pure SC layers have never worked well as photocatalysts in previous studies. This reduces the photodegradation efficiency. Consequently, cationic or anionic dopants should be added to these semiconductors to increase their photodegradation activities. Extra energy levels appear in the bandgap because dopants generally occupy a variety of lattice sites, including the semiconductor's surface, lattice crystal, or interstitial sites. Additionally, by coupling these semiconductors to one another, they can form a heterojunction that significantly contributes to the reduction of e-h pairs via the hybrid bond that is formed [122]. ZnO:Al, ZnO:Al/ZnS, and ZnO:Al/ZnS/NiO (*ZSN*) samples were investigated in this work as MB photocatalysts in the presence of visible light. For the remainder of the investigation, trilayer *ZSN* was selected to examine its photocatalytic ability with the influence of pH (MB), stability/reusability (MB), with 3 organic contaminants (MB, CV, and CR), under a natural light source, as well as its decomposition mechanism (MB). Due to its twofold hybrid bandgap, visible/solar light illumination can increase the absorption efficiency of visible light for photocatalytic activities. The mechanism underlying the photocatalytic interpretation of the *ZSN* photocatalyst is proposed as illustrated in **Figure IV.9**. Under light exposure, electrons were excited from the Valence-B to the conduction-B, which will leave holes in the Valence-B of Nickel-O, Zinc-S, and Zinc-O:Al, respectively, in the studied *ZSN* trilayer sample. The electrons that are generated migrate freely via the conduction-B of zinc-O:Al to the valence-B of zinc-S. While holes are gathered in the valence-B of zinc-O:Al in the *ZSN* multilayer, the electrons produced from the conduction-B of ZnS move to the valence-B of NiO, resulting in the collection of electrons in the conduction-B of NiO. Superoxide ($\bullet\text{O}_2^-$) anion radicals were created when electrons collected on the Nickel-O surface interacted with molecules of oxygen in the surrounding air. $\bullet\text{OH}$ hydroxyl radicals were created from the oxidation of water molecules by the collected holes in the valence-B of ZnO:Al. The resultant hydroxyl radicals, $\bullet\text{OH}$ and $\bullet\text{O}^{2-}$, are strong oxidants that may efficiently attack the surrounding organic molecules and transform them into H_2O and CO_2 [24,123]. Under visible light illumination, the following oxidation process may be the mechanism of reactions for *ZSN* multilayer on organic contaminants such as MB [23,32]:

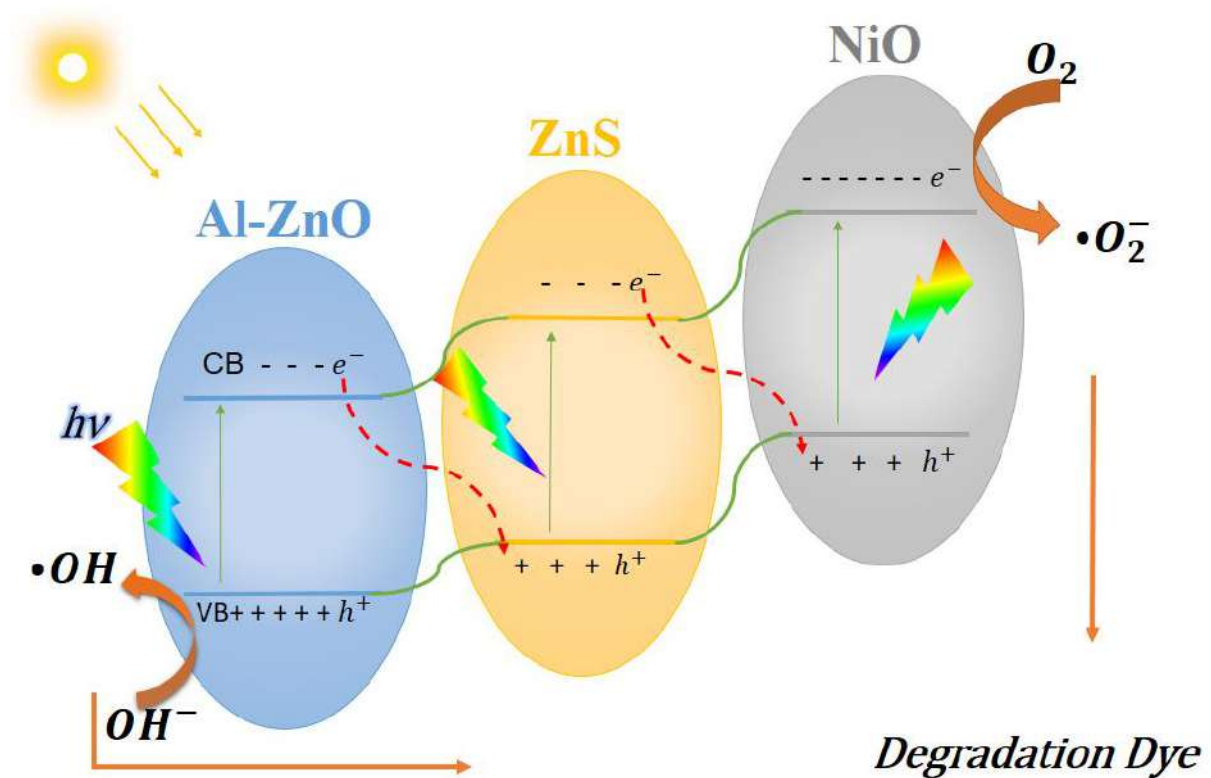
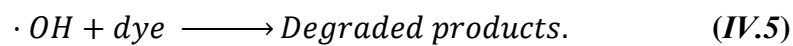
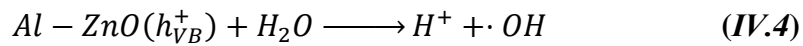
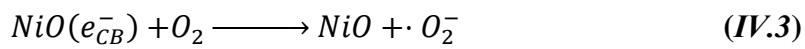
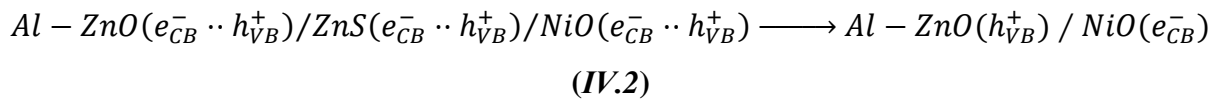
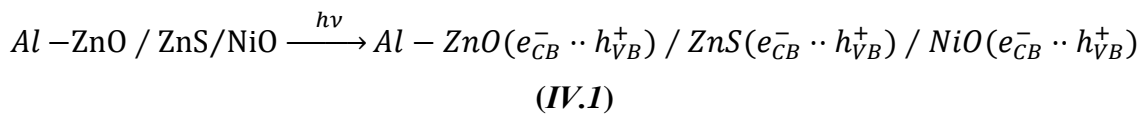


Figure IV.9: Proposed schematic photodegradation mechanism of multilayer photocatalyst under visible irradiation.

To enhance comprehension, **Figure IV.10** provides a full clarification of the possible photocatalytic decomposition pathways of MB produced during the photocatalysis operating period. Prior research has revealed that Cl⁻ ions have the potential to ionize when MB is dissolved in water [124]. In the beginning, an OH-MB molecule that has been hydroxylated may develop. This is accomplished by •OH radicals, which weaken MB compounds. In the next stage of the photocatalytic process, the MB molecules are demethylated by attacking the N-CH₃ link to generate CH₂O + H₂, followed by the generation of CO₂ and H₂O in the oxidation steps [125]. Furthermore, the C-S+=C bond can be broken by •OH radicals, producing a C-S(=O)-C bond [125], requiring the middle ring to be broken by heteroatoms of S and N. •OH radicals swap nitrogen groups to release the NH₂ radical, which then oxidizes to produce NO³⁻ ions and NH⁴⁺ cations [126]. Sulfur undergoes simultaneous hydrolysis, oxidation, and conversion to SO₄²⁻. The MB organic dye was broken down into inorganic compounds, including SO₄²⁻ and NO₃⁻ ions, water and tiny species.

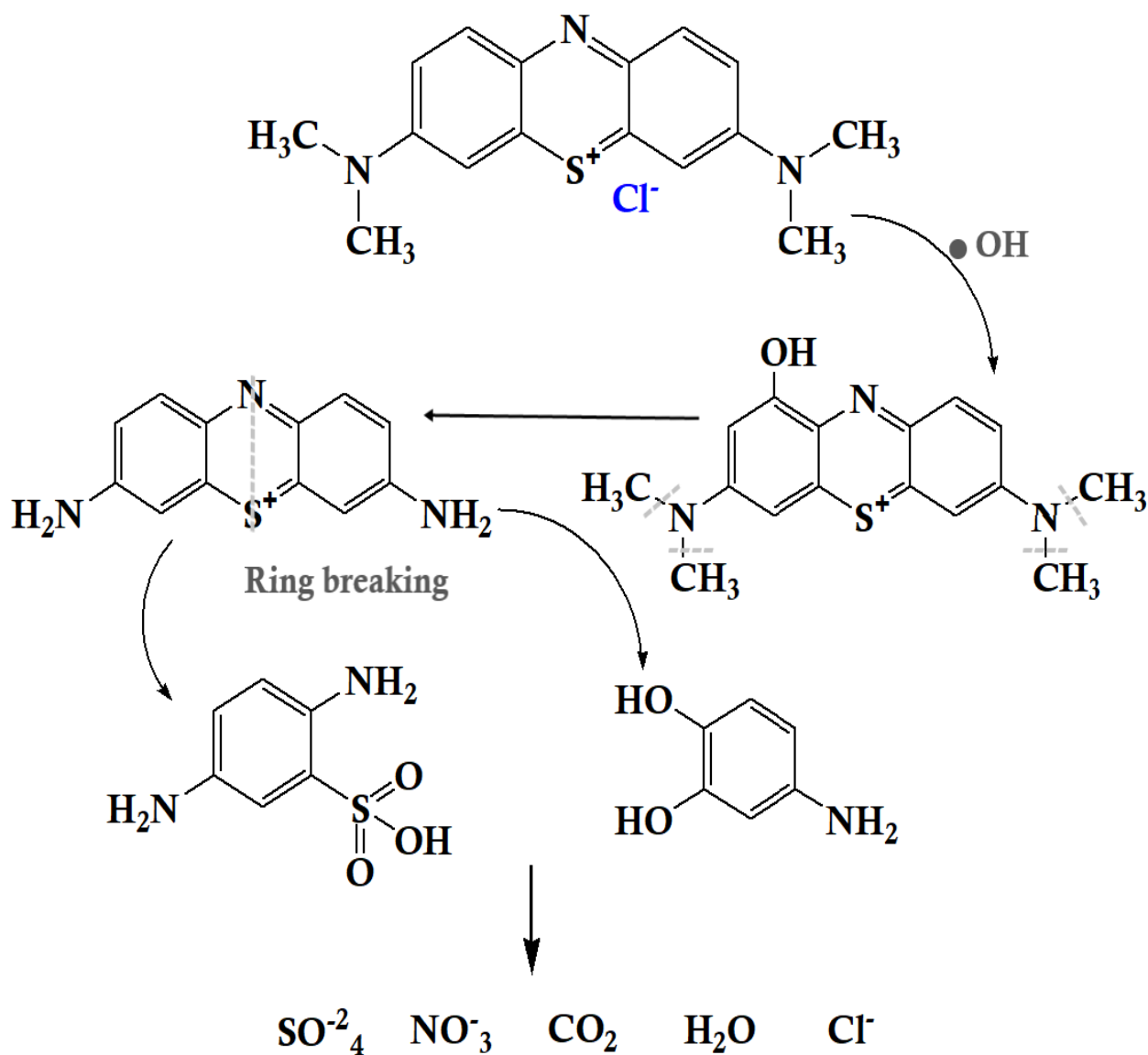


Figure IV.10: Suggested MB decomposition pathway.

IV.4.3 Photodegradation under visible light

The MB dye solution was used as an organic contaminant to study the degradation ability of the mono and multilayer deposited films. *Figure IV.11 (a)* illustrates how the dye's evolution was monitored using UV-vis absorption at the highest absorbance in the procedure time. The primary absorption peak, which corresponded to MB molecules, was found at $\lambda_{\text{max}} = 664 \text{ nm}$.

With increasing exposure time to visible-light irradiation, the rate of MB degradation increased. The photocatalytic rate ($\eta\%$) was found around 96% for the *ZSN* and $\sim 93\%$ for the *Z* and *ZS* samples, it almost completely disappeared after 50 minutes. After 75 min, the *ZSN* rate degradation efficiency enhanced to 99.81%. As may be shown in *Figure IV.11 (b)*, every sample had exceptional efficiency. However, as Zinc-O:Al and Zinc-O:Al/Zinc-S films were previously studied in earlier research, *ZSN* was selected for the remainder of the photocatalytic analysis [32,33,83]. Furthermore, the best photocatalytic performance was demonstrated by *ZSN*.

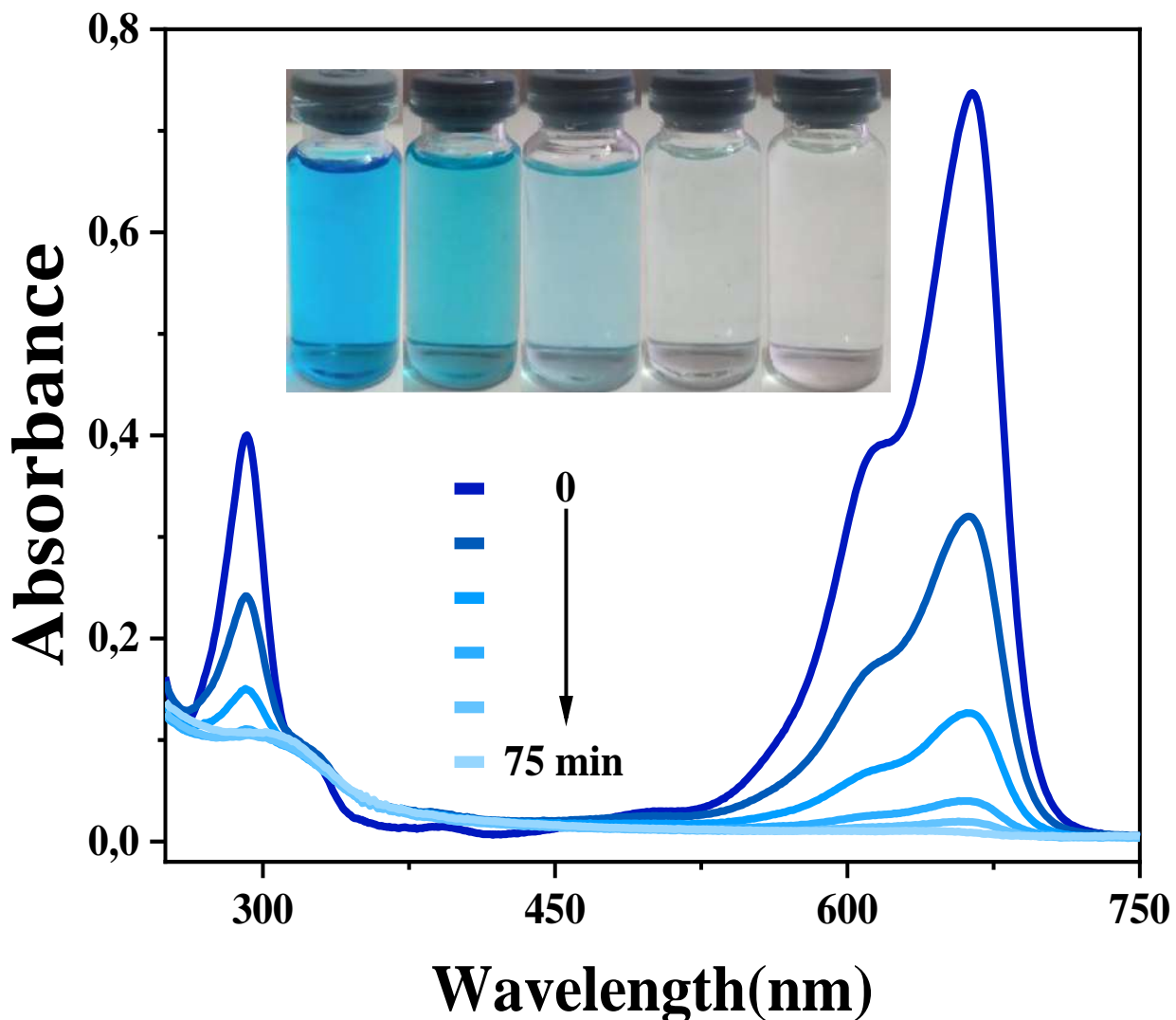


Figure IV.11: UV-visible spectra of MB solution under visible lamp.

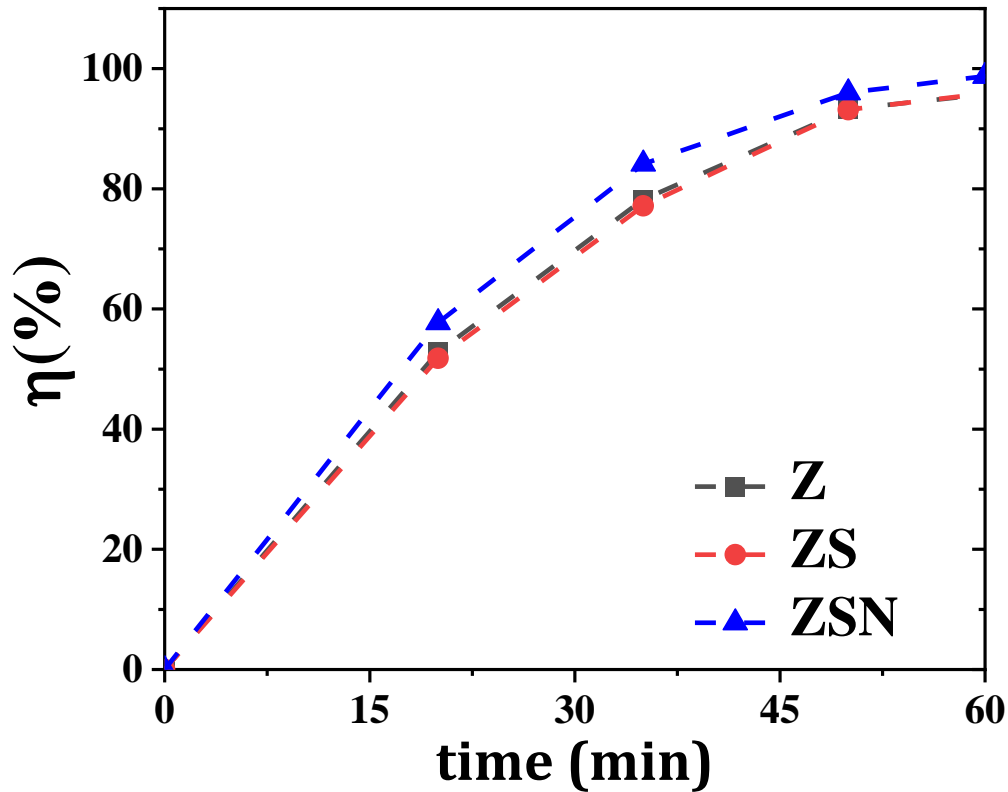


Figure IV.12: Photodegradation efficiency curves of MB with vis-irradiation using mono and multilayer photocatalysts.

The photocatalytic degradation kinetic rate constant (k) of MB dye was determined via the slopes of the plots of $\ln(C_t/C_0)$ vs. irradiation time (**Figure IV.13**), employing the first-order model from Eq. **IV.6** [26]:

$$\ln \frac{C_0}{C_t} = kt \quad (\text{IV.6})$$

where the beginning concentration, the dye concentration during the process, and the rate constant are denoted, respectively, by C_0 , C_t , and k . The correlation coefficients were $R^2 \sim 0.94$ and 0.97 for the **Z** and **ZSN**, respectively, k values have been found to be 0.06844 min^{-1} for the **Z** and 0.07638 min^{-1} for the **ZSN**. The **ZSN** trilayer thin film had a greater R^2 and k degradation rate, indicating its improved discoloration ability.

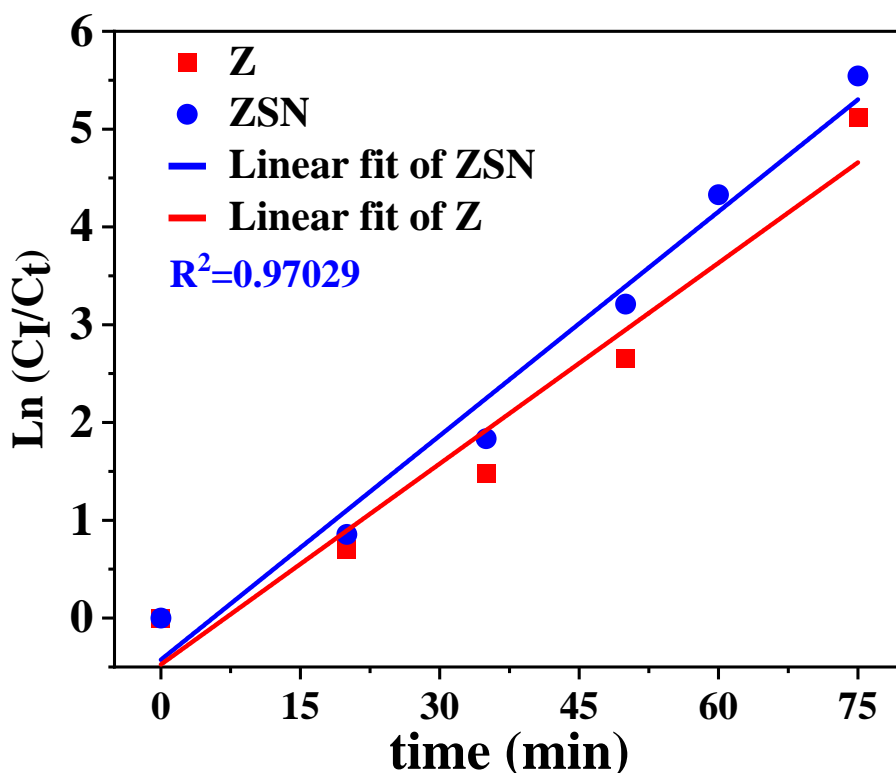


Figure IV.13: Photodegradation kinetics of MB by Z and ZSN as catalysts.

✚ The stability and reusability of the ZSN photocatalyst for MB degradation under visible irradiation for 50 minutes are shown in **Figure IV.11 (d)**. After five iterations of the experiment, the photocatalytic performance slightly decreased with each iteration, reaching about 90% decomposition toward the end. This demonstrates clearly that the photodegradation of MB was slightly decreased (~6%), that is thought to offer real-time, long-term stability for useful industrial photocatalytic applications. As a result, the ZSN photocatalyst sample under investigation showed a high stability against MB.

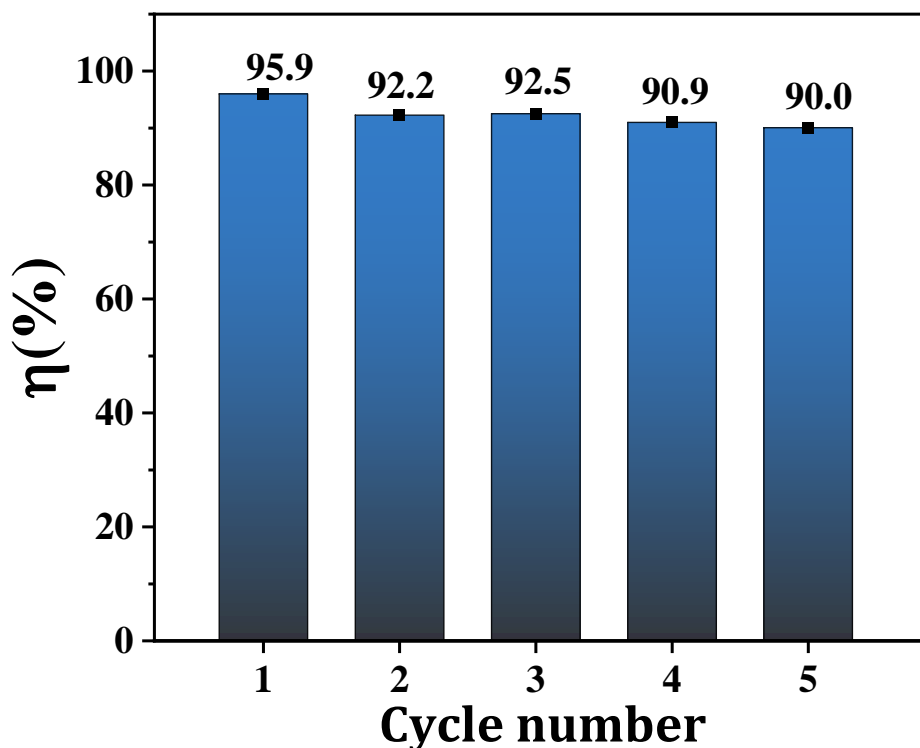


Figure IV.14: Recyclability of ZSN photocatalyst with MB under visible illumination.

IV.4.4 pH Effect

Solution pH plays a significant role in the photocatalytic procedure[127] because it manages interactions in the degradation time of organic pollutants [128]. Thus, the pH must be optimized to achieve the best degradation efficiency. All tests used the ZSN multilayer in 60 min under vis-light to assess the impact of pH on dye degradation. **Figure IV.15** illustrates how NaOH and HCl modify the pH values. This indicates clearly that dye degradation slowed at lower pH values. The photodegradation rate of the ZSN improved when the pH of the MB solution was raised from six. Under vis-irradiation, the MB degradation value was greater in the pH range of 6–10 than it was at acidic pH=two. The sample showed greater photodegradation performance in the intermediate and alkaline regions as compared to the basic, neutral, and acidic regions. This might be related to the higher availability of OH⁻ ions compared to the acidic medium as well as the creation of more OH radicals by combining with holes (h⁺) produced by the radiation-excited electronic (e⁻) catalyst. Additionally, this can be related to the cationic nature of the MB dye [76].

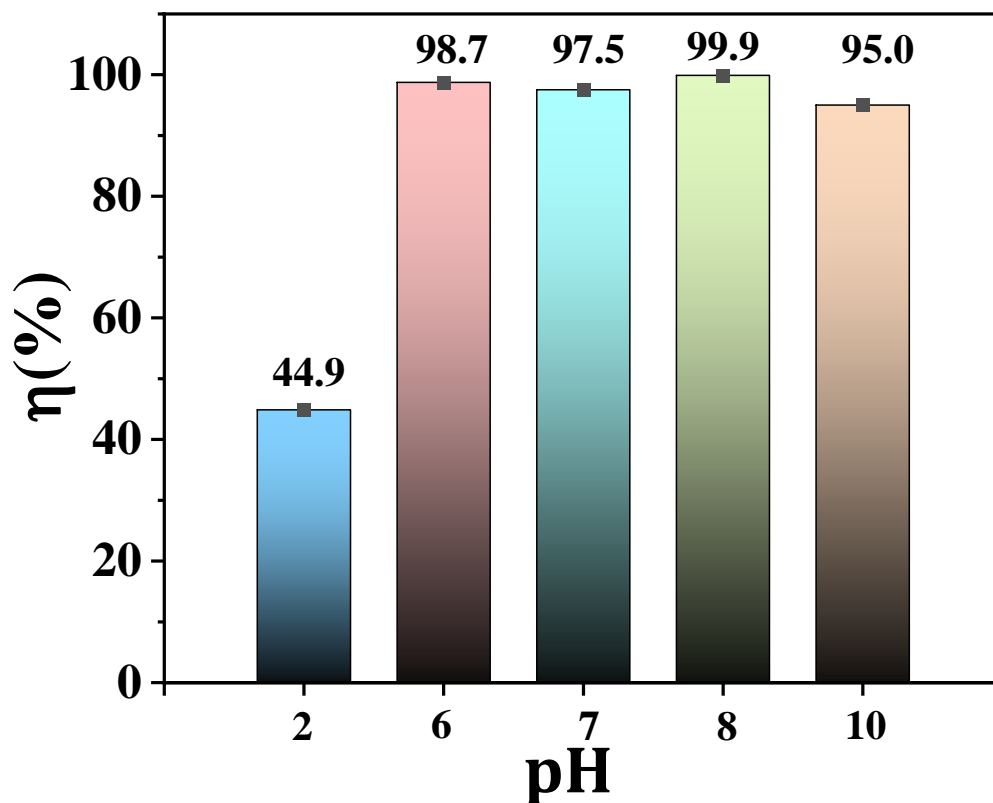


Figure IV.15: The photodegradation efficiencies of various pH levels.

IV.4.5 Photodegradation efficiency under natural irradiation

MB, CV, and CR pollutants were chosen as targets for the second photodegradation operation step to evaluate their capacity for photodegradation under natural light. Furthermore, the dyes' maximum absorbance was measured throughout the visible range; *Figure IV.16*, illustrates this; the MB, CV and CR organic dyes were found to have the highest absorbances at $\lambda = 664, 583,$ and 498 nm, respectively. A variation in the maximum absorbance was noted to determine the rate of photocatalytic efficiency.

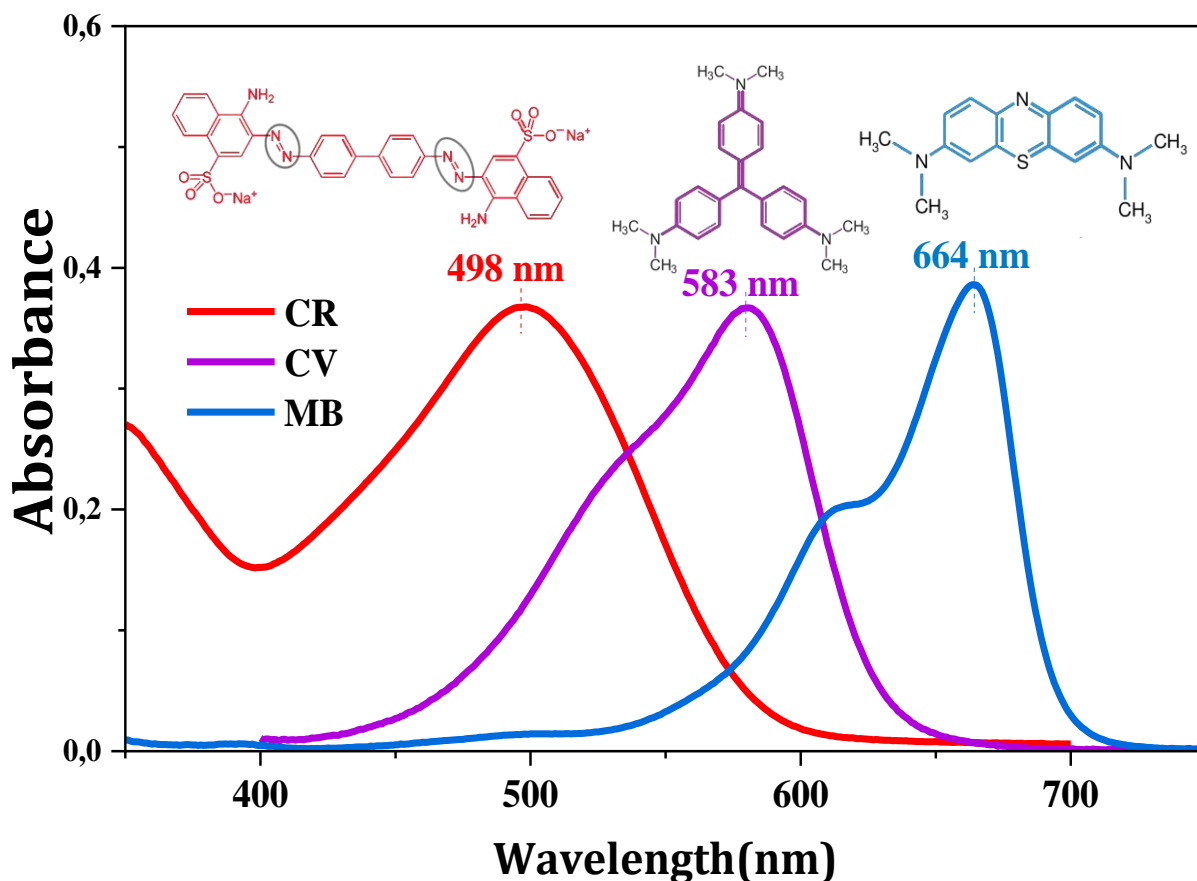


Figure IV.16: CR, CV, and MB UV-visible absorbance spectra.

Similar conditions were employed in the initial step during the photocatalytic studies under visible light. The UV-vis spectra **Figure IV.17 (a-c)** and degradation percentage (**Figure IV.17 (d)**) of the 3 dyes are displayed. For all three organic dyes, the absorption maxima at λ_{\max} gradually diminished with time. It was found that the photocatalytic efficiencies for MB, CV, and CR were 90%, 85%, and 65%, respectively, over the 90-minute illumination period under solar radiation, and that for MB, the rate was 83% in just 60 min. CR is a more challenging decomposition dye than MB or CV. This is explained by the fact that their structure contains a large number of benzene rings in addition to two azo bonds (N=N), each of which has a high bond energy of 4.33 eV [26,125]. This accounts for the relatively poor rate efficiency of only 75.76% over 4 hours of exposure to solar radiation, as opposed to 1.5 hours at $\eta=65\%$. Even at the lowest value in this instance, the first-order kinetic value (k) of CR was 0.00425 min^{-1} with a small correlation coefficient ($R^2=0.63$). **Table IV.2** lists the kinetic rates (K) and R^2 values.

Table IV.2: $\eta\%$, time, k , and R^2 values of mono and multilayer of photocatalytic degradation performance.

<i>Sample</i>	<i>pollutant</i>	<i>light source</i>	<i>rate constant, K (min^{-1})</i>	<i>R^2 value %</i>	<i>$\eta(\%)$</i>	<i>t (min)</i>
ZSN	methylene Blue	Visible	0.0764	97	95.99	50
Z			0.0684	93	93.26	
ZS			0.0523	94	93.16	
ZSN	MB	sunlight	0.0259	98	90.12	90
ZSN	CV		0.0106	96	85.48	
ZSN	CR		0.0043	63	65.42	

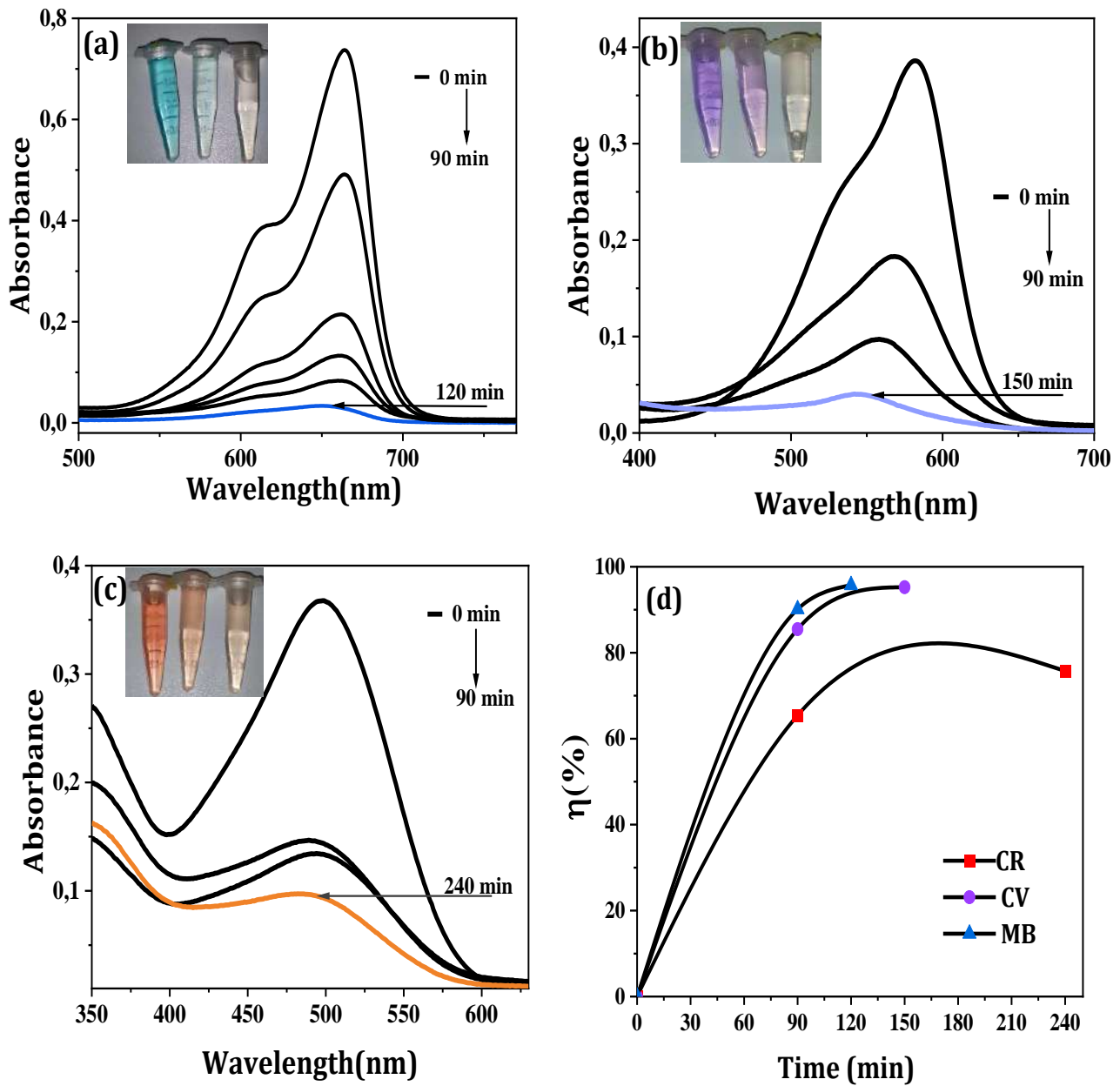


Figure IV.17: a-c) UV-vis curves of a) MB, b) CV, and c) CR under sunlight using ZSN photocatalyst sample, d) Degradation rate of dyes under sunlight using ZSN photocatalyst sample.

Chapter IV. Doped and Coupled ZnO for Enhancing Photocatalytic Activity

Table IV.3: Reported degradation efficiency of coupled ZnO photocatalysts against methylene blue (MB) in literature.

<i>Photocatalyst</i>	<i>Synthesis method</i>	<i>Light source</i>	<i>Dye amount</i>	<i>Catalyst dose</i>	η for MB/ <i>time</i>	<i>Year Ref</i>
ZnO/AZO/ZnO multilayer thin films	on glass substrates by spin coating	visible light 750-W lamp	30 mg/L 40 mL	thin films (24 cm ²)	95.2%/ 180min	2019 [5]
ZnO/ZnS nanoarrays	on Ni foam substrate by hydrothermal	both 300 W UV & 180 W ultrasonic sonication	5 mg/L 50 mL	thin film	53.8%/50min	2021 [22]
Al-ZnO/ZnS	ultrasonic sol-gel	100 W mercury lamp	10mL MB in 10mL DW	1mg	98%/ 60 min	2019 [33]
ZnO:Al/ZnS multilayer	sol-gel & spray pyrolysis	visible light halogen lamp	10 ⁻⁵ M 25mL	thin films (13.5cm ²)	93%/ 50 min	this work
CdS/ZnO thin films	on FTO substrate using SILAR	sunlight	20 mg/L 20mL	thin films (9cm ²)	91%/240 min	2018 [129]
NiO-CdS nanocomposites	chemical method	simulated sunlight lamp (Ultra-Vitaulux, 300 W, Osram)	3mg/ 300mL 70 mL	0.03g	95%/120 min	2022 [15]
ZnO/ZnS/g-C₃N₄	thermal decomposition, chemical precipitation	300W simulated solar light lamp	10 mg/L		up to 75%/ 60 min	2018 [16]
ZnO:Al/ZnS/NiO multilayer	sol-gel & spray pyrolysis	visible light halogen light	10 ⁻⁵ M 25mL	thin films (13.5cm ²)	~96%/ 50 min & 99,8%/75 min	this work
ZnO:Al/ZnS/NiO multilayer	sol-gel & spray pyrolysis	sunlight	10 ⁻⁵ M 25mL	thin films (13.5cm ²)	90%/ 90 min	this work

IV.5 Conclusions

This study presented an easy and cost-effective methods involving spin coating and spray pyrolysis techniques for producing Al-doped Zinc-O and then coated by Zinc-S and then by Nickel-O as upper layers to get Al-ZnO, Al-ZnO/ZnS, and Al-ZnO/ZnS/NiO multilayer samples and studied their structural, morphological, optical and photocatalytic properties. The successfully prepared films were confirmed by XRD and additional FTIR analyses, which revealed the characteristic presence of only Zinc-O, Zinc-S, and Nickel-O phases in the system of the obtained films. This indicates that the hexagonal wurtzite structure has a preferential orientation along the (002) plane in the Al-ZnO signal layer and that the bilayer Al-ZnO/ZnS is responsible for shifting the most intense peak for the typical cubic ZnS structure. Additionally, the multilayer Al-ZnO/ZnS/NiO exhibited an additional peak related to NiO. Further, morphological SEM analysis revealed that while for photocatalyst samples, AFM shows beneficial surface roughness, which causes it to be greater than the smoothed volume ratio; the increase of different phase layer coats on top of one another deteriorates the density and adhesion of the topmost layer, thereby impacting its uniformity network structure. The sample included an Al trace, as shown in the EDX mapping study. According to reports on the optical properties of thin films, Al-ZnO films have a high transparency of 85%, but the Al-ZnO/ZnS/NiO multilayer has a low average transmittance of 65% and substantial absorption properties. Furthermore, the UV-visible absorption revealed that linking Al-ZnO/ZnS reduces the band gap of Al-ZnO (3.26 eV) to 3.15 eV, whereas Al-ZnO/ZnS/NiO shows extra absorption values (3.52 eV) because of the NiO layer. With very little observable reduction after the fifth cycle, the obtained findings show that Al-ZnO/ZnS/NiO displays a high degradation rate (~96%) against MB within 50 min under vis-light, enhancing its stability and reusability in real-time industrial applications. Additionally, when solar radiation, a free, renewable energy source, was used instead of visible light, the photocatalytic activities of Al-ZnO/ZnS/NiO demonstrated a sufficient degradation rate against MB, CV and CR, which were 90%, 85% and 65%, respectively. This study is expected to pave the way for low-cost synthesis of doped and linked metal oxides as multilayer thin films, resulting in more stable and rough photocatalyst capabilities and more absorption bands for effective water treatment applications.

Conclusion and Outlook

In this thesis, we were interested in the preparation of deposits of thin layers of pure, doped, and Co-doped ZnO and coupled ZnO (multilayer) on glass substrates by chemical methods. To study the effectiveness of metal oxide thin-film semiconductor applications, particularly their function in photocatalytic activity applications.

We used an easy and simple chemical method called spray pyrolysis to prepare thin layers of pure and doped ZnO. Can be used to easily obtain nanocrystalline thin films. No annealing temperature was required after the deposition, and the films were neither amorphous nor of poor quality. Thin layers of doped ZnO were coupled with other metal sulfide and oxide phases (ZnS and NiO). The film-doped ZnO was coated using the sol-gel spin coating technique. The samples were then dried to remove solvents, and the entire process, from coating to drying, was carried out six times. The prepared thin films were subsequently subjected to a heat treatment by annealing at 500 °C.

The resulting films were characterized by XRD, FTIR, SEM/EDS, AFM and UV-vis spectroscopy. The SEM results revealed uniform nanostructure films with small spherical shapes and aggregates in undoped and Al-doped ZnO and slight variations in diameter for (Al, Ni) co-doped ZnO for the spread samples. Moreover, SEM analysis of the multilayer samples indicated that the deposition of different nanocrystalline films above one another could deteriorate the adherence of the upper layer, which can influence its homogenous shapes. XRD and FTIR analyses confirmed the growth of the deposited phases of the crystalline thin films. In addition, EDS mapping analysis demonstrated the existence of the deposited materials, particularly dopants that are difficult to detect by other analyses. The optical characteristics of thin films have been reported in high-transmittance films in the visible region, which can be decreased by the addition of layers to multilayer films.

First, the sprayed thin films of undoped and doped Zinc-O were tested for photocatalysis against MB under UV light irradiation. Nevertheless, its opposite effect is due to Al, which increases E_g from 3.22 to 3.28 eV.

On the other hand, the multilayer thin films were elaborated for the first time to enhance the photocatalytic degradation rate of MB organic dye under visible light irradiation. The photodegradation was studied at different time intervals (0–75 min). It exhibited a high photocatalytic rate (~96%) against MB in 50 minutes under visible irradiation, investigating its

Conclusion and Outlook

stability and reusability, with only a slight decrease seen beyond the fifth cycle, which is thought to offer real-time, long-term stability for useful industrial photocatalytic uses. ZnO:Al/ZnS/NiO multilayer sample was used for the photocatalytic degradation under sunlight irradiation. Their photocatalytic activity was evaluated using three dyes, which showed good degradation rates under 90 min of irradiation.

This study also demonstrated the mechanism steps of multilayer photocatalysts and suggested the MB degradation pathway.

The results obtained at the end of this study turned out to be interesting both in terms of investigation and perspectives. Thus, the results confirm the real possibilities offered by nanocomposite films in the field of technical applications in general and photodegradation applications.

There are many prospects as this work continues in several directions, for example, by applying deposited ZnO/ZnS/NiO films to the photodegradation of several other dyes with the possibility of adding other chemical constituents, such as H₂O₂, to accelerate the reaction degradation. This thesis suggests opening the door for cost-effective synthesis of doped and coupled multilayer thin films to obtain more absorption bands and rough and stable photocatalyst properties for efficient water treatment applications using sunlight, particularly Ouargla sunlight, which has been investigated in several studies.

References

- [1] M.R. Khanlary, S. Tarzi, Study of structural, optical and morphological properties of ZnO/ZnS heterostructures deposited by spray pyrolysis method, *Opt. Quantum Electron.* 53 (2021) 1–10. <https://doi.org/10.1007/s11082-020-02657-2>.
- [2] M. Salah, W. Zayani, B. Bouricha, S. Azizi, A. Alatrache, M. Amlouk, J. Lamloumi, Vibrational study of Li-doped ZnO sprayed thin films along with sensors under ethanol vapor and photocatalytic applications, *J. Mater. Sci. Mater. Electron.* 31 (2020) 18883–18902. <https://doi.org/10.1007/s10854-020-04426-z>.
- [3] D. Saravanakumar, S. Sivaranjani, K. Kaviyarasu, A. Ayeshamariam, B. Ravikumar, S. Pandiarajan, C. Veeralakshmi, M. Jayachandran, M. Maaza, Synthesis and characterization of ZnO-CuO nanocomposites powder by modified perfume spray pyrolysis method and its antimicrobial investigation, *J. Semicond.* 39 (2018). <https://doi.org/10.1088/1674-4926/39/3/033001>.
- [4] N. Talebian, M. Douidi, H. Mogoei, Antibacterial activities of sol-gel derived ZnO-multilayered thin films: p-NiO heterojunction layer effect, *J. Sol-Gel Sci. Technol.* 74 (2015) 650–660. <https://doi.org/10.1007/s10971-015-3644-1>.
- [5] M. Baradaran, F.E. Ghodsi, C. Bittencourt, E. Llobet, The role of Al concentration on improving the photocatalytic performance of nanostructured ZnO/ZnO:Al/ZnO multilayer thin films, *J. Alloys Compd.* 788 (2019) 289–301. <https://doi.org/10.1016/j.jallcom.2019.02.184>.
- [6] M.A.M. Ahmed, W.E. Meyer, J.M. Nel, Effect of (Ce, Al) co-doped ZnO thin films on the Schottky diode properties fabricated using the sol-gel spin coating, *Mater. Sci. Semicond. Process.* 103 (2019). <https://doi.org/10.1016/j.mssp.2019.104612>.
- [7] R. Barir, B. Benhaoua, S. Benhamida, A. Rahal, T. Sahraoui, R. Gheriani, Effect of Precursor Concentration on Structural Optical and Electrical Properties of NiO Thin Films Prepared by Spray Pyrolysis, *J. Nanomater.* 2017 (2017). <https://doi.org/10.1155/2017/5204639>.
- [8] O.A. Ali, M.A. Hameed, Q.G. Al-Zaidi, Electrical Properties of Pure NiO and NiO:Ag Thin Films Prepared by Pulsed Laser Deposition, *Trans. Indian Natl. Acad. Eng.* 5 (2020) 27–31. <https://doi.org/10.1007/s41403-020-00086-x>.

References

- [9] D. Aouf, A. Henni, D. Selloum, Y. Khane, F. Fenniche, D. Zerrouki, H. Belkhalifa, N. Dizge, Facile preparation and characterization of nanostructured ZnS/PbS heterojunction thin films for enhanced microbial inhibition and photocatalytic degradation, *Mater. Chem. Phys.* 295 (2023) 127059. <https://doi.org/10.1016/j.matchemphys.2022.127059>.
- [10] G.Y. Shaikh, D.S. Nilegave, S.S. Girawale, K.B. Kore, S.R. Newaskar, S.A. Sahu, A.M. Funde, Structural, Optical, Photoelectrochemical, and Electronic Properties of the Photocathode CuS and the Efficient CuS/CdS Heterojunction, *ACS Omega*. 7 (2022) 30233–30240. <https://doi.org/10.1021/acsomega.2c03352>.
- [11] H. Benamra, H. Saidi, A. Attaf, M.S. Aida, A. Derbali, N. Attaf, Physical properties of Al-doped ZnS thin films prepared by ultrasonic spray technique, *Surfaces and Interfaces*. 21 (2020). <https://doi.org/10.1016/j.surfin.2020.100645>.
- [12] R.S. Pedanekar, S.K. Shaikh, K.Y. Rajpure, Thin film photocatalysis for environmental remediation: A status review, *Curr. Appl. Phys.* 20 (2020) 931–952. <https://doi.org/10.1016/j.cap.2020.04.006>.
- [13] A. Arfaoui, A. Mhamdi, Physical investigations and photocatalytic activity test of NiMoO₄ thin films prepared by spray pyrolysis technique, *Bull. Mater. Sci.* 45 (2022). <https://doi.org/10.1007/s12034-022-02723-3>.
- [14] M. Adeel, M. Saeed, I. Khan, M. Muneer, N. Akram, Synthesis and Characterization of Co-ZnO and Evaluation of Its Photocatalytic Activity for Photodegradation of Methyl Orange, *ACS Omega*. 6 (2021) 1426–1435. <https://doi.org/10.1021/acsomega.0c05092>.
- [15] S.K. Sharma, M.P.C. Kalita, Microstructure analysis of NiO nanocrystals and enhanced photocatalytic activities of NiO-CdS nanocomposites, *J. Mater. Sci. Mater. Electron.* 33 (2022) 7824–7837. <https://doi.org/10.1007/s10854-022-07934-2>.
- [16] Z. Dong, Y. Wu, N. Thirugnanam, G. Li, Double Z-scheme ZnO/ZnS/g-C₃N₄ ternary structure for efficient photocatalytic H₂ production, *Appl. Surf. Sci.* 430 (2018) 293–300. <https://doi.org/10.1016/j.apsusc.2017.07.186>.
- [17] B. Al Farsi, F. Al Marzouqi, M. Al-Maashani, M.T. Souier, M. Tay Zar Myint, M.Z. Al-Abri, Rapid microwave-assisted fabrication of Al-doped zinc oxide nanorods on a

References

- glass substrate for photocatalytic degradation of phenol under visible light irradiation, *Mater. Sci. Eng. B Solid-State Mater. Adv. Technol.* 264 (2021).
<https://doi.org/10.1016/j.mseb.2020.114977>.
- [18] A. Sadollahkhani, I. Kazeminezhad, J. Lu, O. Nur, L. Hultman, M. Willander, Synthesis, structural characterization and photocatalytic application of ZnO@ZnS core-shell nanoparticles, *RSC Adv.* 4 (2014) 36940–36950.
<https://doi.org/10.1039/c4ra05247a>.
- [19] S. Ben Ameer, H. BelHadjltaief, B. Duponchel, G. Leroy, M. Amlouk, H. Guermazi, S. Guermazi, Enhanced photocatalytic activity against crystal violet dye of Co and In doped ZnO thin films grown on PEI flexible substrate under UV and sunlight irradiations, *Heliyon.* 5 (2019). <https://doi.org/10.1016/j.heliyon.2019.e01912>.
- [20] S.C. Bulakhe, R.J. Deokate, Electrochemically prepared Fe: NiO thin film catalysis for oxygen evolution reaction, *J. Mater. Sci. Mater. Electron.* 33 (2022) 18180–18186.
<https://doi.org/10.1007/s10854-022-08674-z>.
- [21] S.M.H. AL-Jawad, S.H. Sabeeh, A.A. Taha, H.A. Jassim, Studying structural, morphological and optical properties of nanocrystalline ZnO:Ag films prepared by sol-gel method for antimicrobial activity, *J. Sol-Gel Sci. Technol.* 87 (2018) 362–371.
<https://doi.org/10.1007/s10971-018-4724-9>.
- [22] Z. Ren, X. Li, L. Guo, J. Wu, Y. Li, W. Liu, P. Li, Y. Fu, J. Ma, Facile synthesis of ZnO/ZnS heterojunction nanoarrays for enhanced piezo-photocatalytic performance, *Mater. Lett.* 292 (2021). <https://doi.org/10.1016/j.matlet.2021.129635>.
- [23] Talinungsang, N. Paul, D. Dhar Purkayastha, M.G. Krishna, TiO₂/SnO₂ and SnO₂/TiO₂ heterostructures as photocatalysts for degradation of stearic acid and methylene blue under UV irradiation, *Superlattices Microstruct.* 129 (2019) 105–114.
<https://doi.org/10.1016/j.spmi.2019.03.004>.
- [24] S. Chen, F. Liu, M. Xu, J. Yan, F. Zhang, W. Zhao, Z. Zhang, Z. Deng, J. Yun, R. Chen, C. Liu, First-principles calculations and experimental investigation on SnO₂@ZnO heterojunction photocatalyst with enhanced photocatalytic performance, *J. Colloid Interface Sci.* 553 (2019) 613–621. <https://doi.org/10.1016/j.jcis.2019.06.053>.

References

- [25] V. Navakoteswara Rao, V. Preethi, U. Bhargav, P. Ravi, A. Kumar, M. Sathish, V. Krishnan, V. Venkatramu, M. Mamatha Kumari, K.R. Reddy, N.P. Shetti, T.M. Aminabhavi, M.V. Shankar, Gram-scale synthesis of ZnS/NiO core-shell hierarchical nanostructures and their enhanced H₂ production in crude glycerol and sulphide wastewater, *Environ. Res.* 199 (2021). <https://doi.org/10.1016/j.envres.2021.111323>.
- [26] F.Z. Nouasria, D. Selloum, A. Henni, S. Tingry, J. Hrbac, Improvement of the photocatalytic performance of ZnO thin films in the UV and sunlight range by Cu doping and additional coupling with Cu₂O, *Ceram. Int.* 48 (2022) 13283–13294. <https://doi.org/10.1016/j.ceramint.2022.01.207>.
- [27] M.A. Ciolan, I. Motrescu, Pulsed Laser Ablation: A Facile and Low-Temperature Fabrication of Highly Oriented n-Type Zinc Oxide Thin Films, *Appl. Sci.* 12 (2022). <https://doi.org/10.3390/app12020917>.
- [28] R. Singh, M. Gupta, S.K. Mukherjee, Effect of Ag layer thickness on optical and electrical properties of ion-beam-sputtered TiO₂/Ag/TiO₂ multilayer thin film, *J. Mater. Sci. Mater. Electron.* 33 (2022) 6942–6953. <https://doi.org/10.1007/s10854-022-07873-y>.
- [29] Y. Bouznit, A. Henni, Enhanced photoelectrochemical performance of Al-doped ZnO thin films prepared by co-spray technique, *Mater. Sci. Semicond. Process.* 118 (2020) 105208. <https://doi.org/10.1016/j.mssp.2020.105208>.
- [30] S. Iaiche, C. Boukaous, D. Alamarguy, A. Djelloul, D. Hamana, Effect of solution concentration on ZnO/ZnAl₂O₄ nanocomposite thin films formation deposited by ultrasonic spray pyrolysis on glass and si(111) substrates, *J. Nano Res.* 63 (2020) 10–30. <https://doi.org/10.4028/www.scientific.net/JNanoR.63.10>.
- [31] M. Baradaran, F.E. Ghodsi, Highly efficient visible photocatalytic degradation of MB organic dye by heteromorphic ZnO/AZO/ZnO nanocatalysts: effect of AZO thickness, *J. Sol-Gel Sci. Technol.* 92 (2019) 25–39. <https://doi.org/10.1007/s10971-019-05081-5>.
- [32] B. Al Farsi, T.M. Souier, F. Al Marzouqi, M. Al Maashani, M. Bououdina, H.M. Widatallah, M. Al Abri, Structural and optical properties of visible active photocatalytic Al doped ZnO nanostructured thin films prepared by dip coating, *Opt. Mater. (Amst.)* 113 (2021). <https://doi.org/10.1016/j.optmat.2021.110868>.

References

- [33] U.P.S. Gahlaut, V. Kumar, Y.C. Goswami, Enhanced photocatalytic activity of low cost synthesized Al doped amorphous ZnO/ ZnS heterostructures, *Phys. E Low-Dimensional Syst. Nanostructures*. 117 (2020) 1–6.
<https://doi.org/10.1016/j.physe.2019.113792>.
- [34] M. Abdelhafid, Etude des couches minces d'Oxyde de Zinc dopé Aluminium et Cobalt élaborées par la technique sol gel-spin coating. Application à la photodétection et au photocourant. thèse de doctorat, 128 (2015) 17. Thèse de doctorat, Université Freres Mentouri, Constantine (2015).
- [35] H. Adachi, K. Wasa, Thin Films and Nanomaterials, *Handb. Sputter Depos. Technol. Fundam. Appl. Funct. Thin Film. Nano-Materials MEMS Second Ed.* (2012) 3–39.
<https://doi.org/10.1016/B978-1-4377-3483-6.00001-2>.
- [36] B. Maroua, Elaboration et Caractérisation de Semi-conducteurs Transparent en Couches Minces Pour Applications Technologiques. Thèse de doctorat, Université Kasdi Merbah Ouargla, (2022).
- [37] S.A. Zakaria, S.H. Ahmadi, M.H. Amini, Chemiresistive gas sensors based on layered double hydroxides (LDHs) structures: A review, *Sensors Actuators A Phys.* 346 (2022) 113827. <https://doi.org/10.1016/j.sna.2022.113827>.
- [38] Y. Marouf, Etude et simulation des cellules solaires multi-jonctions a base de matérisux semi-conducteurs III-V. Thèse de doctorat, Université Mohamed khider Biskra, (2019).
- [39] F. Bourfaa, Effets du dopage sur les propriétés structurales et optique de films minces de l'oxyde de zinc. Mémoire de Magister, Université Mentouri Constantine, (2012).
- [40] F. Z. Nouasria, Elaboration of electrode materials based on metal-semiconductor by electrochemical method. PhD thesis, University of kasdi merbak Ouargla, (2022).
- [41] M.I. Pech-canul, Martin I. Pech-Canul Nuggehalli M. Ravindra, (2019) 17–21.
<https://doi.org/10.1007/978-3-030-02171-9>.
- [42] T. Uddin, Metal oxide heterostructures for efficient photocatalysts Presented at AND, Thesis. (2013).

References

- [43] N. Abdeouahab, Preparation and characterization of thin films nanostructures based on ZnO and other oxides, PhD thesis, University of Larbi ben m'hidi Oum el bouaghi, (2019).
- [44] Dj. Aouf, Elaboration et caractérisation des couches minces ZnS / PbS : Application antibactérienne et photocatalytique, Thèse de doctorat, Université Kasdi Merbah Ouargla, (2023).
- [45] H. He, conductors, Elsevier Inc., 2020. <https://doi.org/10.1016/B978-0-12-814930-0/00002-5>.
- [46] U.P.M. Ashik, S. Kudo, J.I. Hayashi, An Overview of Metal Oxide Nanostructures, Elsevier Ltd., 2018. <https://doi.org/10.1016/B978-0-08-101975-7.00002-6>.
- [47] X. Wu, S. Xie, H. Zhang, Q. Zhang, B.F. Sels, Y. Wang, Metal Sulfide Photocatalysts for Lignocellulose Valorization, *Adv. Mater.* 33 (2021) 1–20. <https://doi.org/10.1002/adma.202007129>.
- [48] A. TAABOUCHE, Etude structurale et optique de films minces ZnO élaborés par voie physique et/ou chimique, Thèse de doctorat, Université Mentouri Constantine, (2015).
- [49] M. Verde, EPD-deposited ZnO thin films: A review, *Bol. La Soc. Esp. Ceram. y Vidr.* 53 (2014) 149–161. <https://doi.org/10.3989/cyv.192014>.
- [50] H. BENELMADJAT, Elaboration et caractérisation de matériaux cristallins ou amorphes purs et dopés, Thèse de doctorat, Université Mentouri Constantine, (2011).
- [51] S. Brochen, Propriétés électriques du ZnO monocristallin, Thèse de doctorat, Université Grenoble, (2012).
- [52] H. Bozetine, Synthèse des nanostructures de ZnO par la méthode hydrothermale et leurs applications, Thèse de doctorat, Université Mouloud mammeri Tizi ouzou, (2017).
- [53] Y. Benkhetta, Elaboration and characterization of thin layers of zinc oxide (ZnO) deposited by ultrasonic spray for photovoltaic and optoelectronic applications, PhD thesis, University Mohamed Khider Biskra, (2018).
- [54] B. Lin, Z. Fu, Y. Jia, Green luminescent center in undoped zinc oxide films deposited

References

- on silicon substrates, *Appl. Phys. Lett.* 79 (2001) 943–945.
<https://doi.org/10.1063/1.1394173>.
- [55] Z. Sofiani, Contributions à l'étude des propriétés optiques nonlinéaires de nanoparticules en couches minces à base de ZnO. Thèse de doctorat, Université d'Angers, (2007).
- [56] B. GHARBI, Elaboration et caractérisation de films minces d'oxydes transparents conducteurs (TCO), Thèse de doctorat, Université Kasdi merbah Ouargla, (2022).
- [57] X. Yin, Y. Guo, H. Xie, W. Que, L.B. Kong, Nickel Oxide as Efficient Hole Transport Materials for Perovskite Solar Cells, *Sol. RRL.* 3 (2019) 1–27.
<https://doi.org/10.1002/solr.201900001>.
- [58] R. Gillen, J. Robertson, Accurate screened exchange band structures for the transition metal monoxides MnO, FeO, CoO and NiO, *J. Phys. Condens. Matter.* 25 (2013).
<https://doi.org/10.1088/0953-8984/25/16/165502>.
- [59] R. Barir. Caractérisation Spectroscopique des Couches minces d'oxyde de Nickel (NiO) Elaborées par Spray, Thèse de doctorat, Université Kasdi merbah Ouargla, (2018).
- [60] H. Hakkoum, Design of a photodiode based on NiO / ZnO heterojunction, Thèse de doctorat, Université Mohamed Khider Biskra, (2022).
- [61] A. Abdel-Kader, F.J. Bryant, Blue light emitting ZnS diodes, *J. Mater. Sci.* 21 (1986) 3227–3230. <https://doi.org/10.1007/BF00553360>.
- [62] A. Bartolucci, Morphological characterization of ZnS thin films for photovoltaic applications, *Amslaurea.Unibo.It.* (2015). <http://amslaurea.unibo.it/id/eprint/10540>.
- [63] A. Hadjadj, Synthèse de nanoparticules de ZnS et études de leurs propriétés structurales et optiques, Thèse de doctorat, Université Mentouri Constantine, (2014).
- [64] P. D'Amico, A. Calzolari, A. Ruini, A. Catellani, New energy with ZnS: Novel applications for a standard transparent compound, *Sci. Rep.* 7 (2017) 1–9.
<https://doi.org/10.1038/s41598-017-17156-w>.
- [65] Boyce et al., Current Perspectives on Zinc Deposits, *Irish Assoc. Econ. Geol.* (2015)

References

- 17–35.
- [66] S. Benhamida, Caractérisation Des Couches Minces D'oxyde De Nickel (Ni O) Elaboré Par Spray Pyrolyse, Thèse de doctorat, Université Mohamed Khider Biskra, (2018).
- [67] Y. Xing, X. Wang, S. Hao, X. Zhang, X. Wang, W. Ma, G. Zhao, X. Xu, Recent advances in the improvement of g-C₃N₄ based photocatalytic materials, *Chinese Chem. Lett.* 32 (2021) 13–20. <https://doi.org/10.1016/j.ccllet.2020.11.011>.
- [68] A. Saravanan, P.S. Kumar, D.V.N. Vo, P.R. Yaashikaa, S. Karishma, S. Jeevanantham, B. Gayathri, V.D. Bharathi, Photocatalysis for removal of environmental pollutants and fuel production: a review, *Environ. Chem. Lett.* 19 (2021) 441–463. <https://doi.org/10.1007/s10311-020-01077-8>.
- [69] M. Samadi, M. Zirak, A. Naseri, E. Khorashadizade, A.Z. Moshfegh, Recent progress on doped ZnO nanostructures for visible-light photocatalysis, *Thin Solid Films.* 605 (2016) 2–19. <https://doi.org/10.1016/j.tsf.2015.12.064>.
- [70] S. Helali, Application de la photocatalyse pour la dégradation des polluants chimiques et bactériologiques dans l' eau en utilisant des catalyseurs irradiés par des photons de lumière naturelle ou artificielle (UV-A / UV-B), Thèse de doctorat, Université de Lyon, (2012).
- [71] K. Hofstadler, R. Bauer, S. Novallc, G. Heisler, New Reactor Design for Photocatalytic Wastewater Treatment with TiO₂ Immobilized on Fused-Silica Glass Fibers: Photomineralization of 4-Chlorophenol, *Environ. Sci. Technol.* 28 (1994) 670–674. <https://doi.org/10.1021/es00053a021>.
- [72] N. LAID, Dégradation Photocatalytique Du Mordant Bleu 13 En Milieu Hétérogène, Mémoire de Magister, Université Mentouri Constantine, (2010).
- [73] W.S. Koe, J.W. Lee, W.C. Chong, Y.L. Pang, L.C. Sim, An overview of photocatalytic degradation: photocatalysts, mechanisms, and development of photocatalytic membrane, *Environ. Sci. Pollut. Res.* 27 (2020) 2522–2565. <https://doi.org/10.1007/s11356-019-07193-5>.
- [74] K.M. Reza, A. Kurny, F. Gulshan, Parameters affecting the photocatalytic degradation

References

- of dyes using TiO₂: a review, *Appl. Water Sci.* 7 (2017) 1569–1578.
<https://doi.org/10.1007/s13201-015-0367-y>.
- [75] E.A. Al-Maliky, H.A. Gzar, M.G. Al-Azawy, Determination of Point of Zero Charge (PZC) of Concrete Particles Adsorbents, *IOP Conf. Ser. Mater. Sci. Eng.* 1184 (2021) 012004. <https://doi.org/10.1088/1757-899x/1184/1/012004>.
- [76] N.S. Jyothi, K. Ravichandran, Optimum pH for effective dye degradation: Mo, Mn, Co and Cu doped ZnO photocatalysts in thin film form, *Ceram. Int.* 46 (2020) 23289–23292. <https://doi.org/10.1016/j.ceramint.2020.06.076>.
- [77] M. Berradi, R. Hsissou, M. Khudhair, M. Assouag, O. Cherkaoui, A. El Bachiri, A. El Harfi, Textile finishing dyes and their impact on aquatic environs, *Heliyon.* 5 (2019). <https://doi.org/10.1016/j.heliyon.2019.e02711>.
- [78] R. Messemche, Elaboration and characterization of undoped and doped titanium dioxide thin layers by sol gel (spin coating) for photocatalytic applications, PhD thesis, University Mohamed Khider Biskra, (2021).
- [79] A. Mittal, J. Mittal, A. Malviya, D. Kaur, V.K. Gupta, Adsorption of hazardous dye crystal violet from wastewater by waste materials, *J. Colloid Interface Sci.* 343 (2010) 463–473. <https://doi.org/10.1016/j.jcis.2009.11.060>.
- [80] U. Shanker, M. Rani, V. Jassal, Degradation of hazardous organic dyes in water by nanomaterials, *Environ. Chem. Lett.* 15 (2017) 623–642.
<https://doi.org/10.1007/s10311-017-0650-2>.
- [81] P.O. Oladoye, T.O. Ajiboye, E.O. Omotola, O.J. Oyewola, Methylene blue dye: Toxicity and potential elimination technology from wastewater, *Results Eng.* 16 (2022) 100678. <https://doi.org/10.1016/j.rineng.2022.100678>.
- [82] S. Goktas, A. Goktas, A comparative study on recent progress in efficient ZnO based nanocomposite and heterojunction photocatalysts: A review, *J. Alloys Compd.* 863 (2021). <https://doi.org/10.1016/j.jallcom.2021.158734>.
- [83] M.R. Islam, M. Rahman, S.F.U. Farhad, J. Podder, Structural, optical and photocatalysis properties of sol–gel deposited Al-doped ZnO thin films, *Surfaces and Interfaces.* 16 (2019) 120–126. <https://doi.org/10.1016/j.surfin.2019.05.007>.

References

- [84] M. Bizarro, A. Sánchez-Arzate, I. Garduño-Wilches, J.C. Alonso, A. Ortiz, Synthesis and characterization of ZnO and ZnO:Al by spray pyrolysis with high photocatalytic properties, *Catal. Today*. 166 (2011) 129–134.
<https://doi.org/10.1016/j.cattod.2010.08.005>.
- [85] P. Pradhan, J.C. Alonso, M. Bizarro, Photocatalytic performance of ZnO: Al films under different light sources, *Int. J. Photoenergy*. 2012 (2012).
<https://doi.org/10.1155/2012/780462>.
- [86] W. Vallejo, A. Cantillo, C. Díaz-Urbe, Methylene Blue Photodegradation under Visible Irradiation on Ag-Doped ZnO Thin Films, *Int. J. Photoenergy*. 2020 (2020).
<https://doi.org/10.1155/2020/1627498>.
- [87] M. Hajji, M. Ajili, N. Jebbari, A. Garcia loreiro, N.T. Kamoun, Photocatalytic performance and solar cell applications of coupled semiconductor CuO– ZnO sprayed thin films: Coupling effect between oxides, *Opt. Mater. (Amst)*. 140 (2023).
<https://doi.org/10.1016/j.optmat.2023.113798>.
- [88] O. Darfan, Elaboration et caractérisation des couches minces de Sulfure de Zinc préparées par spray ultrasonique., *Univ. Mentouri-Constantine*. (2011).
- [89] K. Oura, M. Katayama, A. V. Zotov, V.G. Lifshits, A.A. Saranin, Growth of Thin Films, (2003) 357–387. https://doi.org/10.1007/978-3-662-05179-5_14.
- [90] J.C. Vigui, J. Spitz, Chemical Vapor Deposition at Low Temperatures. *J. Electrochem.Soc.*, 122(4), (1975) 585–588.
- [91] A.A. Mane, P.S. Maldar, S.H. Dabhole, S.A. Nikam, A. V. Moholkar, Effect of substrate temperature on physicochemical and gas sensing properties of sprayed orthorhombic V2O5 thin films, *Meas. J. Int. Meas. Confed*. 131 (2019) 223–234.
<https://doi.org/10.1016/j.measurement.2018.08.042>.
- [92] A.G. Ricciardulli, P.W.M. Blom, Solution-Processable 2D Materials Applied in Light-Emitting Diodes and Solar Cells, *Adv. Mater. Technol*. 5 (2020).
<https://doi.org/10.1002/admt.201900972>.
- [93] A. Maache, Elaboration et caractérisation optique des couches minces de ZnO dopé ou Co-dopé obtenues par méthode sol-gel. Thèse de doctorat, Université Ferhat Abbas

References

- Sétif 1, (2021).
- [94] L. Qin, Y. Hu, H. Wei, Nanozymes : Preparation and Characterization Nanozymes : Preparation and Characterization, (2020). <https://doi.org/10.1007/978-981-15-1490-6>.
- [95] W. Allag, Study of thin films for photovoltaic solar cells Par Walid Alla. PhD thesis, University Ferhat Abbas Sétif 1, (2022).
- [96] A. Derbali, A. Attaf, H. Saidi, M.S. Aida, H. Benamra, R. Attaf, N. Attaf, H. Ezzaouia, L. Derbali, Br doping effect on structural, optical and electrical properties of ZnS thin films deposited by ultrasonic spray, Mater. Sci. Eng. B Solid-State Mater. Adv. Technol. 268 (2021) 115135. <https://doi.org/10.1016/j.mseb.2021.115135>.
- [97] A. Derbali, H. Saidi, A. Attaf, H. Benamra, A. Bouhdjer, N. Attaf, H. Ezzaouia, L. Derbali, M.S. Aida, Solution flow rate influence on ZnS thin films properties grown by ultrasonic spray for optoelectronic application, J. Semicond. 39 (2018) 1–7. <https://doi.org/10.1088/1674-4926/39/9/093001>.
- [98] M.A. Bouacheria, A. Djelloul, M. Adnane, Y. Larbah, L. Benharrat, Characterization of Pure and Al Doped ZnO Thin Films Prepared by Sol Gel Method for Solar Cell Applications, J. Inorg. Organomet. Polym. Mater. 32 (2022) 2737–2747. <https://doi.org/10.1007/s10904-022-02313-0>.
- [99] X. Li, X. Zhu, D. Yang, Enhanced luminescent performance with surface wrinkled Al-doped ZnO films, J. Mater. Sci. Mater. Electron. 31 (2020) 6304–6312. <https://doi.org/10.1007/s10854-020-03186-0>.
- [100] A. Najim, B. Hartiti, H. Labrim, S. Fadili, M. Ertuğrul, P. Thevenin, Synthesis of ZnS thin films using the spray pyrolysis technique, J. Mater. Sci. Mater. Electron. 33 (2022) 15086–15097. <https://doi.org/10.1007/s10854-022-08428-x>.
- [101] U. Kuhlmann, H. Werheit, T. Lundström, W. Robers, Optical properties of amorphous boron, J. Phys. Chem. Solids. 55 (1994) 579–587. [https://doi.org/10.1016/0022-3697\(94\)90056-6](https://doi.org/10.1016/0022-3697(94)90056-6).
- [102] Q. Li, S. Hu, H. Wang, F. Wang, X. Zhong, X. Wang, Study of copper foam-supported Sn thin film as a high-capacity anode for lithium-ion batteries, Electrochim. Acta. 54 (2009) 5884–5888. <https://doi.org/10.1016/j.electacta.2009.05.051>.

References

- [103] D. Fang, K. Lin, T. Xue, C. Cui, X. Chen, P. Yao, H. Li, Influence of Al doping on structural and optical properties of Mg-Al co-doped ZnO thin films prepared by sol-gel method, *J. Alloys Compd.* 589 (2014) 346–352. <https://doi.org/10.1016/j.jallcom.2013.11.061>.
- [104] N. Al Dahoudi, A. Alkahlout, S. Heusing, P. Herbeck-Engel, R. Karos, P. Oliveira, Indium doped zinc oxide nanopowders for transparent conducting coatings on glass substrates, *J. Sol-Gel Sci. Technol.* 67 (2013) 556–564. <https://doi.org/10.1007/s10971-013-3114-6>.
- [105] M. Mohamed, A. Sedky, A.S. Alshammari, M. Gandouzi, Optical, photoluminescence and ferromagnetic properties of Ni-doped ZnO for optoelectronic applications, *J. Mater. Sci. Mater. Electron.* 32 (2021) 5186–5198. <https://doi.org/10.1007/s10854-021-05250-9>.
- [106] A. Baranowska-Korczyca, M. Kościński, E.L. Coy, B.F. Grześkowiak, M. Jasiurkowska-Delaporte, B. Peplińska, S. Jurga, ZnS coating for enhanced environmental stability and improved properties of ZnO thin films, *RSC Adv.* 8 (2018) 24411–24421. <https://doi.org/10.1039/c8ra02823k>.
- [107] N.P. Poddar, S.K. Mukherjee, Investigations on preferentially oriented Al-doped ZnO films developed using rf magnetron sputtering, *J. Mater. Sci. Mater. Electron.* 30 (2019) 537–548. <https://doi.org/10.1007/s10854-018-0320-6>.
- [108] D. Djouadi, A. Chelouche, A. Aksas, Amplification of the UV emission of ZnO: Al thin films prepared by sol-gel method, *J. Mater. Environ. Sci.* 3 (2012) 585–590.
- [109] M. Sypniewska, R. Szczesny, P. Popielarski, K. Strzalkowski, B. Derkowska-Zielinska, Structural, morphological and photoluminescent properties of annealed ZnO thin layers obtained by the rapid sol-gel spin-coating method, *Opto-Electronics Rev.* 28 (2020) 182–190. <https://doi.org/10.24425/opelre.2020.134460>.
- [110] E. György, A. Pérez del Pino, J. Roqueta, C. Sánchez, A.G. Oliva, Processing and immobilization of chondroitin-4-sulphate by UV laser radiation, *Colloids Surfaces B Biointerfaces.* 104 (2013) 169–173. <https://doi.org/10.1016/j.colsurfb.2012.11.044>.
- [111] A.J. Haider, R. Al-Anbari, H.M. Sami, M.J. Haider, Enhance preparation and

References

- characterization of nickel-oxide as self-cleaning surfaces, *Energy Procedia*. 157 (2019) 1328–1342. <https://doi.org/10.1016/j.egypro.2018.11.298>.
- [112] H.W. Wu, C.H. Chu, Structural and optoelectronic properties of AZO/Mo/AZO thin films prepared by rf magnetron sputtering, *Mater. Lett.* 105 (2013) 65–67. <https://doi.org/10.1016/j.matlet.2013.04.017>.
- [113] F. Eskandari, M. Ranjbar, P. Kameli, H. Salamati, Laser induced photoconductivity in sol-gel derived Al doped ZnO thin films, *J. Alloys Compd.* 649 (2015) 35–45. <https://doi.org/10.1016/j.jallcom.2015.07.093>.
- [114] M. Nikzad, M.R. Khanlary, S. Rafiee, Structural, optical and morphological properties of Cu-doped ZnS thin films synthesized by sol–gel method, *Appl. Phys. A Mater. Sci. Process.* 125 (2019) 1–9. <https://doi.org/10.1007/s00339-019-2790-7>.
- [115] A. Tounsi, R. Khalfi, D. Talantikite-Touati, H. Merzouk, A. Souici, Characterization of cerium-doped zinc sulfide thin films synthesized by sol–gel method, *Appl. Phys. A Mater. Sci. Process.* 128 (2022). <https://doi.org/10.1007/s00339-022-05409-z>.
- [116] E.E. El-Katori, E.A. Kasim, D.A. Ali, Sol–gel synthesis of mesoporous NiO/ZnO heterostructure nanocomposite for photocatalytic and anticorrosive applications in aqueous media, *Colloids Surfaces A Physicochem. Eng. Asp.* 636 (2022). <https://doi.org/10.1016/j.colsurfa.2021.128153>.
- [117] H. Sutanto, S. Durri, S. Wibowo, H. Hadiyanto, E. Hidayanto, Rootlike Morphology of ZnO:Al Thin Film Deposited on Amorphous Glass Substrate by Sol-Gel Method, *Phys. Res. Int.* 2016 (2016). <https://doi.org/10.1155/2016/4749587>.
- [118] T. Ivanova, A. Harizanova, T. Koutzarova, B. Vertruyen, R. Closset, Structural and optical characterization of nitrogen and gallium co-doped ZnO thin films, deposited by sol-gel method, *J. Mol. Struct.* 1206 (2020) 127773. <https://doi.org/10.1016/j.molstruc.2020.127773>.
- [119] H. Layoul, F. Meriche, Y. Bouznit, A. Boukerika, Structural and optical characterization of sol–gel processed Al-doped ZnO waveguide films for integrated optical devices, *Appl. Phys. A Mater. Sci. Process.* 127 (2021) 1–12. <https://doi.org/10.1007/s00339-021-04752-x>.

References

- [120] I. Loyola Poul Raj, S. Valanarasu, R.S. Rimal Isaac, M. Ramudu, Y. Bitla, V. Ganesh, I.S. Yahia, The role of silver doping in tuning the optical absorption, energy gap, photoluminescence properties of NiO thin films for UV photosensor applications, *Optik (Stuttg)*. 254 (2022) 168634. <https://doi.org/10.1016/j.ijleo.2022.168634>.
- [121] M.I. Din, J. Najeeb, G. Ahmad, Recent Advancements in the Architecting Schemes of Zinc Oxide-Based Photocatalytic Assemblies, *Sep. Purif. Rev.* 47 (2018) 267–287. <https://doi.org/10.1080/15422119.2017.1383918>.
- [122] H. Wang, L. Zhang, Z. Chen, J. Hu, S. Li, Z. Wang, J. Liu, X. Wang, Semiconductor heterojunction photocatalysts: Design, construction, and photocatalytic performances, *Chem. Soc. Rev.* 43 (2014) 5234–5244. <https://doi.org/10.1039/c4cs00126e>.
- [123] R. Mahdavi, S.S.A. Talesh, Sol-gel synthesis, structural and enhanced photocatalytic performance of Al doped ZnO nanoparticles, *Adv. Powder Technol.* 28 (2017) 1418–1425. <https://doi.org/10.1016/j.appt.2017.03.014>.
- [124] I. Khan, K. Saeed, I. Zekker, B. Zhang, A.H. Hendi, A. Ahmad, S. Ahmad, N. Zada, H. Ahmad, L.A. Shah, T. Shah, I. Khan, Review on methylene blue: Its properties, uses, toxicity and photodegradation, *Water* 14, no. 2 (2022) 242. <https://doi.org/10.3390/w14020242>
- [125] Y.G. Habba, M. Capochichi-Gnambodoe, L. Serairi, Y. Leprince-Wang, Enhanced photocatalytic activity of ZnO nanostructure for water purification, *Phys. Status Solidi Basic Res.* 253 (2016) 1480–1484. <https://doi.org/10.1002/pssb.201600031>.
- [126] J. Luan, Z. Hu, Synthesis, property characterization, and photocatalytic activity of novel visible light-responsive photocatalyst Fe₂BiSbO₇, *Int. J. Photoenergy*. 2012 (2012). <https://doi.org/10.1155/2012/301954>.
- [127] E. Parvizi, R. Tayebee, E. Koushki, M.F. Abdizadeh, B. Maleki, P. Audebert, L. Galmiche, Photocatalytic efficacy of supported tetrazine on MgZnO nanoparticles for the heterogeneous photodegradation of methylene blue and ciprofloxacin, *RSC Adv.* 9 (2019) 23818–23831. <https://doi.org/10.1039/c9ra04702f>.
- [128] K.A. Isai, V.S. Shrivastava, Photocatalytic degradation of methylene blue using ZnO and 2%Fe–ZnO semiconductor nanomaterials synthesized by sol–gel method: a

References

- comparative study, SN Appl. Sci. 1 (2019) 1–11. <https://doi.org/10.1007/s42452-019-1279-5>.
- [129] S. Velanganni, S. Pravinraj, P. Immanuel, R. Thiruneelakandan, Nanostructure CdS/ZnO heterojunction configuration for photocatalytic degradation of Methylene blue, Phys. B Condens. Matter. 534 (2018) 56–62. <https://doi.org/10.1016/j.physb.2018.01.027>.

Abstract

Function semiconductor metal oxide photocatalysts, particularly as thin films mono or multilayer films were demonstrated in this work by synthesis of undoped, Al-doped, and (Al, Ni) co-doped ZnO by spray pyrolysis on a glass substrate in the first part. In the second part, the preparation of multilayer films: Al-ZnO as a bottom layer using spin coating and then sprayed by ZnS and then by NiO as upper layers using spray pyrolysis to get Al-ZnO/ZnS, and for the first time Al-Zinc-O/Zinc-S/Nickel-O multilayers and studied their several properties. X-Ray D, FTIR (ATR), and SEM with EDX, AFM, and UV-vis spectrophotometer characterized the resulting films. Structural XRD study confirmed the high crystallinity ZnO wurtzite structure preferentially oriented along the planes (002) and the successful preparation of the deposited phases in multilayer films. SEM results revealed uniform nanostructure films with small spherical shapes and aggregates in undoped and Al-doped ZnO and slight variations in diameter for (Al, Ni) Co-doped ZnO for the spread samples. Moreover, The SEM examination of the multilayer films suggested that the deposition of multi-nanocrystalline films over each other could damage the cohesion of the top layer, which influences its uniformity. EDX mapping demonstrated the existence of the deposited materials, particularly dopant traces. Moreover, The optical characteristics have been reported that all the ZnO pure and doped films are transparent, and have a high average transmittance of 85%, while the multilayer exhibits a low one of 65%. The photocatalytic rate of the multilayer (Zinc-O:Al/Zinc-S/Nickel-O) under vis-light was ~96% efficiency against MB after only 50 min. It improved its stability with slightly reduced observed after the fifth cycle. Further, under sunlight, the degradation reached 90, 85, and 65% for MB, CV, and CR, respectively, in 90 min. This work demonstrates the effective degradation of organic contaminants using a constructed ZnO:Al/ZnS/NiO heterojunction photocatalyst.

Keywords: pure ZnO, Co-doped ZnO, multilayer thin films, ZnO:Al/ZnS/NiO, spray pyrolysis, visible irradiation.

ملخص

تم توضيح وظيفة المحفزات الضوئية لأكسيد المعدن من انصاف النواقل ، خاصة الأغشية الرقيقة أحادية أو متعددة الطبقات في هذا العمل من خلال انشاء طبقات رقيقة من ZnO النقي والمطعم بـ Al ، و ثنائي التطعيم بالألمنيوم والنيكل باستعمال تقنية الانحلال الحراري بالرش على ركيزة زجاجية في الجزء الأول. في الجزء الثاني تم تحضير أغشية متعددة الطبقات: من أكسيد الزنك كطبقة سفلية باستخدام الطلاء الدوراني ومن ثم تغليفها بـ ZnS ومن ثم بواسطة NiO كطبقات عليا باستخدام التحلل الحراري بالرش للحصول على ZnO/ZnS/Al ، ولأول مرة عينة متعددة الطبقات ZnO:Al/ZnS/NiO ودراسة خواصها المختلفة. تم تشخيص الأفلام الناتجة باستخدام مطيافية XRD ، FTIR ، SEM/EDS ، AFM ، والأشعة فوق البنفسجية. أكد تحليل XRD و FTIR الهيكلي على بنية ZnO wurtzite عالية التبلور بنمو الحبيبات بشكل تفضيلي على طول المستويات (002)؛ وبين التحضير الناجح لطور ZnO و ZnS و NiO في أفلام متعددة الطبقات. كشفت نتائج SEM عن أفلام ذات بنية نانوية موحدة ذات أشكال كروية صغيرة وركام في ZnO غير المطعم والمطعم مع اختلافات طفيفة في القطر للألمنيوم والنيكل لـ ZnO ثنائي التطعيم. علاوة على ذلك ، أشار تحليل SEM للعينات متعددة الطبقات إلى أن ترسيب أفلام بلورية نانوية مختلفة فوق بعضها البعض يمكن أن يؤدي إلى تدهور التصاق الطبقة العليا ، مما قد يؤثر على شكل سطحها المتجانس. أظهر تحليل أطياف EDS وجود المواد المرسبة ، وخاصة آثار للشوائب المضافة. إضافة إلى ذلك ، يُظهر AFM خشونة سطحية مقبولة للاستخدام كمحفز ضوئي. تم الإبلاغ عن الخصائص البصرية أن جميع أفلام ZnO النقية والمطعمة شفافة ، ولها متوسط نفاذية مرتفع يصل إلى 85% ، في حين أن الطبقات المتعددة تظهر نفاذية اقل تصل إلى 65%. أظهر نشاط التحفيز الضوئي لمتعدد الطبقات (ZnO:Al/ZnS/NiO) تحت الضوء المرئي كفاءة تحلل ضوئي تبلغ حوالي 96% ضد أزرق الميثيلين بعد 50 دقيقة فقط. لقد أدى إلى تحسين ثباته مع انخفاض طفيف بعد الدورة الخامسة. ومع ذلك ، تحت ضوء الشمس ، وصلت معدلات التحلل إلى 90 و85 و65% لأزرق الميثيلين والبنفسجي البلوري والأحمر الكونغولي ، على التوالي ، في 90 دقيقة. توضح هذه الدراسة أن المحفز الضوئي متعدد الطبقات ZnO:Al/ZnS/NiO المركب يمكنه تحليل الملوثات العضوية بكفاءة.

الكلمات المفتاحية: ZnO:Al/ZnS/NiO ، ZnO ثنائي التطعيم ، الأغشية الرقيقة متعددة الطبقات ،

ZnO:Al/ZnS/NiO ، الانحلال الحراري بالرش ، الاشعاع المرئي

